Integrated Modeling to Facilitate Control Architecture Design for Lightweight Space Telescopes

by

Lucy Elizabeth Cohan

Submitted to the Department of Aeronautics and Astronautics
in partial fulfillment of the requirements for the degree of

Masters of Science in Aeronautics and Astronautics

at the

MASSACHUSETTS INSTITUTE OF TECHNOLOGY

June 2007

Author .....
Department of Aeronautics and Astronautics
June 8, 2007

Certified by .....
David W. Miller
Professor
Thesis Supervisor

Accepted by .....
Jaime Peraire
Chairman, Department Committee on Graduate Students

Integrated Modeling to Facilitate Control Architecture Design for Lightweight Space Telescopes

by

Lucy Elizabeth Cohan

Submitted to the Department of Aeronautics and Astronautics
on June 8, 2007, in partial fulfillment of the
requirements for the degree of
Masters of Science in Aeronautics and Astronautics

Abstract

The purpose of this thesis it to examine the effects of utilizing control to better meet performance and systematic requirements of future space telescopes. New telescope systems are moving toward tighter optical performance requirements with lower mass and cost, creating an implicit conflict for currently designed systems. Therefore, new technology and telescope types must be developed and implemented, and a key to lightweight systems is the addition of controls. This thesis uses an integrated modeling technique to examine a large tradespace of space telescope systems. The analysis techniques includes finite element and dynamic disturbance analyses to determine the effects of various parameters on overall system performance metrics.

In particular, this thesis will focus on the control system architecture for future space telescopes. As systems become less massive, more control is necessary to meet the performance requirements. Less massive systems have more flexibility, which degrades performance. Thus, this flexibility must be controlled to obtain adequate performance. However, the control also has a cost that must be considered. As the areal density of the mirror decreases, the cost due to mass decreases, but the cost due to control increases because more control is required to meet the requirements. Therefore, a balance between lightweight systems and control is sought to give the best overall performance. Additionally, there are many different types of control that could be used on the system, thus finding optimal combinations of controllers, sensors, actuators, and bandwidths is a daunting task. The integrated modeling technique allows the designer to examine the effects of structural parameters and requirements on the control system architecture and the performance metrics. The ability to determine favorable control system architectures early in the design process will allow new technologies to be pushed further, while still maintaining confidence that the system will perform as expected.

Thesis Supervisor: David W. Miller
Title: Professor

Acknowledgments

Thank you to the Department of Defense for their support of this work, Professor David Miller for guidance throughout the program, the MOST team of Scott Uebelhart, Deborah Howell, Elizabeth Jordan, Andrzej Stewart, and Tom Gray, and my family and friends for their support.

Contents

List of Figures

List of Tables

Chapter 1

Introduction

1.1 Motivation

Current space telescopes are reaching their limits in terms of size, cost, and performance. Future systems include increasingly tight performance requirements, with line-of-sight (LOS) jitter on the order of milli-arcseconds and wavefront error (WFE) on the order of nanometers. At the same time, lower mass, lower cost, and rapidly deployed systems are desired. This creates an implicit conflict for currently designed systems, thus new technologies and telescope types must be developed and implemented. Candidate technologies for these new systems include deployable mirrors or sparse apertures, structural control, and adaptive optics. Sparse apertures and deployable mirrors can be deployed on orbit, preventing the launch fairing diameter from imposing an aperture size constraint. Also, the smaller, identical mirrors used in sparse apertures are easier and less expensive to manufacture than large monolithic mirrors. However, the cost and complexity of precision beam combining can off-set some of these savings. Structural control can provide a means to achieve better performance with a less massive system by controlling the flexible dynamics of the lightweight system, but at the cost and complexity of multi-channel control and support avionics. Adaptive optics can also help to meet the strict performance requirements; a fast steering mirror can correct for LOS jitter, and wavefront sensing and shape control can rectify both thermal and dynamic distortions of the primary

mirror. These and other technologies provide a promising path to meeting both the performance and programmatic requirements of future space telescopes. The challenge is in determining the combinations of technologies that create the most favorable architectures. Each of these technologies has associated cost, mass, and complexity; the relationships arising from the utilization of such combinations is complicated, and thus it is a challenge to find a favorable balance. Therefore, it is important to explore the entire tradespace of possible designs to ensure that superior designs are not overlooked.

One way to meet such demanding requirements is to introduce control into the system; control can allow flexible systems to meet the tight performance requirements imposed by the optical imaging system. However, control can be added in many different places and at various levels of authority, so it is necessary to find to the correct balance of control. Although control can provide great benefit, it also comes at the cost of stability margin, complexity, robustness, and power. Therefore, there is an optimal amount of control where the performance is maximized, but the control costs are minimized. This point, where the aggregate cost of the mission is minimized, is sought.

Additionally, the new technologies and additional controls that are included in the system, to meet the performance requirements, change the system architecture. In the past, many of the major design decisions made during the conceptual design phase were based on previous engineering experience. This works well for designs that are based on heritage. However, when the technologies and architectures completely change, this intuition is no longer as reliable. Therefore, many possible designs should be analyzed during the conceptual design phase to ensure a good design before the major decisions are made.

The Modular Optical Space Telescope (MOST) project uses a parametric, integrated modeling technique to quantitatively determine the performance of many different architectures during the conceptual design phase. In order to have an accurate performance prediction, the key features of the structure and the control systems must be included. The MOST project models the telescope system, including the end-to-

end propagation of disturbance to performance. It also strives to include many types of performance requirements so that an accurate interpretation of the overall quality of the design can be achieved. In particular, this thesis utilizes and examines various control systems, including their implementation and their effects on the performance of space telescopes.

1.2 Literature Review

There is a large amount of literature available addressing space telescopes and space telescope modeling. Select works, chosen for their relevance to the specific technologies utilized in this thesis, will be discussed. The literature review is broken into two sections: the first focusing on parametric and integrated modeling techniques, and the second focusing on controls interactions for such systems.

1.2.1 Parametric and Integrated Modeling

An overview of relevant literature addresses a number of integrated modeling efforts for future space telescope systems. NASA's James Webb Space Telescope (JWST) is using an integrated model [24, 17] to assess the performance of the telescope, both optically and structurally. Also, integrated models were used in earlier design phases of JWST [15] to determine the sources of error and likelihood of meeting the performance requirements. In many future systems such as JWST, the size will prevent full integrated testing prior to launch, so integrated models of the performance are a necessary substitute. Also, the LISA space telescope [41] is incorporating extensive integrated modeling, again, because it will not be able to be fully tested on the ground. LISA consists of three separate spacecraft that must function as one, making the accuracy of the performance predictions extremely important. The Terrestrial Planet Finder (TPF) mission has used integrated modeling [35] for design trades and to predict optical performance. The Space Interferometry Mission (SIM) [22, 43] uses integrated modeling to optimize key instrument features as well as assess on-orbit performance in the absence of representative ground tests. Each of these missions,

along with many other missions, have used integrated modeling as an important component of the design and verification of performance. However, most of these models are created and utilized after the important conceptual design decisions have been made and the design is near completion. Then, the models are used to optimize key components of the design and predict performance.

Additionally, there are a number of ground-based telescopes that are undergoing integrated modeling efforts [4, 36]. Like space-based telescopes, ground-based telescopes have tight performance requirements; the disturbance they encounter is primarily due to wind. Therefore, though the environment is different, many of the same techniques can be applied. The Thirty Meter Telescope (TMT) has undergone extensive integrated modeling efforts [5, 16]. These models incorporate tradespace analysis during conceptual design, rather than purely a performance prediction, and thus are more similar to the desired outcome of the MOST project.

Parametric modeling and tradespace analysis have also been utilized in other fields. Botkin [9] uses parametric modeling for computer-aided-design (CAD) modeling of automobiles. Fenyes [19] uses the parametric technique for modeling the hierarchical flow of parameters to smaller components for automotive design. Alexandrov et. al. [2] uses parametric techniques for airplane wing design and analysis. Smith et. al. [48] uses aircraft geometric parameters to create finite element models of the airplane structure. Sensmeier et. al. [45] uses parametric design and analysis to predict and optimize the weight of the aircraft wing. Each of these models are adapted to the specific problem and field, but the overall parametric modeling concept is similar to that of MOST. Parametric, integrated modeling has had much success in automotive finite element modeling and aircraft computational fluid dynamics, along with the ground-based telescope modeling, making the spacecraft modeling a next logical step.

Work has also been done in developing tradespace analysis tools for conceptual design of space systems. Jilla [28] uses the Generalized Information Network Analysis (GINA) framework to mathematically model the conceptual design of satellite systems in order to utilize optimization methods, with specific applications to TPF.

Guitierrez [23] developed an end-to-end performance model which incorporates disturbance and uncertainty in order to tune the structure so that it meets performance requirements, specifically applied to SIM. Portions of both of these techniques are used in creating and analyzing the end-to-end MOST model.

The MOST project builds upon these works. It uses a parametric, integrated model to quantitatively determine the end-to-end performance [52, 53]. The parametric finite element model has been created [29]. An integrated state-space dynamics model, complete with disturbance, optical performance, and uncertainty [55] has also been created. The next step in this analysis is the inclusion and balancing of control systems. The following section will address the relevant literature relating to the inclusion of controls.

1.2.2 Design of Controlled Structures

There is also an abundance of literature on controls, controlled structures, and adaptive optics. Crawley et. al. [13] provides an overview of structural dynamics and control theory as applicable to controlling flexible structures. Also, work has been done in designing controlled structures [27], optimization of controls/structures interactions over select frequencies [39], uncertainty modeling of controlled structures [11], and end-to-end modeling of such systems [23]. The Middeck Active Controls Experiment (MACE) program [42] investigated the process for confidently predicting the behavior of control for flexible structures in a zero-gravity environment and provides ample research and documentation on the modeling and control of such systems.

Additionally there is a great deal of background on control theory available. Grocott [21] includes an overview and comparison of various control techniques for uncertain structural systems. Mallory [37] gives a method for control tuning, as well as multi-input, multi-output (MIMO) extensions to single-input, single-output (SISO) control theory. Also, many books, such as Van de Vegte [14], Bryson [30], Brown and Huang [10], Zhou [58], and Kwakernaak and Sivan [31] were used for control theory background, algorithms, and implementations.

Adaptive optics, and specifically deformable mirrors, is another area which has

undergone considerable research. Irschik [26] provides an overview of structural shape control using piezo electrics. Freeman [20] describes various adaptive optics techniques and motivation for utilizing adaptive optics. Tyson's [51] book summarizes the field of adaptive optics, including optics principles, wavefront sensing, and wavefront control for a wide variety of optical systems. These references provide a basis for the prior work in the field of adaptive optics.

Finally, there as been some work in determining how to partition controls between multiple controllers with different bandwidth ranges. Liu [34] discusses regulating optical path length for interferometers, and the necessity of using a suite of actuators and controllers, since a single actuator cannot provide both the large control authority, bandwidth, and dynamic range, that are necessary. Therefore, the actuation is staged and the utilization of multiple actuators to accomplish an overall stabilization problem is discussed. This type of work combines the effects of multiple actuators to improve a particular performance metric, which is one step away from using multiple controllers to improve multiple performance metrics.

There is literature available on different portions of the problem. However, there are very few studies combining all of these areas together to look at the overall control architecture design. By combining these different techniques and fields, comprehensive modeling and analysis of the control of flexible space telescopes is possible.

1.3 Thesis Objective

There has been previous work done in the fields of integrated and parametric modeling, conceptual-design tradespace analysis, controls-structures interactions, and adaptive optics. However, less attention has been given to combining all of these areas for space telescope conceptual design. The MOST project aims to fill some of these missing portions, and has succeeded in the areas of parametric finite element modeling and dynamic analysis. However, the addition of controls interactions still remains. Therefore, the objective of this thesis is to examine a number of possible control systems, their effects, and their interactions in order to identify families of architec-

tures with favorable characteristics.. The effects of four different control systems on the performance and the cost are examined. Additionally, the interactions between control systems, and the effect of the structural configuration on the control system performance, are included.

1.4 Approach

This thesis develops a method for determining a control architecture for space telescopes. Figure 1-1 shows a block diagram of the flow of the analysis in this thesis. Chapter 2 describes the MOST model and the integrated modeling technique. It focuses on the entire modeling process, including the key structural features, integrated model formulation, and analysis routines. Additionally, the performance metrics by which the designs are distinguished are motivated and presented. Then, Chapter 3 describes the control systems used in the model. Each control system and its implementation is described individually, and the resulting performance from utilizing only that particular controller is presented. The individual trends in performance and cost are discussed.

Chapter 4 presents the slew and settle analysis. This analysis provides a metric for mission operations in determining the amount of time necessary to point the telescope to a new location and stabilize the image. The various parameters affecting this analysis are examined and analyzed.

Chapter 5 looks at the interactions between control systems. First, it examines the interactions of two control systems at a time. Then, it proceeds in examining the effects of all control parameters together on a single structural configuration. Finally, it investigates the selection of a control architecture. Chapter 6 includes both the control and structural parameters in a complete tradespace. The controls/structures interactions are presented to help determine families of favorable architectures. Finally, Chapter 7 concludes with a summary of the preceding chapters, summarizing the necessary steps in determining a space telescope control architecture.

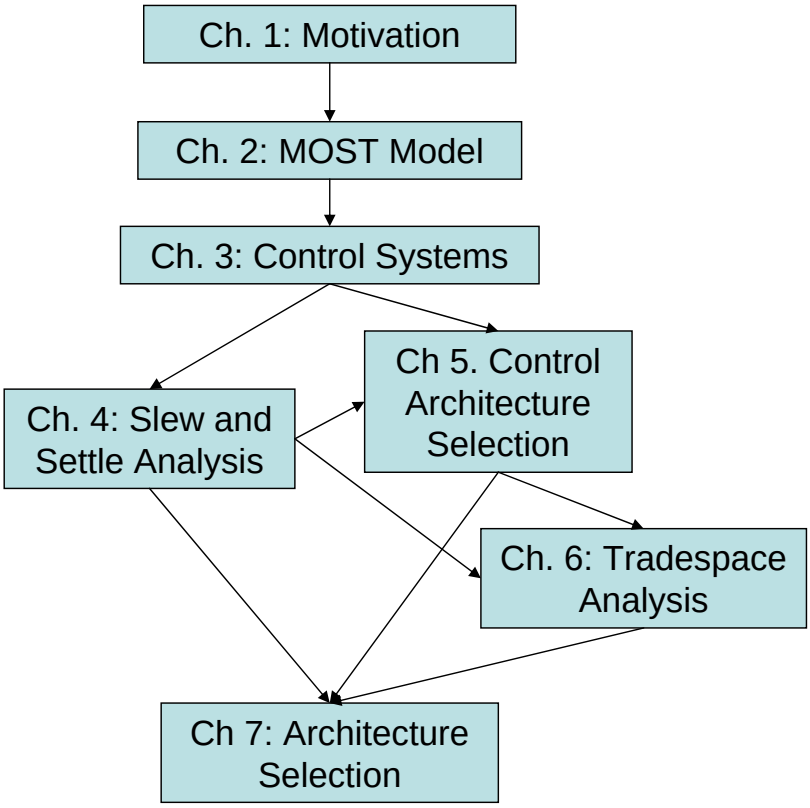

Figure 1-1: Thesis Outline

Chapter 2

Modular Optical Space Telescope (MOST)

The Modular Optical Space Telescope (MOST) model is a parametric, integrated model that allows analysis of many different telescope realizations in the early phases of design. Instead of modeling a single point design in detail, the MOST model enables the examination of a full tradespace of many different designs to determine favorable families of architectures. This technique also allows for the addition of many different telescope components, control systems, and analysis routines. This chapter will focus on a basic overview of the MOST model and how it can be used for analyzing control architectures. The parametric modeling environment (Section 2.2), structural finite element model (Section 2.3), integrated model formulation (Section 2.4), analysis routines (Section 2.5), and performance metrics (Section 2.6) will all be discussed.

2.1 MOST Telescope

Design realizations in the MOST model can vary quite substantially. However, there are some similarities that exist amongst all designs. First, the MOST telescopes are Cassegrain telescopes. They are being designed to operate in the visible spectrum, with a nominal wavelength of 600 nm. All of the telescopes have a parabolic primary mirror, with a secondary mirror at the appropriate focus point. There is an optical

telescope assembly (OTA) containing all of the optical elements, and a bus to contain the supporting spacecraft subsystems. The relevant details of the rest of the structure and the analysis tools will be presented in this chapter.

2.2 Parametric Modeling Environment

The MOST modeling approach consists of a parametric framework in which a modular collection of MATLAB® functions interact to form a finite element model (FEM) of the structure, interface with Nastran to run a normal modes analysis, and create an integrated model. Many different control systems are implemented and analysis routines are run to yield a set of quantitative figure-of-merit outputs.

In order to allow for large tradespace examination, the entire process of creating the FEM, running the finite element analysis (FEA), creating the integrated model, and performing the analysis must be completely automated. Also, all design variables are parameterized and kept in a separate input file to easily create new design realizations. This type of automation has been utilized in other disciplines such as as weight estimation [45], structural optimization [19], and computational fluid dynamics [48]. The MOST model builds upon these concepts to create a completely automated parameter-input to figure-of-merit-output model to judge the ability of competing designs to meet the stringent requirements of these systems.

All input parameters are stored in a top level "Parameter" input file which flows down to the rest of the model, as seen in Figure 2-1. Each component of the model or analysis routine is contained within its own MATLAB function, making it easy to replace, upgrade, or add model components, performance metrics, and analysis routines. The shaded boxes represent the figure-of-merit outputs, while the other boxes represent various portions of the model and analysis.

The model generation and analysis is performed using multiple software programs. A flow of the model, as it relates to the analysis and the programs used, can be seen in Figure 2-2. The FEM is first created in MATLAB, where the grid points, element connectivities, and material properties are defined. Then, the software interfaces

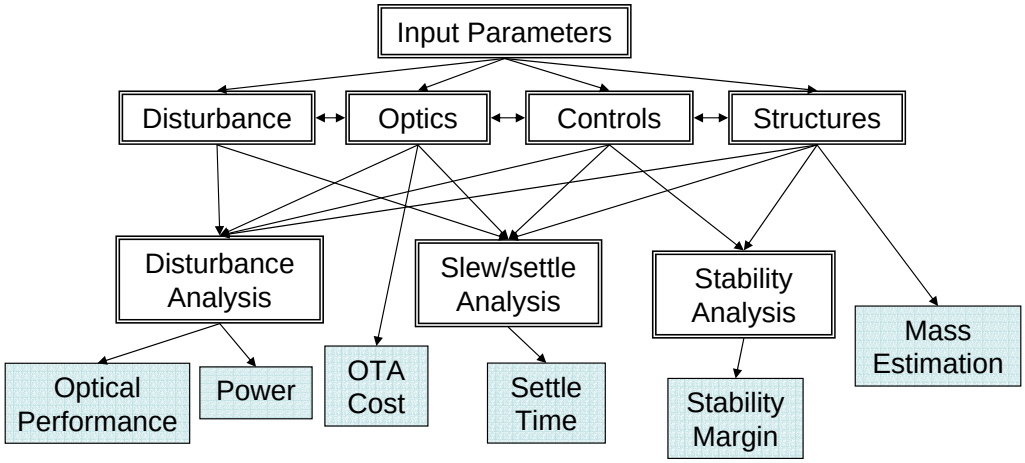

Figure 2-1: MOST Model Hierarchy

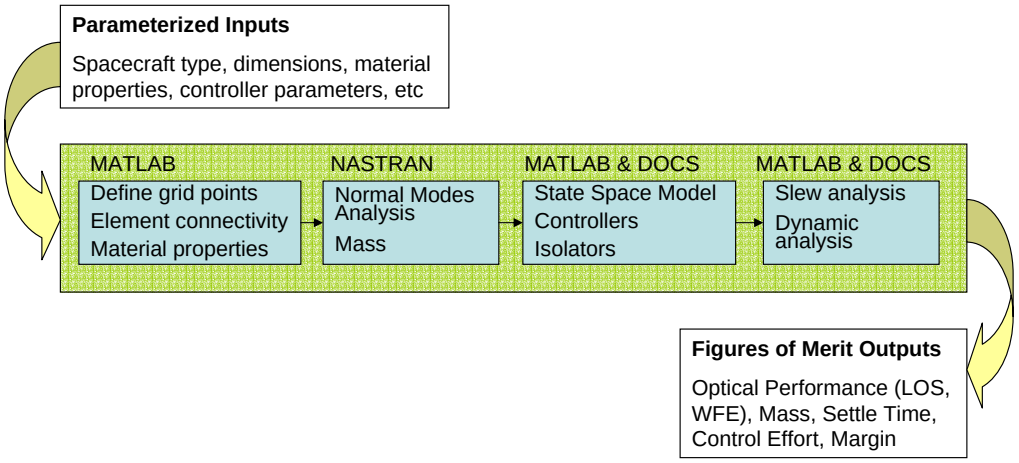

Figure 2-2: MOST Model Flow

with Nastran to run a normal modes analysis. The results of the FEA are brought back into MATLAB to create an integrated model using the Disturbance, Optics, Controls, and Structures (DOCS) toolbox [8]. Finally, slew and settle, disturbance, and stability analyses are run on the model using MATLAB and DOCS to determine the performance outputs.

This automated computational flow enables the quick analysis of many different space telescope realizations. Additionally, it allows for easy addition of new structural components, control systems, and analysis routines due to the modular nature of the code. As long as the input/output structure is maintained, new code modules can

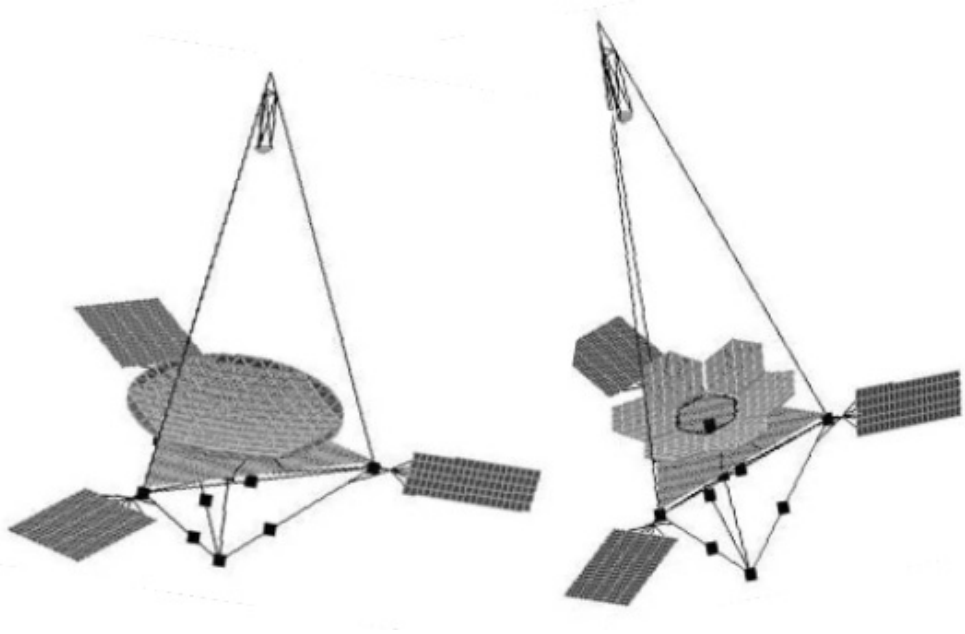

Figure 2-3: Sample Realizations of MOST Systems

be easily added or swapped. The inclusion of multiple disciplines, such as controls, structures, and optics, allows for the comparison of different types of metrics, which will be discussed in Section 2.6. The remainder of this section will focus on the relevant details of the MOST model.

2.3 Structural Finite Element Model

The MOST finite element model is created automatically based on the input parameters, so it can vary quite substantially. For example, a sample of two MOST realizations, with only two differing parameters, the $F\#$ and type of the primary mirror, can be seen in Figure 2-3. However, all models have the same basic form; the two fundamental sections of the system are an optical telescope assembly (OTA) and a bus. A schematic labeling the major structural components can be seen in Figure 2-4. A brief overview of a few of the key features in the model are discussed below.

The OTA is the payload of the system, with the focus being the optics. There are primary, secondary and tertiary mirrors. The secondary mirror is held above the

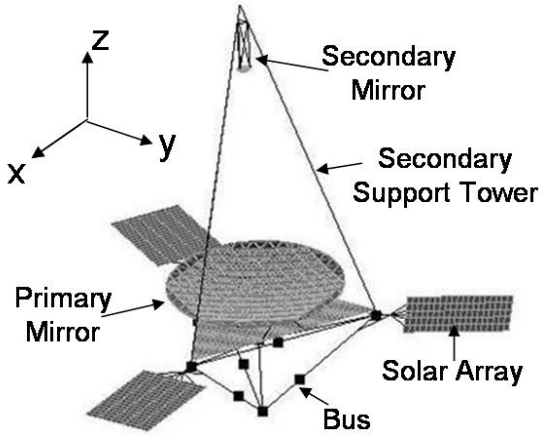

Figure 2-4: Key Structural Components of a Typical MOST Telescope

primary mirror by the secondary support tower (SST). This tower can have multiple forms including: tripodal; hexapodal; and circular, which are described in Reference [29]. There is an optics bench at the base of the SST. This bench holds optical instruments, including the tertiary mirror.

The tertiary mirror is an actuated, fast steering mirror (FSM) that has the ability to tip and tilt to correct for jitter in the optical path. The FSM is modeled as a concentrated mass with appropriate mass and inertia [12], and is connected to a strut on the optical bench. The concentrated mass is connected with a stiff spring element, about the tip and tilt rotational degrees of freedom. Then, when equal and opposite torques are applied to either side of the spring, the desired actuation is simulated and the FSM will rotate.

The primary mirror has been a major focus of the modeling effort. It is a rib-stiffened mirror. There is a thin face-sheet forming the optical surface, supported by a triangular pattern of tall, thin ribs that provide stiffness without substantially adding mass. Both the number and the size of the ribs are variable. Additionally, there is a surface-parallel piezo-electric actuator embedded in the edge of each rib furthest from the face sheet, as seen in Figure 2-5. When a voltage is applied, the actuators expand, creating a moment on, and thus bending the surface of the mirror. This can be used to correct for both quasi-static thermal deformations and dynamic deformations of the primary mirror.

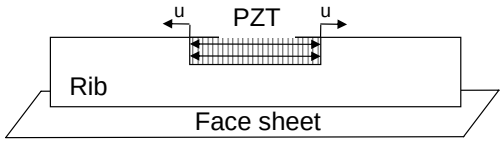

Figure 2-5: Schematic of a Piezo-electric Actuator Embedded in the Mirror Rib

The primary mirror is either an annular monolith or composed of segmented hexagonal mirror petals. The type of aperture can be changed by a single parameter in the input file. The monolithic mirror is connected to the structure through three kinematic bipods that connect directly to the mirror and the OTA structure. In the case of the segmented system, there are six hexagonal petals cantilevered off a center ring. Each of these connections contains a torque actuator (co-located with a stiff spring) that can be used to correct for deployment misalignments and control the rotations of the petals. The center ring is then connected to the OTA structure through three bipod connections. The monolithic and hexagonal mirrors, with key connection points labeled, can be seen in Figures 2-6 and 2-7.

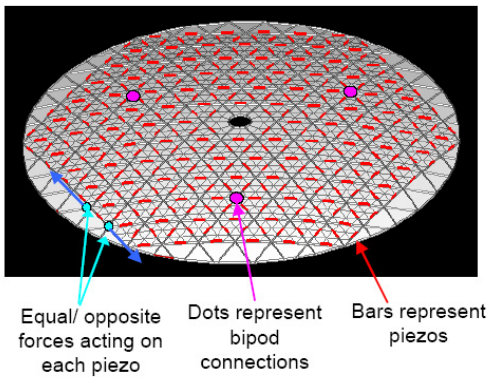

Figure 2-6: Annular Monolithic Primary Mirror

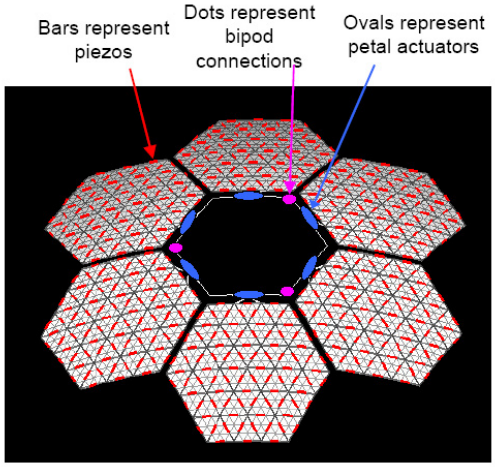

Figure 2-7: Segmented Hexagonal Primary Mirror

The kinematic bipods, used with both types of primary mirrors, help to mitigate the transference of disturbance energy from the structure to the aperture. The bipods constrain motion in the vertical (z) and circumferential (θ) directions. There is a soft spring connecting the radial (r) and rotational degrees of freedom. The

spring connects, but does not rigidly constrain, the motion in these degrees of freedom. Specifically, the soft degrees of freedom of the bipods essentially have zero stiffness, so deformation of the OTA structure only creates rigid body motion of the primary mirror. These connections help decouple quasi-static deformations in the mirror from those in the structure, while still constraining all six degrees of freedom of the aperture.

The second major component of the telescope structure is the bus. The bus is connected to the OTA through an isolator, which is described in Section 2.4. The bus is tetrahedral in shape and is modeled as a series of struts and concentrated masses. The concentrated masses represent the mass of the spacecraft subsystems (avionics, communications, propulsion, etc.) that are not modeled in detail. The bus concentrated masses are sized in accordance with the mass of the OTA, as a more massive OTA would generally require larger bus instruments.

There are three low frequency solar panel appendages attached to the bus. The panels are roughly sized to provide 1000 Watts of total power [32]. Flexible appendages are common on space systems and include components such as solar panels, communications antennas, and radiators. Flexible appendages can greatly affect the dynamics of the system, so solar panels are included in the MOST model to account for these types of flexible dynamics. These appendages have variable frequency, but are typically analyzed with a fundamental frequency of 0.5 Hz.

The reaction wheel assembly (RWA), composed of five reaction wheels, is located in the center of the bus and is connected through a second isolator. The RWA is the actuator that is used for slewing maneuvers and attitude control, and is also the primary source of dynamic disturbance in the MOST model. The reaction wheels are sized to accommodate the desired slewing maneuvers, and are thus based on the inertia and mass of the system (Section 4.1.1). The disturbance model is constructed based on the harmonics of the imbalance in each wheel [40]. This disturbance model is allowed to vary with the mass of the wheels, so if more massive wheels are required to maneuver the spacecraft, a penalty is paid in terms of greater disturbance energy.

The structural model includes the key features necessary to examine the perfor-

mance of light-weight, highly controlled space telescopes. It also maintains enough simplicity and generality to be applied to a large number of designs and be analyzed quickly, thus making it useful for parametric modeling.

2.4 Integrated Model

The next step in the analysis is the creation of an integrated model. Once the structural FEM is created, a normal modes analysis is run using Nastran. Nastran determines the mass and stiffness matrices of the FEM based on the defined element geometry, connectivities, and material properties. The dynamic equations of motion are given by:

$$M\ddot{\eta}(t) + K\eta(t) = 0 \tag{2.1}$$

where M is the mass matrix, K is the stiffness matrix, and η are the global degrees of freedom. This formulation assumes no forcing inputs and allows the calculation of the natural frequencies and mode shapes of the system.

This solution proceeds in the following manner. First, a sinusoidal solution is assumed:

$$\eta_n(t) = \phi_n sin(\omega_n t) \tag{2.2}$$

$$\ddot{\eta}_n(t) = -\omega_n^2 \phi_n sin(\omega_n t) \tag{2.3}$$

Substituting Equations 2.2 and 2.3 into Equation 2.1 yields:

$$-\omega_n^2 M\phi_n + K\phi_n = 0 \tag{2.4}$$

Here, ϕ_n is the n^{th} mode shape and ω_n is the corresponding natural frequency for the n^{th} mode. All of the frequencies and mode shapes can be combined into matrices, and Equation 2.4 can be rewritten as:

$$(K - \Omega^2 M)\Phi = \mathbf{0} \tag{2.5}$$

where Ω is the diagonal matrix of all of the modal frequencies, and Φ is the matrix containing all of the mode shapes.

This is an eigenvalue problem; Nastran solves for the frequencies and mode shapes for a user-specified number (200) of modes in the model. These modal frequencies and mode shapes are imported into MATLAB. Then, the DOCS [8] toolbox is used to create the MOST integrated model by combining the frequencies and mode shapes with uniform modal damping, input channels (actuator and disturbances), and output channels (sensors and performance metrics). The state space model can be written as follows:

$$\begin{aligned}
\begin{bmatrix} \dot{x} \\ \ddot{x} \end{bmatrix} &= \begin{bmatrix} 0 & I \\ -\Omega^2 & -2\zeta\Omega \end{bmatrix} \begin{bmatrix} x \\ \dot{x} \end{bmatrix} + B_u u + B_w w \\
y &= C_y \begin{bmatrix} x \\ \dot{x} \end{bmatrix} + D_{yu} u + D_{yw} w \\
z &= C_z \begin{bmatrix} x \\ \dot{x} \end{bmatrix} + D_{zu} u
\end{aligned} \tag{2.6}$$

where x are the modal coordinates obtained from $\eta(t) = \Phi x(t)$, Ω is the diagonal matrix of modal frequencies, ζ is the prescribed damping ratio of 0.5%, u are the control inputs, w are the white-noise disturbances, y are the control sensor outputs, and z are the figure-of-merit outputs.

Since the system is operating in space, it is not constrained or connected to anything. Therefore, there are six rigid body modes of the system (three translational, and three rotational). These rigid body modes have zero frequencies, and thus make the A matrix singular. The rotational rigid body modes are observable, and are stabilized by the ACS controller (Section 3.1). The translational rigid-body modes are unobservable to the outputs, and are truncated from the system.

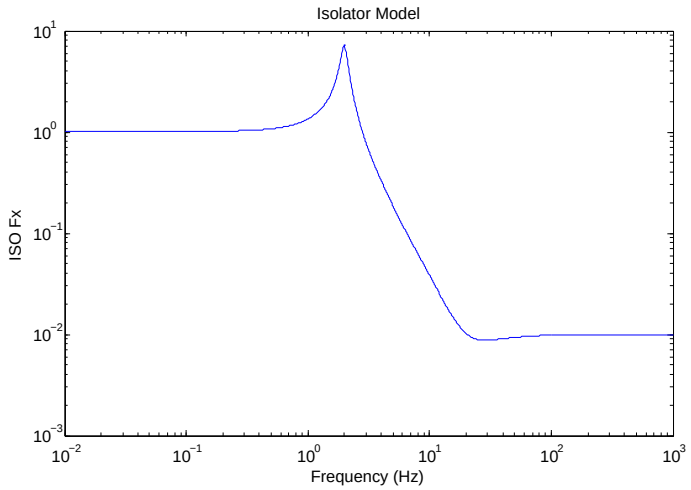

Figure 2-8: Isolator Used in MOST State Space Model

Once the state space model of the plant is created, the isolators and control systems are added to the model. They are also implemented as linear, state-space systems. There are up to four control systems and two isolators for each telescope realization. The two isolators (one between the RWA and the bus, the other between the bus and the OTA) are implemented as low pass filters that level out at high frequencies, as seen in Figure 2-8. The disturbances (in x, y, and z axis forces and torques) are filtered through the isolator. The isolator corner frequencies are variable, but the defaults are two hertz for the bus isolator and ten hertz for the RWA isolator; this combination has been shown to have desirable interaction characteristics between the two isolators [52, 55]. The four control systems are: attitude control (ACS), fast steering mirror control (FSM), wavefront control, and petal control. The control systems will be discussed in detail in Chapter 3.

The plant, formed from the Nastran normal modes analysis with inputs and outputs, along with the control systems and isolators, are combined to create the MOST integrated model. The control system loops are connected using DOCS with a positive feedback convention as seen in Figure 2-9. All of the sensor outputs feed back through the control systems to create the control commands (u). The control commands are fed back to the plant, and, when these loops are closed, the entire integrated model reduces to:

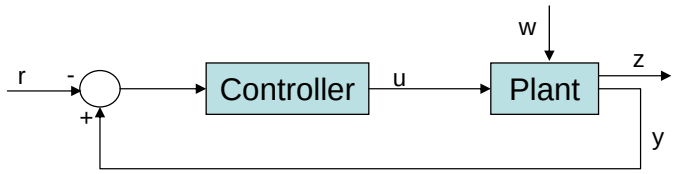

Figure 2-9: Block Diagram of the MOST Integrated Model with the Control Loops Implemented in a Positive Feedback Convention

$$\begin{aligned} \begin{bmatrix} \dot{x} \\ \ddot{x} \end{bmatrix} &= A \begin{bmatrix} x \\ \dot{x} \end{bmatrix} + B_w w \\ z &= C_z \begin{bmatrix} x \\ \dot{x} \end{bmatrix} \end{aligned} \tag{2.7}$$

This fully integrated model is used for a variety of analyses that will be described subsequently.

2.5 Analysis Routines

Once the integrated model is created, the analysis routines are run on the model to determine the performance outputs. There are three general analysis routines considered: slew and settle analysis, dynamic disturbance analysis, and stability robustness analysis. Each will be discussed briefly, and their corresponding performance metrics will be discussed in Section 2.6.

The slew and settle analysis is a time domain simulation of the spacecraft undergoing a slewing maneuver. The slewing involves pointing the spacecraft to another location, or changing the angular position by a specified amount. The settle time is defined as the amount of time that it takes for the vibrations, resulting from the slew, to attenuate. Once the vibrations have attenuated, the telescope can return to operations. The input torque commands can be generated in a variety of different ways, including feed-forward techniques that minimize the residual vibrations after

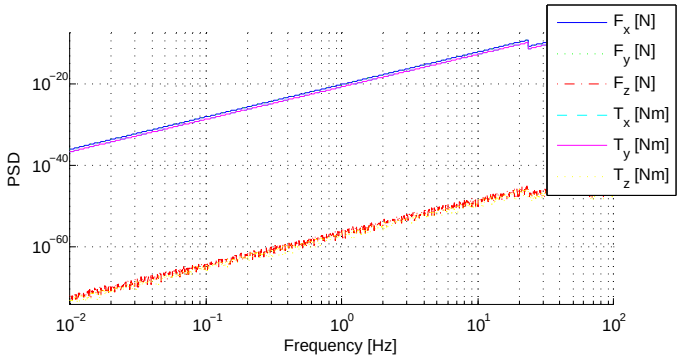

Figure 2-10: PSD for Reaction Wheel Forces and Torques

the slew. Each slew has a specified angular distance and time for completion. The simulation calculates the time-domain histories of key optical performance metrics both during the slewing maneuver and after the slew is complete. This is used to examine the resultant vibrations and system settling characteristics and compare them with requirements. This analysis is described more completely in Chapter 4.

The steady-state dynamic disturbance analysis comprises the bulk of the analysis. The disturbance is described in terms of a power spectral density (PSD) of the reaction wheel assembly in all six degrees of freedom (x, y, z forces and torques about those axes). The PSD is formed from the reaction wheel imbalance harmonics (Section 4.1.1) [40]. A time-averaged, broad-band, steady-state disturbance model that is valid across all frequencies, rather than only at specific harmonic frequencies, is derived from the harmonics of the reaction wheel imbalance [23]. A sample of the disturbance model can be seen in Figure 2-10.

The integrated state-space model is transformed into a frequency domain transfer function matrix as follows:

$$G_{zw} = C_z(sI - A)^{-1}B_w \tag{2.8}$$

The PSD of the output can then be found using:

$$S_{zz} = G_{zw} \cdot S_{ww} \cdot G_{zw}^H \tag{2.9}$$

where S_{zz} is the PSD of the output, S_{ww} is the PSD of the disturbance input (Figure 2-

10), G_{zw} is the system transfer function matrix, and ^{H} is the hermitian operator. The mean squared value of the outputs can then be found [10]:

$$\bar{z_i^2} = \frac{1}{2\pi}\int_{-\infty}^{+\infty} S_{zz}(j\omega)_{i,i}d\omega = \frac{1}{\pi}\int_{0}^{+\infty} S_{zz}(j\omega)_{i,i}d\omega \tag{2.10}$$

The square root of $\bar{z_i^2}$ yields the root-mean-square value of the output. The output metrics determined from this analysis will be discussed more in Section 2.6.

The final analysis is a stability robustness analysis. This analysis is a substitute for gain and phase margin of the system, as multi-input, multi-output (MIMO) gain and phase margins are often ambiguously defined and difficult to calculate. Instead, the maximum singular value of the sensitivity transfer function is used as a substitute. The exact formulation is described in Section 2.6.2. The stability robustness analysis contributes to the determination of the cost of including control; it indicates the stability margin in each design.

These analyses combine to allow for quantitative analysis of the different space telescope realizations. They cover a range of analysis types and allow the determination of both performance and programmatic performance outputs. The performance metrics used to distinguish between designs will be discussed next.

2.6 Performance Metrics

The performance metrics represent many important aspects of space telescopes. They include optical performance metrics which are the classical performance requirements for space telescopes. Additionally, control metrics, including stability margin and power consumption, and programmatic metrics such as mass, cost and operational availability are examined. These additional metrics help to better depict the overall performance of the systems, including costs associated with improving optical performance.

2.6.1 Optical Performance Metrics

The optical performance metrics are the classic metrics that specify the optical quality of the telescope. The two optical metrics considered are line-of-sight jitter (LOS) and wavefront error (WFE).

Line of Sight Jitter

The LOS jitter can be thought of as the error due to vibrations of the entire OTA. It is approximated using the rotations and translations of points on the primary, secondary, and tertiary mirrors via the following equations [44]:

$$\begin{aligned} LOS_x &= -\frac{1}{f_1}\delta_{P_y} + \frac{(M-1)}{Mf_1}\delta_{S_y} + \frac{1}{Mf_1}\delta_{T_y} + \\ &\quad 2\alpha_{P_x} - \frac{2}{M+1}\alpha_{S_x} - \frac{2}{M+1}\alpha_{T_x} \\ LOS_y &= \frac{1}{f_1}\delta_{P_x} - \frac{(M-1)}{Mf_1}\delta_{S_x} - \frac{1}{Mf_1}\delta_{T_x} + \\ &\quad 2\alpha_{P_y} - \frac{2}{M+1}\alpha_{S_y} - \frac{2}{M+1}\alpha_{T_y} \end{aligned} \tag{2.11}$$

where f_1 is the focal length of the primary mirror, M is the secondary mirror magnification, and δ are the translations and α are the rotations of points on the primary mirror (P), secondary mirror (S), and tertiary mirror (T). The three points utilized in this formulation can be seen in Figure 2-11.

This LOS jitter value is calculated by using the appropriate C_z matrix in the state space formulation of the integrated model. Then, the LOS jitter about the x and y axes are computed using the dynamic disturbance analysis.

The target value for the LOS jitter, assuming a three meter diameter mirror, is 1.6 milli-arcseconds (mas). The jitter requirement is calculated using the angular resolution of a diffraction-limited optical system:

$$\theta_{res} = \frac{1.22\lambda}{D} \tag{2.12}$$

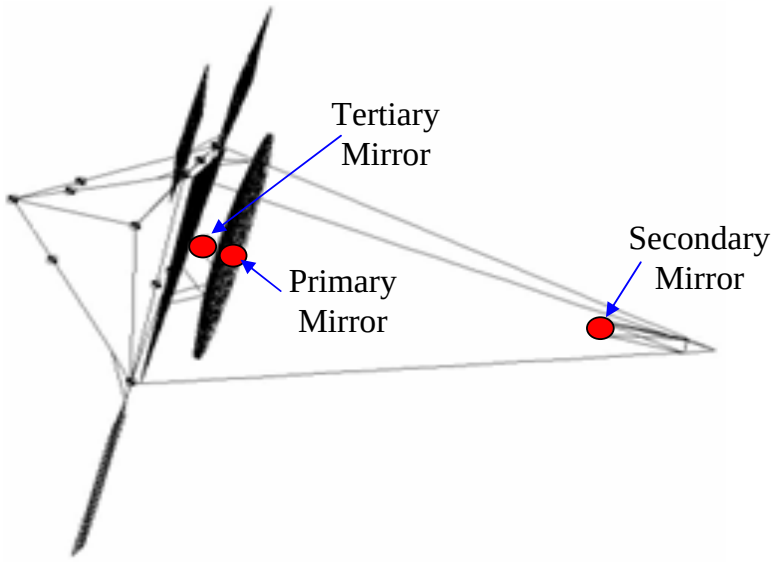

Figure 2-11: Points Used for the Line-of-Sight Jitter Calculation

Here, θ_{res} is the angular resolution, λ is wavelength and D is diameter. The pixel size roughly corresponds to the angular resolution, and smearing light across more than one pixel is undesirable. Therefore, the jitter needs to be less than the angular resolution. The LOS requirement can be created by using θ_{res} as a 3-σ value. This requires the LOS jitter to be less than θ_{res} for 99.7% of the time.

It is also assumed that the error due to the effects of the dynamics, which are accounted for by the model, are allocated only 10 % of the total LOS error budget. Other error contributions include sensor noise, unbalanced solar pressure and drag toruqes. Therefore, since the disturbance analysis provides 1-σ values, $\lambda = 600$ nm, and $D = 3$ m, the 1-σ LOS requirement is 1.6 mas.

$$LOS_{req} = 10\% \cdot \frac{1}{3} \cdot \frac{1.22 \cdot 600 \cdot 10^{-9}}{3} = 8.13 \cdot 10^{-9}\text{rad} = 1.6\text{mas (1-}\sigma\text{)} \qquad (2.13)$$

The 1-σ LOS jitter output from the dynamic disturbance analysis is compared with the 1.6 mas requirement to judge the LOS performance of each system.

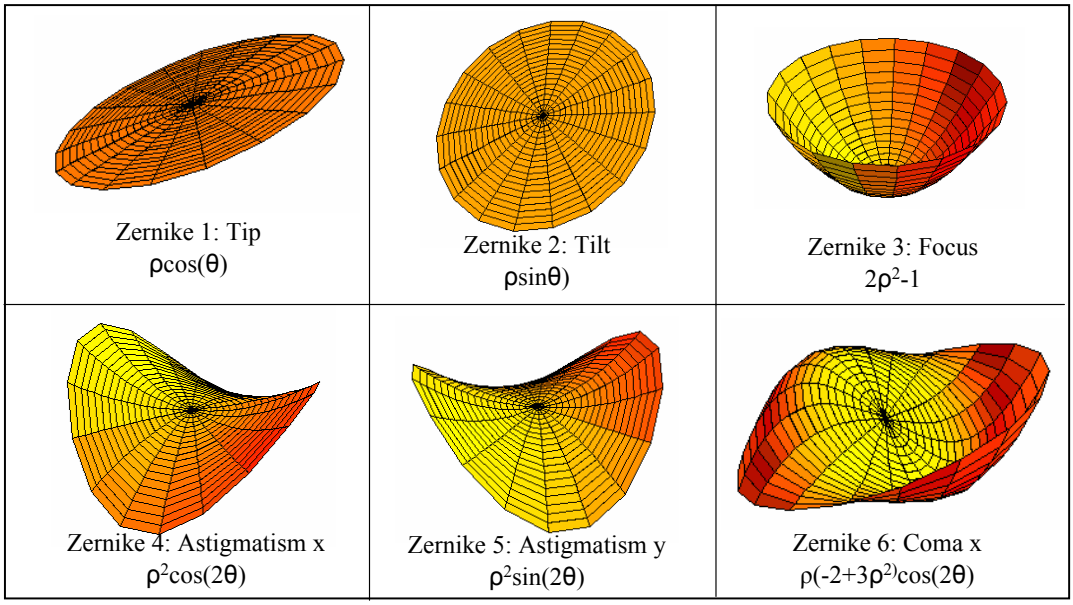

Figure 2-12: First Six Zernikes Used for Wavefront Error Calculation

Wavefront Error

The second optical performance metric is wavefront error (WFE). Wavefront error accounts of the distortions of the mirror surface. For MOST, only the distortions of the primary mirror are considered. The wavefront error is calculated using the first 48 Zernikes of the primary mirror. The Zernikes, which are a set of optical basis functions [57], are calculated using the z-translations (see Figure 2-4) of all of the nodes on the surface of the primary mirror. The Zernikes decompose the surface of the mirror into a set of orthogonal shapes; the first few can be seen in Figure 2-12. In the figure, ρ is the radial distance from the center of the mirror, and θ is the angular distance around the circumference of a circle of radius ρ. Each Zernike shape has a weighting that is used to determine the error resulting from the particular deformation.

The disturbance analysis yields the mean-square amplitude of each Zernike as seen in Figure 2-13. Then, the WFE is calculated using the root-sum-square of the Zernike output values.

$$WFE = \sqrt{\sum (w_i \cdot z_i)^2} \tag{2.14}$$

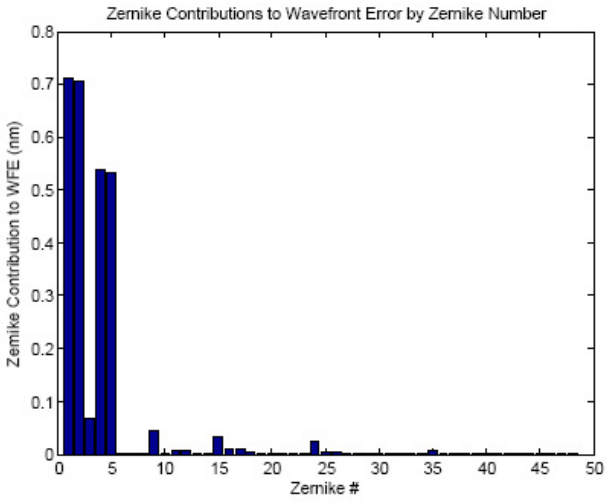

Figure 2-13: Wavefront Error Contribution of Each Zernike

where z_i are the coefficients of each Zernike from the disturbance analysis and w_i are the weightings of each Zernike [3].

The target value for wavefront error is 1.0 nm, which is obtained using the following relation:

$$WFE_{req} = \frac{\lambda}{20} \tag{2.15}$$

Again, this requirement is treated as a 3-σ value to ensure that the WFE meets the requirement 99% of the time. Therefore, with the 1-σ value provided by the model, allocating only 10% of the requirement to the dynamics budget, and $\lambda = 600nm$:

$$WFE_{req} = 10\% \cdot \frac{1}{3} \cdot \frac{600 \cdot 10^{-9}}{20} = 1\text{nm} \tag{2.16}$$

In both the LOS jitter and WFE calculations, only 10% of the error is allocated to the dynamics. Other sources of error not considered here that contribute to the other 90% of the error include thermal deformations, mis-alignment, manufacturing flaws, optical contamination, unbalanced solar pressure and drag torque, and sensor noise.

2.6.2 Control Metrics

Adding control to the system can greatly improve performance of the optical metrics and allow for new systems and technologies to meet requirements. However, adding control has associated costs. Two such costs are considered here; the first is stability margin, obtained using the sensitivity transfer function, and the second is control effort.

Sensitivity and Stability Margin

The sensitivity metric is a measure of stability margin. It is desirable to have a metric that quantitatively determines how close the system is to instability, and to see how the control systems alter the stability margin. To define the sensitivity, a singular value decomposition of the sensitivity transfer function matrix is performed at each frequency. The maximum singular values at each frequency are then collected into a frequency domain function. The maximum of this function, over all frequency, corresponds to $\bar{\sigma}$, or the sensitivity:

$$\bar{\sigma} = max_{\omega}(\sigma_{max}(I - GK)^{-1}) \tag{2.17}$$

where ω is frequency, σ_{max} is the maximum singular value, and $(I - GK)^{-1}$ is the sensitivity transfer function for a positive feedback system (G is the plant, K is the controller). The maximum singular value of the sensitivity transfer function is a function of frequency, and the frequencies with high values correspond to frequencies where instability may be an issue, as seen in Figure 2-14.

The sensitivity can be used to approximate the MIMO gain margin (GM) and phase margin (PM) of the system as follows[37]:

$$GM \approx \frac{\bar{\sigma}}{1 \pm \bar{\sigma}} \tag{2.18}$$

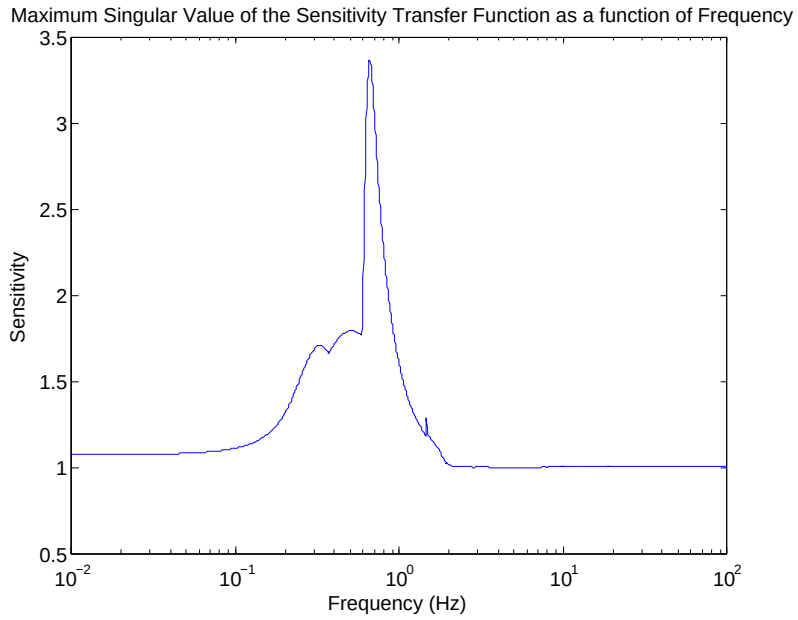

Figure 2-14: Maximum Singular Value of the Sensitivity Transfer Function as a Function of Frequency

$$PM \approx \pm arccos\left(1 - \frac{1}{2}\left(\frac{1}{\bar{\sigma}}\right)^2\right)$$

These approximations are rather conservative; they assume uncertainty in the plant in all directions, even those that are physically impossible. Therefore, they provide a lower bound on the stability margin.

Using these rather conservative approximations, a sensitivity of two corresponds to roughly 6 dB of gain margin and 30 degrees of phase margin. Therefore, a conservative estimate for the sensitivity requirement is that it be less than two. However, experimental results suggest that, for some systems, sensitivity can be pushed as high as ten before instability becomes a concern [42].

Control Effort

The second control metric is control effort. The control effort is used to approximate the forces and torques that the actuators must apply to achieve a given amount of control. It is the quadratic output of each actuator channel that is calculated through the dynamic disturbance analysis. In this analysis, the control efforts are normalized

for each type of actuator by the mean value and then summed together. With further extensions, a constant relating the mean square force or torque to the required power could be introduced in order to convert this metric into a true power metric.

High control effort not only means more power, but can also imply more complexity. The power system must provide additional power, making it bigger and possibly more complex. Also, the likelihood of actuator fatigue increases, requiring the actuators to have longer lifetimes and increased reliability.

The inclusion of control metrics in the analysis ensures that the price of adding control is included in the analysis so that real conclusions on the benefits and detriments of control can be drawn. Without such metrics, controls may be applied indiscriminately to continually improve optical performance, which could potentially lead to adverse effects and even instability.

2.6.3 Programmatic Metrics

In addition to the optical performance and control metrics mentioned, future space telescopes also have to meet increasingly demanding programmatic requirements. MOST strives to include some of these programmatic metrics in order to fully consider all trade-offs.

Mass

The first programmatic metric is mass. The mass is calculated directly using the finite element model in Nastran. The mass of the modeled components are based on the size and material properties. Parts of the system, such as the bus, use concentrated masses to account for the mass of components that are not modeled in detail. These masses are sized based on the mass of the payload to obtain an accurate representation of the system mass (larger payloads require more massive supporting subsystems). The mass is important because launch costs are largely proportional to mass, thus it is desirable to have a low-mass design.

Relative OTA Cost

The second metric is relative OTA cost. As mentioned above, the launch costs are largely proportional to mass, and mass can even be used to approximate a relative cost between similar systems. However, when systems are dissimilar and have different aperture types or mirror curvatures, the cost of manufacturing the mirror varies substantially. Therefore, a metric was developed to include the manufacturing cost of the mirror. There have been cost models developed for manufacturing ground-based mirrors [49]. These cost relations can be used for a relative, but not absolute, cost analysis of space-based mirrors,

$$Cost \propto n_{segs} D^{1.8} Z^{1.04} \tag{2.19}$$

where n_{segs} is the number of segments in the primary mirror, D is the diameter of the mirror or mirror segment, and Z is the mirror sagitta, which is based on the mirror F # and conic constant. It is important to note that this cost is not an absolute cost, only a proportionality. However, it allows the determination of a portion of the relative cost and comparison between different architectures.

Slew and Settle Time

The final metric considered is slew and settle time. The slew and settle time serves as a metric for mission operations. When a system is performing a slew, or settling after a slew, it cannot be operating. Therefore, the total time it takes to complete the slew and return to operations can serve as a measure for the amount of time the system is not operational. The slew and settle time is obtained using a time simulation of various slewing maneuvers to determine the total amount of time it takes to return to operations. This metric is more fully described in the Slew and Settle Analysis Chapter (Chapter 4).

2.7 Summary

This chapter provides a general description of the MOST model that is used in the remainder of the thesis. The model is completely parametric and includes a structural FEM, normal modes analysis, integrated state space model, and analysis routines to quantitatively determine a number of potentially conflicting performance requirements. This framework is used to examine the effects of various control systems in order to create telescope systems with good performance across all output metrics. Specifically, it is used to balance between the different control systems discussed in Chapter 3 so that the LOS jitter, WFE, and settle time are minimized, while still keeping the sensitivity less than two and the mass, OTA cost, and control effort low.

Chapter 3

Control Systems

Lightweight telescope systems are desirable for launch, but as systems become more lightweight, they also tend to become more flexible. Flexibility causes more vibrations at lower frequencies, which tends to degrade performance. The loss in performance due to flexibility can be counteracted by adding control. However, there are many different areas where control could potentially be added. Here, four different controllers are considered: attitude control, fast steering mirror control, wavefront control, and petal control. The following chapter will describe these four different controllers, their implementation in the MOST model, and their individual effects. Then, Chapter 5 will address integration of these controllers.

The controllers are implemented sequentially, and are examined individually, to the furthest extent possible. The attitude control must remain active at all times, to stabilize the rigid body attitude modes. Therefore, when the ACS system is analyzed, the other three controllers are inactive. When any of the other three controllers are analyzed, only the ACS and the controller of interest are active.

3.1 Attitude Control System

The attitude control system (ACS) is a necessary control system; it stabilizes the rigid body rotations of the telescope, preventing small disturbances from creating large rotations. Therefore, it is imperative to have some ACS control at all times. The

ACS is also responsible for performing the slewing maneuvers. The control system mitigates the error between the desired and actual attitude in both the steady-state and slewing modes.

The ACS actuator is the reaction wheel assembly (RWA). The RWA consists of five reaction wheels whose speed, and thus angular momentum, can vary. This causes a torque on the system that can be used for control actuation. The ACS sensor is an angular sensor, sensing θ_x, θ_y, and θ_z, and is located on the outside of the bus.

The ACS controller is a proportional-derivative (PD) controller with inertial decoupling (defined below) and roll-off poles. The controller has variable bandwidth and a nominal damping ratio of 0.707. The state space implementation is as follows:

$$\begin{aligned} \dot{x_c} &= A_c x_c + B_c y \\ u &= -C_c x \end{aligned} \tag{3.1}$$

where x_c is the vector of controller states, y is the vector of sensor readings, u is the vector of control commands, and A_c, B_c, and C_c are defined as follows:

$$\begin{aligned} A_c &= \begin{bmatrix} 0 & I \\ -\omega_b^2 & -2\zeta_c\omega_b \end{bmatrix} \\ B_c &= \begin{bmatrix} 0 \\ \omega_b^2 \end{bmatrix} \\ C_c &= \begin{bmatrix} K_p & K_v \end{bmatrix} \end{aligned} \tag{3.2}$$

Here, ω_b is the controller bandwidth, ζ_c is the controller damping ratio, K_p is the proportional gain, and K_v is the velocity gain. K_p and K_v are defined as:

$$K_p = w_b^2$$

$$K_v = 2\zeta_c w_b \tag{3.3}$$

The controller must control all three attitude degrees of freedom, so these matrices are extended, resulting in a six-state controller.

The controller implementation above assumes that the system needs to be controlled identically about the x, y, and z axes. In other words, this controller would work well for a system with a diagonal inertia tensor with identical inertias about all three axes. However, the spacecraft body axes are not necessarily the principle axes of the system. Also, the system is not perfectly symmetric, so the inertia is likely to be larger in certain directions. Therefore, in order to account for the different inertias about the three attitude axes, an inertial decoupling is implemented as follows:

$$P = V \cdot D^{1/2} \tag{3.4}$$

where V are the eigenvectors and D are the eigenvalues of the 3×3 system inertia tensor. Then, the control system is modified as follows:

$$\begin{aligned} \dot{x_c'} &= A_c x_c' + B_c P' y \\ u &= -P C_c x_c' \end{aligned} \tag{3.5}$$

Here, A_c, B_c, and C_c are the matrices calculated in Equation 3.2. This inertially decouples the controller and accounts for the magnitudes of the components of the inertia in all directions.

An example of the frequency response of the controller can be seen in Figure 3-1. The corresponding system inertia matrix is:

$$I_{sc} = \begin{bmatrix} 573 & 0.8 & 0.1 \\ 0.8 & 573 & 0.2 \\ 0.1 & 0.2 & 752 \end{bmatrix} kg \cdot m^2 \tag{3.6}$$

As visible in Figure 3-1, the magnitudes of the controller are largest along the

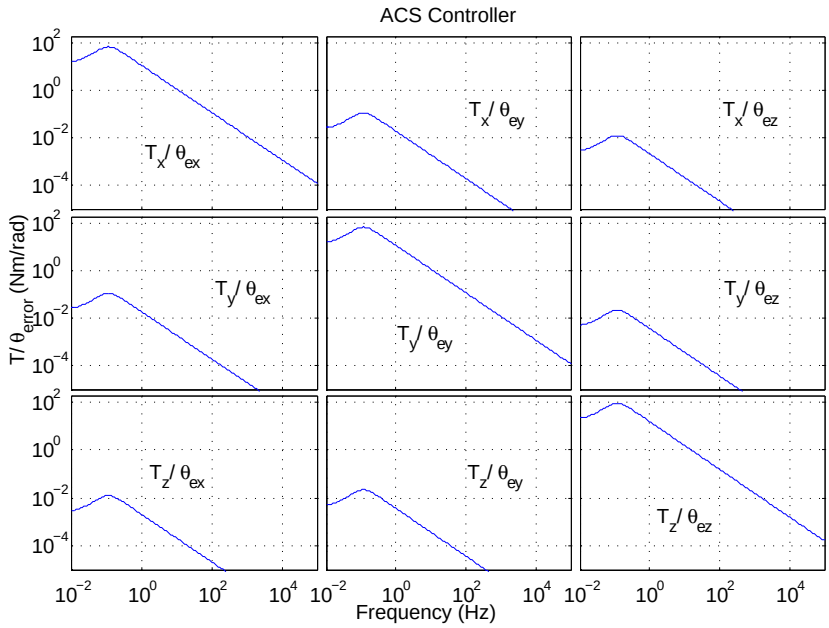

Figure 3-1: Frequency Response of the ACS Controller with Inertial Decoupling

diagonal (θ_x input to T_x output, etc.), consistent with the fact that the inertia matrix has its largest components along the diagonal. The off-diagonal terms of the inertia tensor have very small values, and, thus, also small magnitudes in the ACS controller.

The main variable in the ACS controller is the bandwidth. The bandwidth adjusts the frequency region in which the controller is active. Additionally, higher bandwidth increases the gains, and thus increases the magnitude of the frequency response of the controller. An example of the frequency responses of three different ACS bandwidths are shown in Figure 3-2. The ACS bandwidth is the "knob" that allows variation in the amount of control applied, and thus affects the performance of the system.

The ACS controller can improve LOS jitter, WFE, and settle time, but, as with all controllers, performance improvement comes at the expense of sensitivity and control effort. Of all of the performance metrics, the ACS controller most strongly affects the settle time, since the slewing maneuver is performed by the ACS controller and the ACS controller is responsible for settling the vibrations after the slew.

It is assumed that the sensitivity (stability margin) is a more limiting factor than the control effort in determining the amount of control that can be utilized because increasing the sensitivity too much results in instability, whereas an increase in control

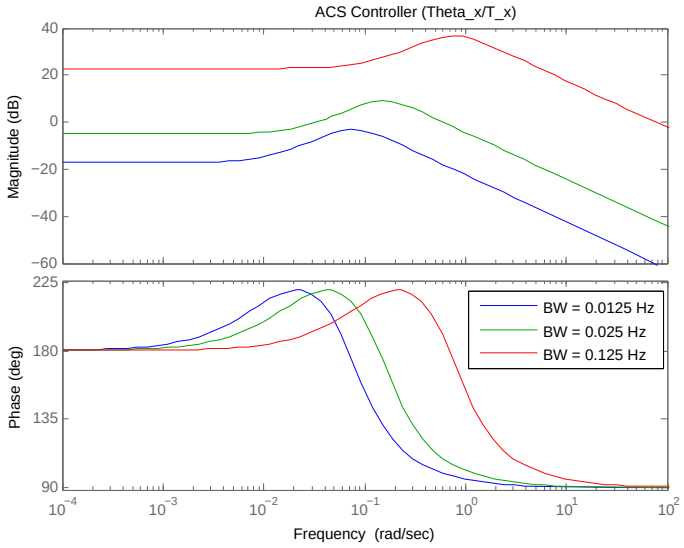

Figure 3-2: Frequency Response of ACS Controller at Multiple Bandwidths

effort results in more power consumption, which is not as severe of a problem as instability. Therefore, the sensitivity and settle time can be examined together as a cost versus performance analysis to discover the trade-off between the two metrics. Figure 3-3 illustrates this. When the ACS bandwidth is very low (0-0.2 Hz), the settle time decreases with increasing bandwidth. The sensitivity appears to remain constant in this region, but actually is slightly increasing. At values of ACS bandwidth near 0.5 Hz, the frequency of the first solar panel mode, the ACS controller interacts with the low frequency appendage mode and causes very poor behavior. As the ACS bandwidth is pushed higher than the solar panel mode, the settle time becomes extremely fast. However, even though the sensitivity returns to a more acceptable range, it is about twice as high as it was before the solar panel mode, indicating that the system is much closer to instability.

The control effort can also be examined as a function of bandwidth. This can be seen in Figure 3-4. As expected, increasing the bandwidth dramatically increases the control effort utilized. There is a small bump in the control effort near the solar panel mode frequency where more control must be exerted to control the system because of the appendage vibration. Otherwise, it is monotonically increasing, as expected. The ACS control can improve the settle time. However, it causes increases in both

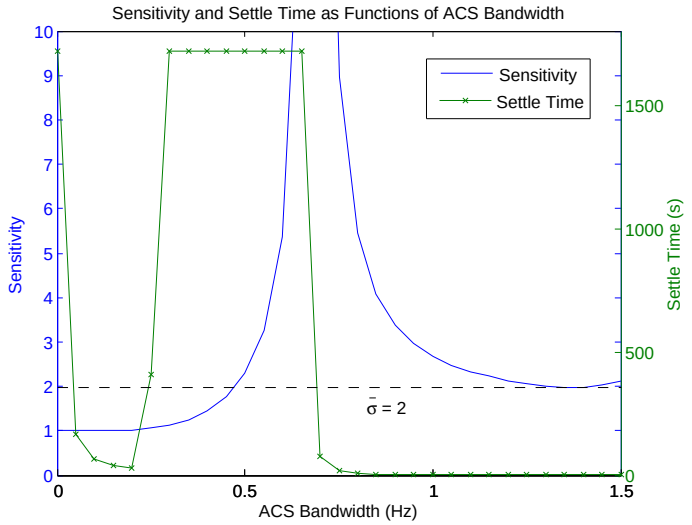

Figure 3-3: Sensitivity and Settle Time as Functions of ACS Bandwidth

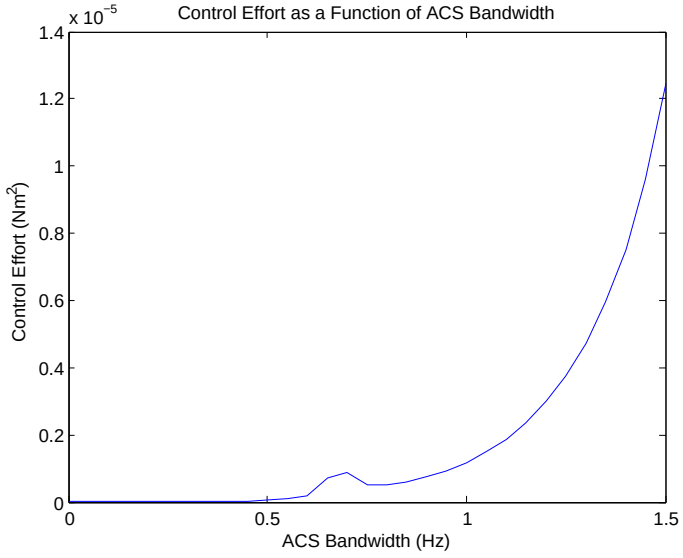

Figure 3-4: Control effort as a function of ACS bandwidth

sensitivity and control effort, and thus should be increased with caution.

3.2 Fast Steering Mirror Control

The fast steering mirror (FSM) is the tertiary mirror of the system. The entire tertiary mirror can tip and tilt as a rigid body. This motion can be performed at high frequency, and can be used to correct for errors in the optical path. FSMs are commercially available from companies such as Physik Instruments [25] and Ball Aerospace [1]. These mirrors can have bandwidths up to 1000 Hz, which allows for high-bandwidth correction in the LOS jitter.

The FSM control actuator is the actual FSM. It is implemented as a concentrated mass, sized at 0.055 kg with an inertia calculated using a radius of 4 cm and a height of 10 cm, which is the size of a commercially available FSM [12]. The concentrated mass is connected to a strut on the optics bench that is directly beneath the center of the primary mirror. This connection has a stiff spring about the tip and tilt (θ_x and θ_y) degrees of freedom. The θ_z and three translational degrees of freedom are connected rigidly. Equal and opposite torques are applied to either side of the spring to actuate the FSM.

The FSM controller sensor is the line-of-sight jitter performance metric described in Section 2.6.1. The tertiary mirror rotation is directly a part of the metric (Equation 2.11), so the FSM controller can directly compensate for errors due to jitter.

The FSM controller is a PD controller. It is implemented in a similar manner as the ACS controller:

$$\begin{bmatrix} \dot{x}_{c1} \\ \ddot{x}_{c1} \\ \dot{x}_{c2} \\ \ddot{x}_{c2} \end{bmatrix} = \begin{bmatrix} 0 & 1 & 0 & 0 \\ -\omega_f^2 & -2\zeta_f\omega_f & 0 & 0 \\ 0 & 0 & 0 & 1 \\ 0 & 0 & -\omega_f^2 & -2\zeta_f\omega_f \end{bmatrix} \begin{bmatrix} x_{c1} \\ \dot{x}_{c1} \\ x_{c2} \\ \dot{x}_{c2} \end{bmatrix} + \begin{bmatrix} 0 & 0 \\ \omega_f^2 & 0 \\ 0 & 0 \\ 0 & \omega_f^2 \end{bmatrix} \begin{bmatrix} S_x \\ S_y \end{bmatrix} \quad (3.7)$$

$$\begin{bmatrix} \tau_x \\ \tau_y \end{bmatrix} = \begin{bmatrix} \omega_f^2 & 2\zeta_f\omega_f & 0 & 0 \\ 0 & 0 & \omega_f^2 & 2\zeta_f\omega_f \end{bmatrix} \begin{bmatrix} x_{c1} \\ \dot{x}_{c1} \\ x_{c2} \\ \dot{x}_{c2} \end{bmatrix} \tag{3.8}$$

where ω_f is the frequency of the FSM controller, ζ_f is the controller damping ratio, x_{ci} are the controller states, S_x and S_y are the x and y sensor outputs ($S_x = LOS_x$ and $S_y = LOS_y$), and τ_x and τ_y are the control torques.

By design, the FSM controller corrects the LOS jitter. Therefore, the most important trade-off for the FSM control is between the LOS jitter and the sensitivity, which is shown in Figure 3-5. The LOS jitter gradually decreases as the bandwidth increases. At low frequency, the sensitivity increases very slowly. Then, above a bandwidth of about 300 Hz, the sensitivity increases rapidly. Therefore, the desirable range of FSM bandwidth is near 200 Hz where there is significant improvement in the LOS jitter, but the sensitivity penalties are not exceedingly high. However, depending on the desired outcome (high performance or a lot of stability margin), other bandwidths could also be suitable.

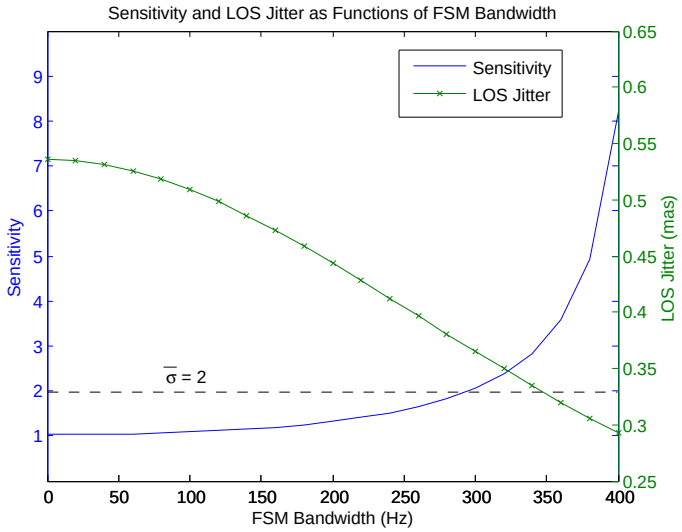

Figure 3-5: Sensitivity and LOS Jitter as Functions of FSM Bandwidth

The FSM control effort is shown in Figure 3-6. As expected, the control effort increases with increasing bandwidth. The effort initially increases rapidly, but as the

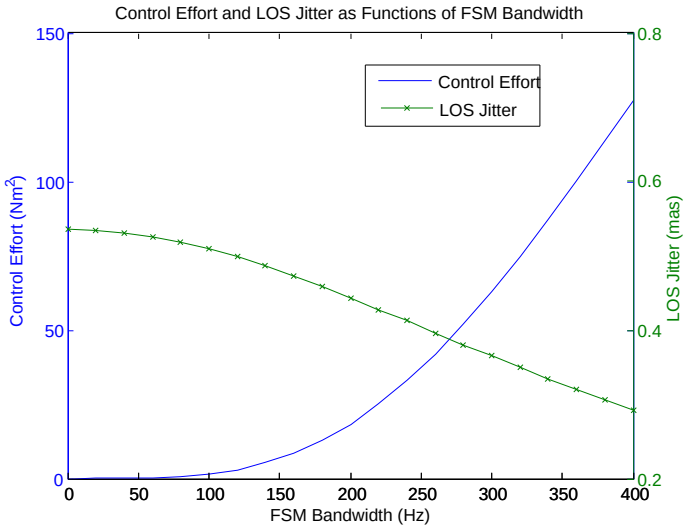

Figure 3-6: FSM Control Effort as a Function of FSM Bandwidth

bandwidth continues to increase, the curve approaches a linear, rather than exponential, increase. This illustrates the additional trade-off between performance and control effort. While the sensitivity curve remains rather flat for a large range of bandwidths, allowing good LOS performance, the control effort is always increasing, and should also be considered when making design decisions.

3.3 Wavefront Control

In preliminary analysis of the telescope, the wavefront error was particularly high and reduction was necessary to meet the requirements. This could be done in multiple ways: by either increasing the areal density of the mirror, or by adding control. The first option is to increase the areal density, thereby increasing the stiffness of the mirror. The WFE is calculated by determining the distortions, or crinkling, of the primary mirror, as was shown in Section 2.6.1. As a result, a stiffer mirror has less vibrations which should result in lower wavefront error. The second option for reducing the WFE is to add control. Since the WFE accounts for the deformations of the surface of the mirror, one way to improve the WFE is to bend the mirror to counteract these unwanted distortions. Wavefront control could theoretically be implemented in any (or all) of the mirrors in the system. In this thesis, only deformation

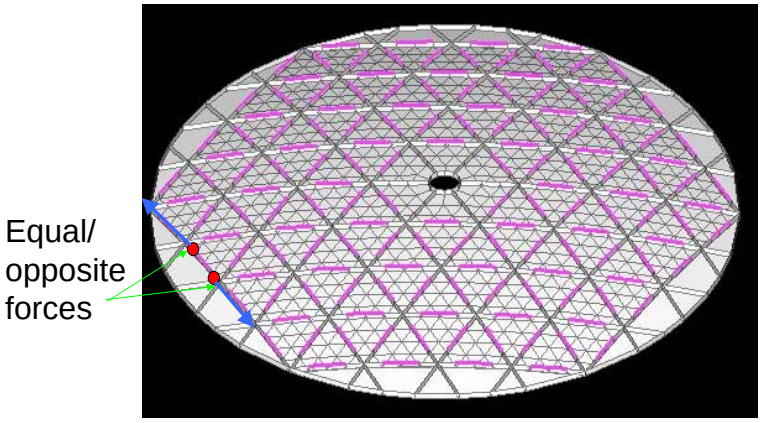

Figure 3-7: Piezo-electric Actuator Implementation. Actuators are red.

corrections of the primary mirror are considered, as it is assumed that it is better to correct the aberrations at the source.

In general, lightweight systems are desired. As will be shown in Chapter 4, higher mass systems yield larger disturbances, in addition to the unwanted launch costs. Increasing areal density of the mirror significantly increases the mass of the system. Therefore, the preferred approach is to add control to decrease the WFE. This will be done using the wavefront control, which will be described in the remainder of this Section.

The actuators for the wavefront controller are surface-parallel, piezo-electric actuators that are embedded in the back of each rib (Figure 3-7). When a voltage is applied, the piezo-electrics expand or contract. This expansion changes the length of the rib and creates a moment on the mirror surface. This can then be used to bend the surface in a desired manner.

The piezos are implemented in the model as bar elements that have representative material properties. Since the linear state-space model will not allow actuation using nonlinear voltage or temperature relations, the piezo actuation is applied using forces. While this is not physically accurate, these forces can be calculated using the material properties of the piezos and the mirror with the appropriate voltage/strain relations to get equivalent forces. Therefore, for the purpose of the model, only the forces are considered, and the voltage relation could be calculated if necessary. The piezo forces

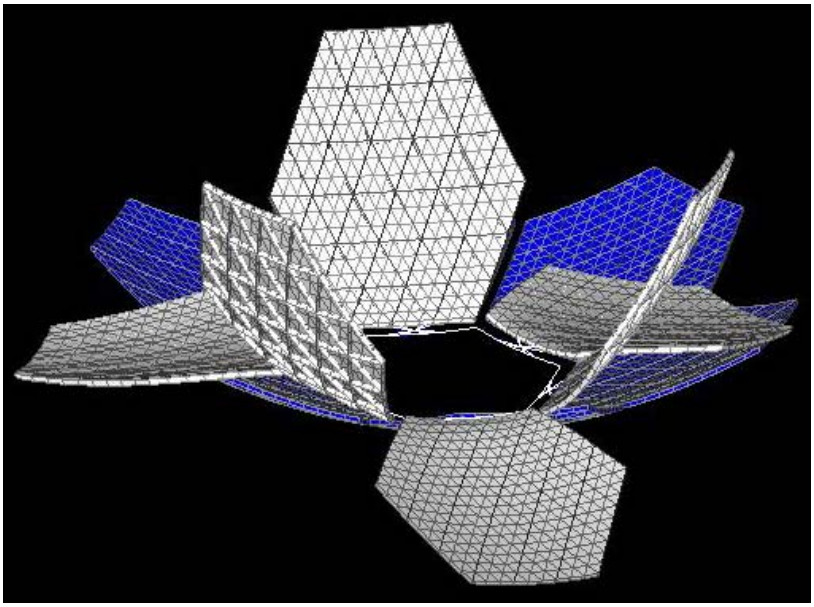

Figure 3-8: Segmented Aperture Petal "Flapping" Mode

are then implemented as an equal and opposite force on either end of the piezo-electric stack, as seen in Figures 3-7 and 2-5.

The sensor for the wavefront controller is slightly different for the monolithic and segmented aperture systems. In the case of a monolithic aperture, the sensor is comprised of the 3^{rd} through 48^{th} Zernikes of the primary mirror. The first two Zernikes, which are tip and tilt, are excluded because the piezos cannot explicitly control those Zernikes. Since the root-sum-square of the first 48 Zernikes is used to calculate the WFE (Section 2.6.1), utilizing the Zernikes as the sensor ensures that the WFE will be directly reduced.

The WFE sensor is slightly modified for the segmented aperture systems. Instead of utilizing the Zernikes of the entire primary mirror, each mirror segment is treated individually. Many of the primary mirror modes of the segmented system involve a petal "flapping" mode as seen in Figure 3-8. Although this flapping is essentially a rigid body mode for each petal, the Zernikes of the overall aperture interpret it as a combination of higher order Zernikes.

For example, if all petals tilt in the same amount in the same direction about the mounting axis, their local Zernike is tilt, but the global primary mirror deformation is

predominately a focus term. A similar example can be seen in Figure 3-9. Pure focus is induced in the entire aperture. The three-dimensional surface of the entire mirror and an individual petal are both seen in Figure 3-9(a). The entire aperture has the actuated "cup" shape. However, the petal appears to be rather flat and merely tilted. A Zernike decomposition of both the local and global surfaces yields the components in Figure 3-9(b). The entire aperture has only a focus term (Zernike 3). However, the Zernike decomposition of the individual petal reveals the that largest component is tilt (Zernike 2), and there are small components of the higher order spherical Zernikes (Zernikes 3, 8, 24).

Since the global Zernikes indicate shape deformations (focus in this case), the piezos attempt to correct for local rigid body tip/tilt motion over which they have no control authority. Therefore, the Zernikes of each individual segment are used for the sensor rather than the Zernikes of the entire aperture. Then, the piezo actuators correct for deformations of the surface of each petal, but not for the rigid body tip/tilt motion of each segment.

Also, since the Zernikes of each petal are used, there is the potential for six times the number of Zernikes to be used in the control sensor than for the monolith aperture system. The higher order Zernikes of the individual petals combine to create much higher order Zernike shapes of the entire aperture than that which is considered in the WFE calculation. Therefore, only the first six Zernikes of each petal are utilized. These few Zernikes from each segment combine to form the necessary higher order Zernikes of the overall aperture that are considered as a part of the WFE calculation.

It was mentioned that the piezo-electric actuators do not have the authority to induce tip and tilt in the primary mirror. It is worth noting that although they cannot actuate pure tip or tilt, they can create shapes that contain components of the tip and tilt Zernikes. As an example, consider a single piezo-electric that is located near the center of a petal and is statically actuated to determine its influence function. The ensuing shape, and its Zernike decomposition, are shown in Figures 3-10 and 3-11, respectively. The mounting constraints in the mirror, along with the assymetric actuation, creates the assymetric shape seen in the figure. The Zernike decomposition

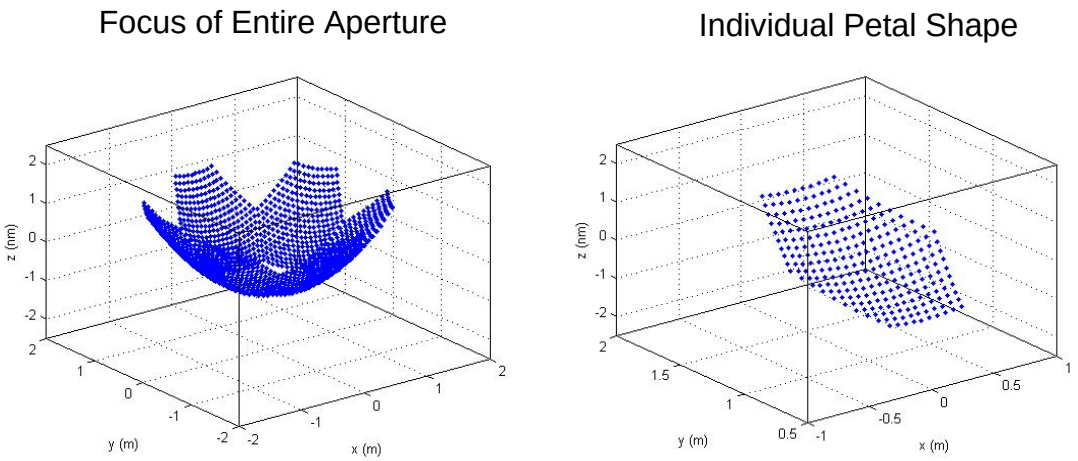

(a) Three-Dimensional Surface of the Aperture and an Individual Petal

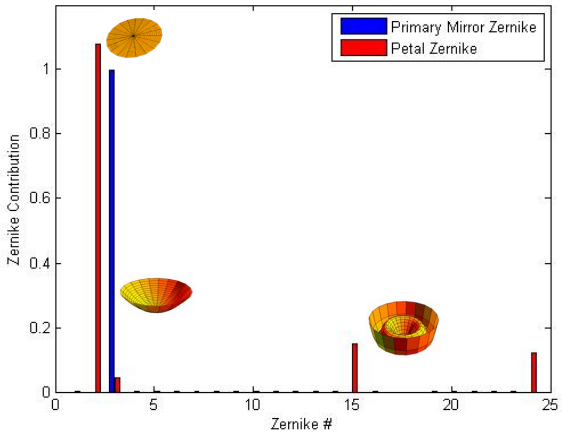

(b) Zernike Decomposition of the Aperture and an Individual Petal

Figure 3-9: Implementation of Pure Focus of a Segmented Aperture

of this shape reveals a large component of tilt. Therefore, the surface-parallel actuator can induce tip and tilt in combination with other Zernike shapes, so a deformed shape that contains a component of tip/tilt can be corrected, even though a pure tip/tilt is uncontrollable.

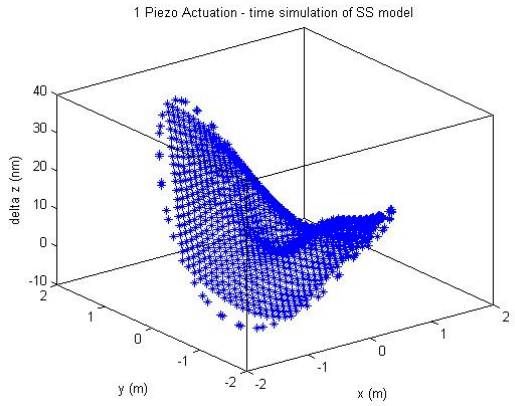

Figure 3-10: Deformed Mirror Shape Due to the Actuation of a Single Piezo-Electric Actuator

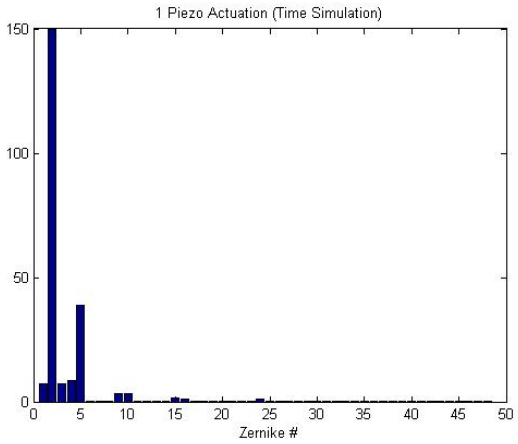

Figure 3-11: Zernike Decomposition for Actuation of a Single Piezo-Electric

3.3.1 Wavefront Controller Implementation

The wavefront controller, in both the monolithic and segmented aperture cases, is implemented as a Linear Quadratic Gaussian (LQG) controller. The LQG method creates a controller of equal order as the plant. The MOST plant is typically between 400 and 450 states. Therefore it is necessary to reduce the size of the plant used to build the controller in order to create a controller of a reasonable size.

In the following description, only the controller inputs and sensor outputs of the state-space system are considered; the other inputs and outputs are temporarily eliminated from the model. In general, the performance outputs and disturbance inputs should also be kept, and only inputs/outputs of the other controllers eliminated. Then, any state that couples either the disturbance or control inputs to either the performance or sensor outputs is maintained.

In the monolithic case, the sensor is almost equal to the performance output. The

sensor is made up of the primary mirror Zernikes, and the performance output is simply the root-sum-square of those Zernikes. Therefore, including both the sensor and performance outputs is redundant. In the segmented aperture case, the sensor is slightly different, and includes the Zernikes of the individual petal segments. When the Zernikes of the overall mirror are added to the system, a similar problem arises as that with the global Zernike sensor; the piezo-electric actuators attempt to correct the global mirror Zernikes, which include the tip/tilt of the segments over which the actuators do not have full control-authority. Therefore, including the performance output in the model creates a larger controller with larger sensitivities and very little performance benefit. Therefore, the performance outputs were not used in the model reduction.

The main source of disturbance in the model is the reaction wheels. Including this in the reduced model should improve performance. However, in this particular case, including the disturbance inputs results in additional states which are largely uncontrollable by the piezo actuators. Therefore, the size of the model increases with very minimal performance improvement. Therefore, the disturbance inputs were not used in the model reduction.

Therefore, the technique that follows should generally be utilized considering the disturbance inputs and the performance outputs in addition to the control inputs and outputs. However, in this case, the performance is not greatly affected by excluding those inputs and outputs. With this system, considering only the wavefront controller inputs and outputs, the process of determining an appropriate reduced-order model can be split into two steps: balancing the model and reducing the model.

Balancing a Model

Balancing a model involves determining transformations that effectively equate the amount a state can be observed and controlled. By balancing the model, the states which have the greatest effects are separated from those that are less influential and could potentially be truncated. This approach is described in References [54, 47, 58, 56].

The controllability and observability grammians (W_c and W_o, respectively) define the degree to which a mode is controllable by an actuator and observable by a sensor. They are determined by solving the appropriate Lyapunov equations:

$$AW_c + W_C A^T + BB^T = 0 \tag{3.9}$$

$$A^T W_o + W_o A + C^T C = 0 \tag{3.10}$$

where A, B, and C are the system state-space matrices.

A state-space representation is not unique, thus transformations can be applied to the system to obtain different controllability and observability grammians that have desirable properties. Ideally, the states are transformed so that the states that are most controllable are also most observable, and thus have the largest effects on the outputs. Then, states which are neither strongly controllable nor strongly observable can be eliminated.

To proceed with the balancing transformations, a transformation matrix, T is assumed to relate $\mathbf{x}$, the original state vector, to $\tilde{\mathbf{x}}$, the transformed state vector.

$$\mathbf{x} = T\tilde{\mathbf{x}} \tag{3.11}$$

The transformation can be substituted into the original state-space equations (Equation 2.6) and combined for simplicity as follows:

$$\begin{aligned} \dot{\mathbf{x}} &= A\mathbf{x} + \begin{bmatrix} B_u & B_w \end{bmatrix} \begin{bmatrix} u \\ w \end{bmatrix} \\ \begin{bmatrix} y \\ z \end{bmatrix} &= \begin{bmatrix} C_y \\ C_z \end{bmatrix} x + \begin{bmatrix} D_{yu} & D_{yw} \\ D_{zu} & 0 \end{bmatrix} \begin{bmatrix} u \\ w \end{bmatrix} \end{aligned} \tag{3.12}$$

These combined matrices can be called A, B, C, and D, the vector of control and noise inputs can be combined into u, and the vector of sensor and performance outputs can

be combined into y for simplicity of notation. These equations can be transformed by substituting $\tilde{\mathbf{x}}$ for $\mathbf{x}$ and algebraically manipulated to obtain the following transformed set of equations:

$$\begin{aligned} \dot{\tilde{x}} &= T^{-1}AT\tilde{x} + T^{-1}Bu \\ y &= CT\tilde{x} + Du \end{aligned} \tag{3.13}$$

The transformed state matrices can then be defined as:

$$\begin{aligned} \tilde{A} &= T^{-1}AT \\ \tilde{B} &= T^{-1}B \\ \tilde{C} &= CT \end{aligned} \tag{3.14}$$

The grammian equations (Equations 3.9 and 3.10) can be written for the transformed system to obtain equations for the transformed grammians, $\tilde{W}_c$ and $\tilde{W}_o$.

$$\begin{aligned} T^{-1}AT\tilde{W}_c + \tilde{W}_cT^TA^TT^{-T} + T^{-1}BB^TT^{-T} &= 0 \\ \tilde{W}_oT^{-1}AT + T^TA^TT^{-T}\tilde{W}_o + T^TC^TCT &= 0 \end{aligned} \tag{3.15}$$

These equations are pre/post multiplied by the transformation matrix as follows:

$$\begin{aligned} T(T^{-1}AT\tilde{W}_c + \tilde{W}_cT^TA^TT^{-T} + T^{-1}BB^TT^{-T})T^T &= 0 \\ T^{-T}(\tilde{W}_oT^{-1}AT + T^TA^TT^{-T}\tilde{W}_o + T^TC^TCT)T^{-1} &= 0 \end{aligned} \tag{3.16}$$

These equations simplify to:

$$\begin{aligned} A(T\tilde{W}_c T^T) + (T\tilde{W}_c T^T)A^T + BB^T &= 0 \\ (T^{-T}\tilde{W}_o T^{-1})A + A^T(T^{-T}\tilde{W}_o T^{-1}) + C^T C &= 0 \end{aligned} \tag{3.17}$$

These equations are of the same form as the original Lyapunov Equations 3.9 and 3.10. Therefore, the transformed grammians can be described in terms of the transformation matrix and the original grammians.

$$\begin{aligned} \tilde{W}_c &= T^{-1} W_c T^{-T} \\ \tilde{W}_o &= T^T W_o T \end{aligned} \tag{3.18}$$

The desired transformation is that which equates the transformed grammians ($\tilde{W}_c = \tilde{W}_o$), thus making the states that are highly observable also highly controllable. Since the two grammians are assumed equal, they can be written as $\Sigma_H = \tilde{W}_c = \tilde{W}_o$. Multiplying the grammians together results in:

$$\Sigma_H^2 = \tilde{W}_c \tilde{W}_o = T^{-1} W_c W_o T \tag{3.19}$$

Equation 3.19 can be rewritten as an eigenvalue problem as follows.

$$W_c W_o = T \Sigma_H^2 T^{-1} \tag{3.20}$$

Here, T is the matrix of eigenvectors and Σ_H^2 is the diagonal matrix of eigenvalues of the product $W_c W_o$, giving a straightforward way to compute the balancing transformation.

Another benefit of this transformation is that the matrix Σ_H is the matrix of Hankel singular values, which can be thought of as describing the energy of the state. Therefore, the transformed system has a Hankel singular value associated with each state. The states with low Hankel singular values can be truncated without losing

important dynamics. The truncation is described in the following section.

Truncating a Model

To begin with model truncation, it is necessary to determine a tolerance for the Hankel singular values (HSVs). Any states with HSVs belows this tolerance have relatively low energies and can then be truncated. Then, Σ_H can be ordered and divided into a block diagonal matrix.

$$\Sigma_H = \begin{bmatrix} \Sigma_1 & 0 \\ 0 & \Sigma_2 \end{bmatrix} \tag{3.21}$$

where Σ_1 contains the higher HSVs that will be kept, while Σ_2 contains the HSVs of the states to be truncated. The state space system can be correspondingly divided.

$$\begin{aligned} \tilde{A} &= \begin{bmatrix} A_{11} & A_{12} \\ A_{21} & A_{22} \end{bmatrix} \\ \tilde{B} &= \begin{bmatrix} B_1 \\ B_2 \end{bmatrix} \\ \tilde{C} &= \begin{bmatrix} C_1 & C_2 \end{bmatrix} \end{aligned} \tag{3.22}$$

It can be proved [58] that the reduced system:

$$\begin{aligned} \dot{x'} &= A_{11}x' + B_1 u \\ y &= C_1 x' + Du \end{aligned} \tag{3.23}$$

is stable, balanced, and contains the highest energy states relating to the actuator control authority and the sensor observability. The HSVs of both a full system and a reduced system can be seen in Figure 3-12.

In addition to the benefits of the smaller model, the balancing transformation also

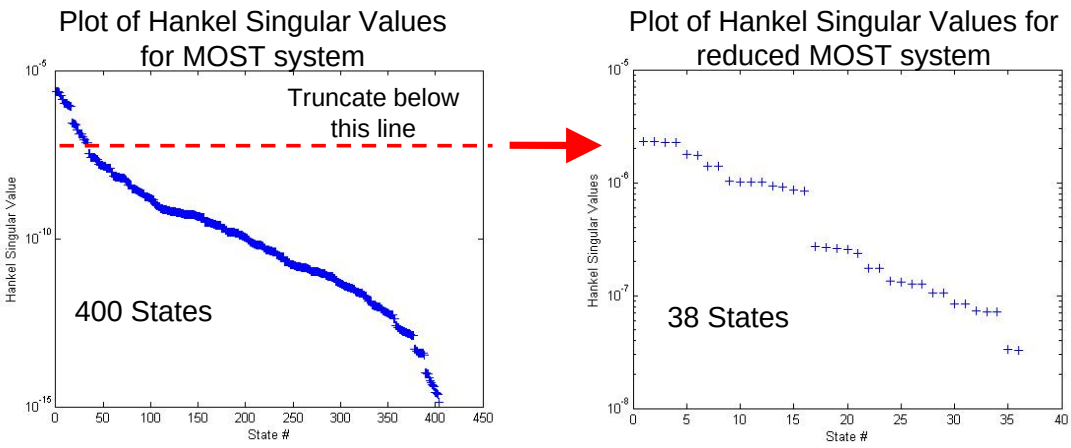

Figure 3-12: Hankel Singular Values of a System Before and After Reduction

improves the condition number of the system. The condition number is defined as the largest singular value divided by the smallest. Low condition numbers are best, and high condition numbers can lead to numerical and computational problems. By truncating out the states with low singular values, the condition number of the system is automatically improved.

At the end of this process, a much smaller, manageable model containing only the most controllable and observable states remains. This model can then be used for the design of an LQG controller.

LQG Controller

As mentioned previously, the controller is a LQG controller. The LQG control combines the optimal Linear Quadratic Regulator (LQR) and optimal Kalman filter. The LQG controller minimizes a cost function J:

$$J = E\left[\frac{1}{2}(z^T R_{zz} z + u^T R_{uu} u)\right] \tag{3.24}$$

where z is the performance output, u is the control input, R_{xx}, R_{uu} are the state and control cost weighting matrices, respectively, and E is the expectation operator. The LQG controller minimizes the expected value of the cost (J) in the presence of uncertain and incomplete measurements. Using the separation principle, LQR

and Kalman filtering can be combined to create an optimal controller [30, 31]. The resulting LQG controller has the following form:

$$\begin{aligned} \dot{x_c} &= A_c x_c + B_c y \\ u &= -C_c x \end{aligned} \tag{3.25}$$

Where x_c are the controller states, y are the sensor inputs, and u are the control outputs. The matrices are defined as:

$$\begin{aligned} A_c &= A - B_u K - L C_y \\ B_c &= L \\ C_c &= K \end{aligned} \tag{3.26}$$

Here, A, B_u, and C_y are from the state space model of the plant for which the controller is being designed. In this case, they are the state space matrices of the reduced model. The K and L matrices are obtained from the solutions to the steady-state control and estimation Ricatti equations:

$$0 = A^T P + PA + C_z^T R_{zz} C_z - P B_u R_{uu} B_u^T P \tag{3.27}$$

$$K = R_{uu}^{-1} B_u^T P \tag{3.28}$$

$$0 = AQ + QA^T + B_w V_{xx} B_w^T - Q C_y^T V_{yy}^{-1} C_y Q \tag{3.29}$$

$$L = Q C_y V_{yy}^{-1} \tag{3.30}$$

To use this controller for the wavefront control problem, the weighting matrices, R_{zz}, R_{uu}, V_{xx}, and V_{yy}, must be chosen appropriately. The state cost matrix is R_{xx}, and is defined as $R_{xx} = C_z^T R_{zz} C_z$. It penalizes the difference between the actual performance output, z, and the desired value of zero.

A rate-damping controller is desired, so only the $\dot{x}$ states are penalized. This involves creating the R_{xx} matrix from the original, unreduced state-space model that is in modal form and has states that are explicitly x and $\dot{x}$ for each mode. The penalty matrix is block diagonal of the form:

$$R_{xx} = \begin{bmatrix} 0 & 0 \\ 0 & I \end{bmatrix} \tag{3.31}$$

where I is the identity matrix. The state vector that is penalized by the R_{xx} matrix is written as:

$$\mathbf{x} = \begin{bmatrix} x \\ \dot{x} \end{bmatrix} \tag{3.32}$$

Therefore, when written as $\mathbf{x}^T R_{xx} \mathbf{x}$, only the velocity states are penalized. Once this matrix is formed, it must be transformed using the balancing and truncation transformations so that it appropriately penalizes the transformed states ($\tilde{\mathbf{x}}$) in the reduced-order model.

The R_{uu} matrix penalizes control effort. If no control penalty is applied, the controller will use an infinite amount of control in an attempt to completely mitigate all state error. It is assumed that all piezo actuators are identical, so they are penalized equally.

$$R_{uu} = \rho I \tag{3.33}$$

Here, the identity matrix penalizes all piezos by a weighting factor, ρ. In the Ricatti solutions, the absolute numbers of the R_{xx} and R_{uu} matrices are insignificant, and only the relative weighting between the two matrices is important. Therefore, the identity matrix can be used in both cases, and the value of ρ specifies the relative difference, which allows the allocation of more or less control.

The V_{xx} and V_{yy} matrices pertain to the estimation portion of the controller. The sensor does not fully determine the state matrices, but full state knowledge is required

for a regulator. Therefore, the state vector must be estimated. Also, it is assumed that the controller is acting in the presence of both process noise and sensor noise. Process noise is due to uncertainty in the state and can be thought of as the error due to incomplete information in determining the state. The uncertainty in the dynamics is considered to be Gaussian white noise with a covariance of V_{xx}. The form of the V_{xx} matrix is assumed to be:

$$V_{xx} = B_{wp} B_{wp}^T \tag{3.34}$$

where B_{wp} is the portion of the B_w matrix penalizing the process noise. In other words, the noise input, w, can be broken into two portions, process noise and sensor noise. Then, the noise vector, w, is written as:

$$w = \begin{bmatrix} w_p \\ v \end{bmatrix} \tag{3.35}$$

where w_p is the process noise and v is the sensor noise. The B_w matrix from the state space equations (Equation 2.6) is then written as:

$$B_w = \begin{bmatrix} B_{wp} & 0 \end{bmatrix} \tag{3.36}$$

Therefore, with this formulation, the V_{xx} matrix penalized the locations where the process noise enters the system.

The V_{yy} matrix represents the sensor noise. The sensor is assumed to be imperfect, with Gaussian white noise of covariance V_{yy}. It is assumed that all of the sensors are equally accurate, thus the form of V_{yy} is:

$$V_{yy} = \rho_e I \tag{3.37}$$

Here, all sensor measurements are equally penalized, and the value of ρ_e is another "knob" for the relative weighting of V_{xx} and V_{yy}. The more the sensor measurements are trusted relative to the dynamics estimate, the smaller ρ_e should be.

This formulation provides a wavefront controller with two variables: ρ and ρ_e. As

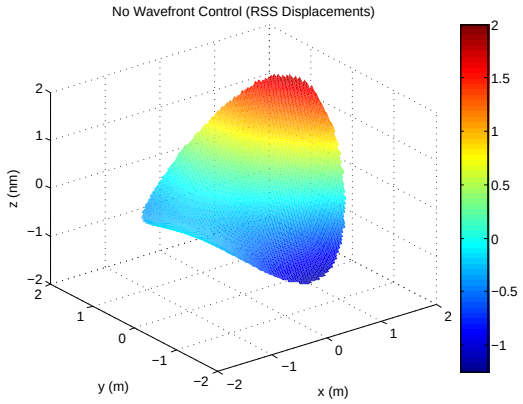

Figure 3-13: Deformations of Mirror Surface Without Wavefront Control

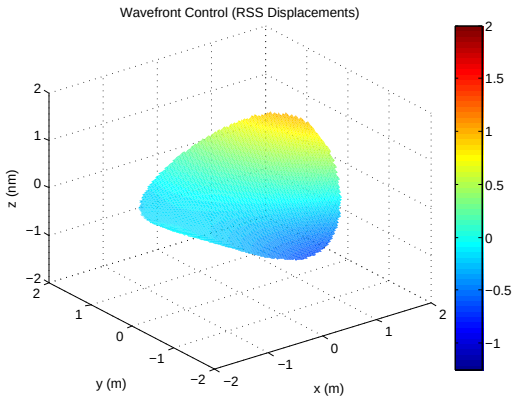

Figure 3-14: Deformations of Mirror Surface With Wavefront Control

ρ becomes smaller, more control is utilized. As ρ_e becomes smaller, the sensors are assumed more accurate and all of the estimation error is contributed to uncertain dynamics.

The Ricatti equations can be solved using MATLAB, and then put into the proper controller form. Then, the controller, which was designed on the reduced order model, is implemented on the full model. An LQG controller has guaranteed stability, however, since the design and implementation systems are different, the stability guarantee is lost.

3.3.2 Wavefront Controller Results

The wavefront controller is obviously aimed at improving the WFE performance. It accomplishes its goal, as seen in Figures 3-13 and 3-14. The left plot shows the z-displacements of the mirror after the disturbance analysis with no wavefront control, and the right plot shows the same system with the wavefront control applied. There is a large visible improvement in the deformation of the mirror, with the maximum peak reduced by 50%.

Since performance gain comes at a cost, it is important to look at both WFE and sensitivity as functions of the control. For simplicity, ρ and ρ_e are assumed to be equal. Then, this single parameter is varied to increase or decrease the amount of control. This assumption has been tested, and, for this controller, has proved to

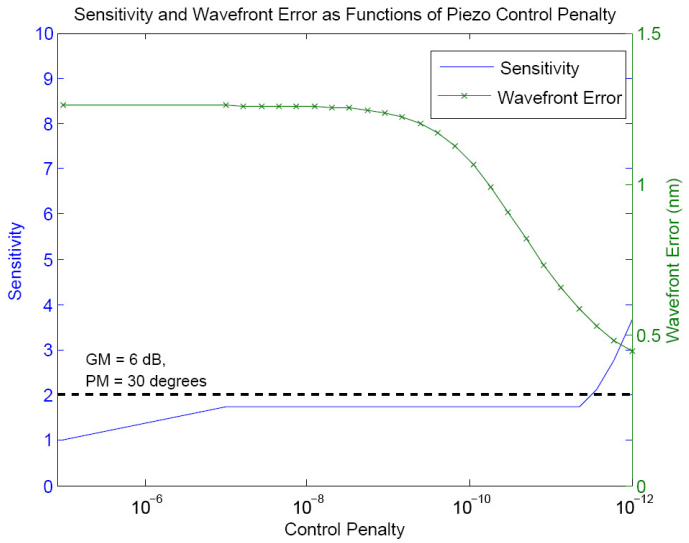

Figure 3-15: Sensitivity and WFE as Functions of Control Cost (ρ)

be a good measure of overall control. There is only a small difference resulting from varying the two parameters separately, so the simplicity of varying only a single input outweighs the very slight performance variation.

The sensitivity and WFE as functions of the control penalty, ρ, can be seen in Figure 3-15. Not shown is the fact that the amount of control increases as the control penalty decreases, from left to right in the plot. The sensitivity rises slightly from including any sort of wavefront control. However, it stays rather constant for a long range of control penalty values. Then, at very low values of control penalty, as the system approaches instability, the sensitivity rises very rapidly. The WFE remains constant for much of the plot, then begins to drop very rapidly. The drop in WFE comes in the range where the sensitivity is still constant, so about a 50% improvement in the WFE can be achieved with only a minimal rise in sensitivity.

The control effort and WFE as functions of wavefront control penalty can be seen in Figure 3-16. The control effort remains quite low for a long range of control penalties, even with significant WFE improvement. However, as the control penalty decreases to less than about 10^{-11}, the control effort becomes extremely large. This occurs at about the same point that the sensitivity begins to rise, indicating that it is a good limit to the amount of control applied.

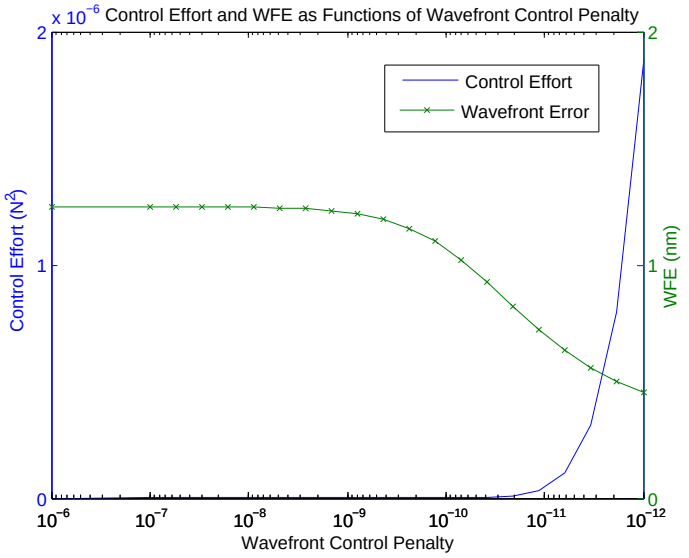

Figure 3-16: Control Effort and WFE as Functions of Control Cost (ρ)

Overall, the wavefront control can significantly decrease the wavefront error of the system by using the piezo actuators to dynamically deform the mirror surface. Significant improvement can be gained without excessive rises in either sensitivity or control effort. The model reduction and controller implementation techniques could be modified for better performance, but the current method functions well for the desired tradespace analyses.

3.4 Petal Control

The wavefront control does not correct for rigid body tip and tilt of the mirror. This is particularly a problem in the segmented aperture systems, which have "flapping" modes that are shown in Figure 3-8. These modes contribute to the wavefront error, and, for the low areal density mirrors, must be controlled to make the segmented system a viable option that meets requirements. Therefore, a petal controller has been implemented for the segmented aperture systems.

The segmented apertures are designed as six hexagonal petals that are cantilevered off of a center ring, which is in turn connected to the rest of the spacecraft. The cantilever connections are utilized in order to save the mass of a back-structure that

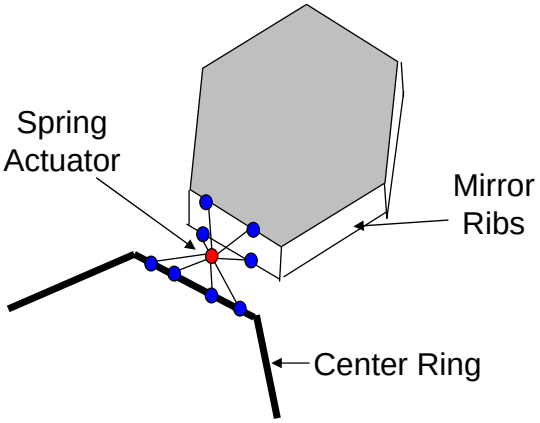

Figure 3-17: Petal Connection to Center Ring

has typically been used in segmented apertures [33, 38]. However, the removal of the back structure necessitates the addition of more control of the petals in order to prevent the flapping modes.

The connections between each petal and the center ring contain petal control actuators. The actuators are torque actuators. They are implemented as springs about the tip direction between two collocated nodes (one connected to the petal and one connected to the center ring), with a rigid element connecting the other degrees of freedom. The nodes on either side of the spring are rigidly connected to their respective components. These connections must include multiple connection points to avoid a point load at a single node. A schematic of the connection can be seen in Figure 3-17. The center "spring actuator" point represents the two collocated nodes where the two sections are connected with the spring. The other eight dots represent the points where the actuator assembly connects to the center ring and mirror segment. With this implementation, an equal and opposite torque can be applied on either side of the spring (both located at the center point) to actuate the petal as desired.

The sensor is a differential measurement of the z-translations of two points on a radial line on the petal (Figure 3-18). This measurement is made relative to the actuator so that the petal remains at a constant angle with respect to the spacecraft, not inertial space. This gives an approximation to a rigid body tip sensor for the

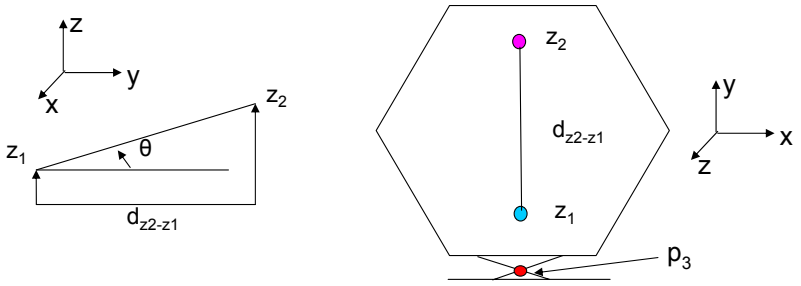

Figure 3-18: Rigid Body Tip Sensor for Each Petal Segment

petal using a small angle approximation as:

$$\theta_{sens} = \frac{z_2 - z_1}{d_{z_2 - z_1}} - \theta_{3_x} \tag{3.38}$$

The relevant points can all be seen in Figure 3-18. Here, z_1 and z_2 are the vertical translations of the two points, $d_{z_2-z_1}$ is the distance between points 1 and 2, and θ_{3_x} is the rotation of the point of the actuator on the side of the center ring (p_3).

All of the petals have the same layout, with a local coordinate system that is rotated in a circle so that the axes appear the same on each petal. Therefore, the problem statement for each petal sensor and actuator pair looks identical to Figure 3-18.

The controller is a positive position feedback (PPF) controller [18]. The stiff joint does not give enough control authority for a typical PD controller. Therefore, a positive position feedback is utilized with negative rate feedback. The positive position feedback de-stiffens the joint, while the negative rate feedback improves the performance and maintains stability. The controller is similar to the PD controller described for the FSM (Section 3.2) in all respects other than the positive value for K_p rather than the typical negative value.

Again, the bandwidth is the primary means for dictating the amount of control applied. The bandwidth ranges anywhere from 0 to about 50 Hz. Very good results can be obtained without sacrificing a lot of stability margin. Figure 3-19 shows the sensitivity and WFE as functions of the petal controller bandwidth.

As visible in the plot, the wavefront error decreases about 20% before the sen-

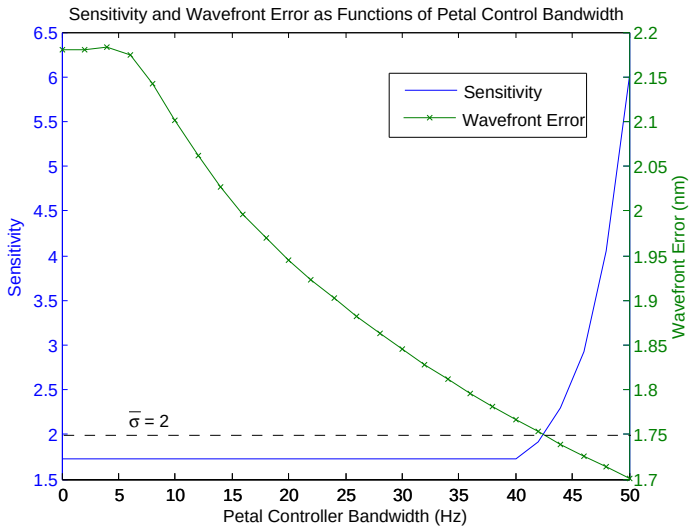

Figure 3-19: Sensitivity and Wavefront Error as Functions of Petal Controller Bandwidth

sitivity increases discernably. Then, around a bandwidth of 40 Hz, the sensitivity shoots upwards, and at approximately 53 Hz, the system becomes unstable. These exact values depend on the system considered, but overall, a significant improvement in WFE performance can be realized with only a small increase in sensitivity.

The control effort and WFE resulting from increasing bandwidth are shown in Figure 3-20. As seen previously, the WFE decreases with increasing bandwidth. Also, as expected, the control effort increases with increasing bandwidth. However, this increase is exponential, thus, there is a definite balance to be made between the performance improvement and power consumption.

Overall, the petal control significantly improves the WFE of the segmented aperture systems. However, it does so at the expense of sensitivity and control effort. Even so, the benefits gained from the improved performance of the segmented systems can outweigh these costs.

3.5 Summary

The four controllers implemented in conjunction with the MOST system all serve to improve the performance in a particular way. Each controller has a particular

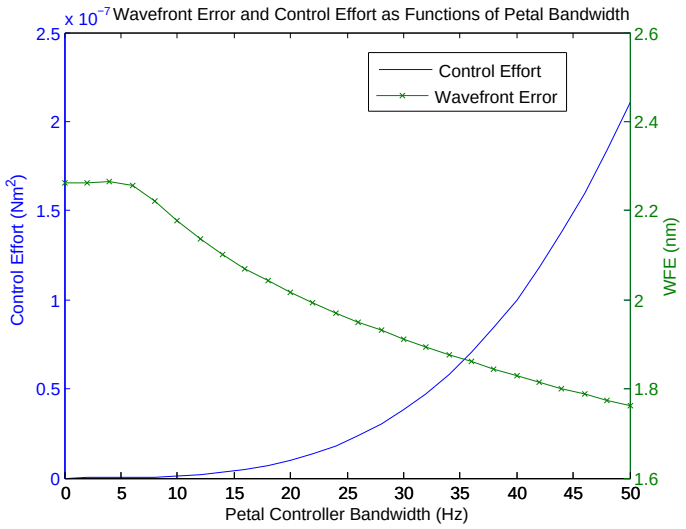

Figure 3-20: Petal Control Effort and WFE as Functions of Petal Controller Bandwidth

performance metric for which it attempts to enhance the performance: ACS mainly improves settle time, FSM improves LOS jitter, and the wavefront controller and petal controller improve WFE. For each of these particular tasks, each controller performs well. However, each of these control systems also affects other performance metrics; they affect the stability margin and control effort. They can also unintentionally affect the other optical performance metrics, which can provide either good or bad performance changes. Also, the interactions that arise when the controllers combine can be complicated and unintuitive. Therefore, it is important to examine these controller not only alone, as was done in this chapter, but also in conjunction with one another as is discussed in Chapter 5.

Chapter 4

Slew and Settle Analysis

Effective space telescopes must quickly slew to point at different locations. This slewing allows for more productive imaging, but also induces jitter in the system and decreases the amount of time that can be utilized for operations. The system must be out of operations during the time that the system is performing the slew, and until the vibrations resulting from the slew attenuate. Thus, the sum of time that it takes to complete the slew and settle from the vibrations measures the amount of time that the system is out of operations. Therefore, it is included as a system performance metric (Section 2.6.3).

The slewing maneuvers are actuated with the reaction wheel assembly (RWA) located in the center of the bus. The RWA also generates the disturbances used for the dynamic disturbance analysis (Section 2.5). The size of the RWA impacts the magnitude of the disturbance imparted on the system, and the RWA is sized to accommodate the desired slewing maneuver. Therefore, even though faster slews can decrease the system slew and settle time, they also require larger reaction wheels, and thus cause more disturbance. The settle time also depends highly on the temporal profile of the torque command, and on the way in which the required torque is distributed amongst the reaction wheels. The slewing methodology, various torque profiles, and their resulting vibrations will be discussed in the following section.

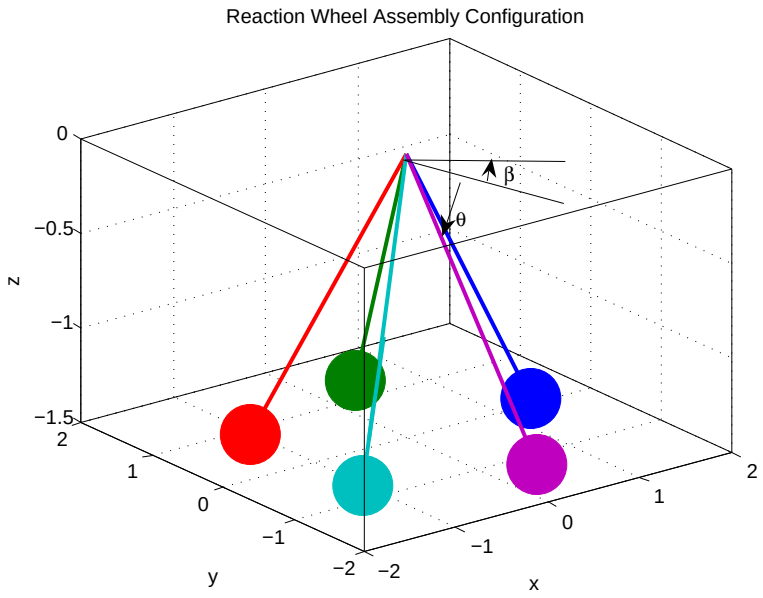

Figure 4-1: Pyramidal Reaction Wheel Configuration

4.1 Methodology

The slew and settle analysis can be broken into two tasks. The first involves creating the desired torque profile, distributing the torque amongst the different reaction wheels, and sizing the reaction wheels. The second step is the actual slewing simulation to determine the overall slew and settle time. Both tasks are described in the following sections.

4.1.1 Reaction Wheel Sizing and Torque Distribution

The reaction wheel assembly consists of five individual reaction wheels. These wheels are at variable angles to each other, but the most commonly utilized configuration is pyramidal, with all reaction wheels at equal angles below the $x-y$ plane (θ) and spaced evenly around the $x-y$ plane (spaced with angle β) as seen in Figure 4-1. The reaction wheel spin axis is along the lines pointing toward the common point as seen in the figure.

A system torque profile is generated for the slewing maneuvers (Section 4.2). This torque must then be partitioned amongst the five reaction wheels, but there

are an infinite number of ways the necessary torque could be divided. Therefore, a division scheme that minimizes the wheel speeds, and consequently minimizes the angular momentum and torque that each wheel must provide, is utilized [6]. The minimization is performed as follows:

$$min \sum_{i=1}^{5} \omega_i^2 \tag{4.1}$$

subject to the constraint:

$$\begin{bmatrix} H_x \\ H_y \\ H_z \end{bmatrix} = A \cdot \begin{bmatrix} H_{w_1} \\ H_{w_2} \\ H_{w_3} \\ H_{w_4} \\ H_{w_5} \end{bmatrix} \tag{4.2}$$

where ω_i is the angular velocity of wheel i, H_x, H_y, and H_z are the components of angular momentums of the reaction wheel assembly in global coordinates, H_{w_i} is the angular momentum of wheel i along its spin axis, and A is a matrix relating the wheel orientation to the spacecraft axes. The A matrix is calculated using the Euler angles of each reaction wheel in the configuration shown in Figure 4-1. The minimization can be solved using Lagrange multipliers to obtain the solution:

$$\begin{bmatrix} H_{w_1} \\ H_{w_2} \\ H_{w_3} \\ H_{w_4} \\ H_{w_5} \end{bmatrix} = A^T (A A^T)^{-1} \begin{bmatrix} H_x \\ H_y \\ H_z \end{bmatrix} \tag{4.3}$$

The torque that each wheel must provide can be obtained from the angular momentum as a function of time using:

$$T_{w_i} = \frac{\Delta H_{w_i}}{\Delta t} \tag{4.4}$$

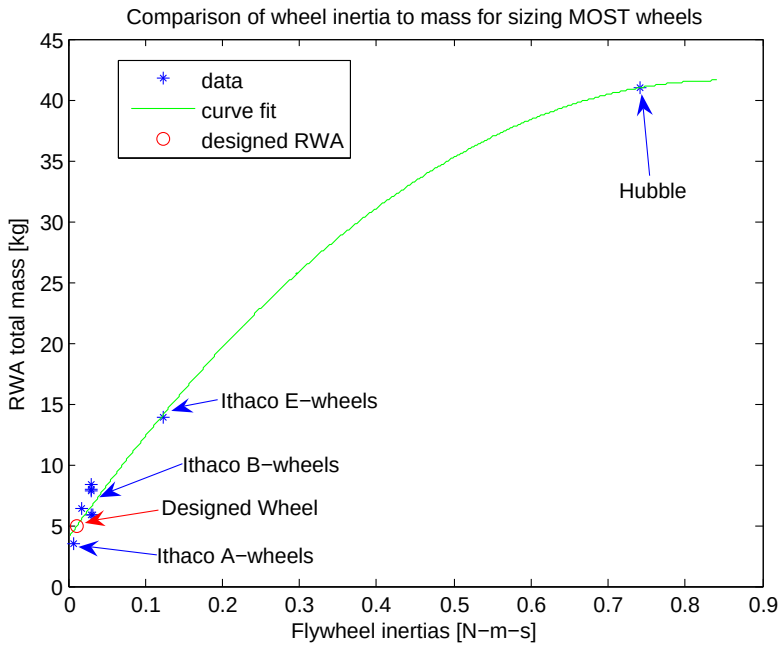

Figure 4-2: Comparison of Wheel Inertia to Mass for Sizing the MOST Reaction Wheels

Here, T_{w_i} is the torque provided by the wheel at that time step, ΔH_{w_i} is the difference in momentum at either end of the time step, and Δt is the length of the time step. In this way, the torque provided by each wheel as a function of time can be constructed.

It is assumed that all reaction wheels are identical, so the maximum torque that must be provided by any wheel at any time is used to size the inertia of the wheel. The wheel is sized based on the angular momentum storage required at the maximum torque, while not exceeding the maximum allowable speed of the wheel (4000 rotations per minute). Additionally, the minimum wheel inertia is multiplied by a safety factor of two.

The wheel inertia is used in conjunction with a curve fit of existing reaction wheels inertias and masses [40], and the wheel mass is calculated from the curve as seen in Figure 4-2. The curve-fit inertias are used to determine the reaction wheel mass and the amplitudes of the harmonics that are used to create the disturbance model [40]. This methodology, along with the slewing torque profiles (Section 4.2), can then be used to size the reaction wheels, determine the torques, and determine the disturbance harmonics used in slew and settle analysis.

4.1.2 Slewing Simulation

The actual slew and settle analysis is a time domain simulation of the slew of the MOST integrated model. The input command is the desired torque profile summed with the disturbances. The disturbances are given by [40]:

$$m(t) = \sum_{i=1}^{n} C_i \cdot \omega^2 \cdot sin(2\pi h_i \omega t + \alpha_i) \tag{4.5}$$

Here, $m(t)$ is the disturbance force or torque in N or N-m, n is the number of the harmonic, C_i is the amplitude of the i^{th} harmonic, ω is the wheel speed in hertz, h_i is the harmonic number, and α_i is a random phase that is uniform over the interval [0, 2π]. The random phase is necessary to account for the non-deterministic nature of the disturbance. The disturbances due to each reaction wheel are calculated using Equation 4.5, and transformed to the global spacecraft axes. The disturbances and torque commands are input into a linear time-domain simulation of the state-space model to obtain the line-of-sight jitter as a function of time. The system has settled when the LOS jitter remains below the threshold value, as seen in Figure 4-3. This threshold is the LOS jitter requirement derived in Section 2.6.1. The simulation gives a quantitative result for the amount of time that a system is out of operations due to a slewing maneuver. The slew and settle time can then be optimized by changing various parameters as discussed in the remainder of this chapter.

4.2 Torque Profiles

As previously indicated, the temporal torque profile utilized for the slew can affect the slew and settle time and the size of the wheels. A number of profiles are examined: bang-bang, sinusoidal, and a zero initial condition profile. Additionally, a feed forward technique is discussed in Section 4.3.

The bang-bang profile is the minimum time solution for the slew. The torque is a positive constant for the first half of the slew, then instantaneously switches to the same negative constant at the midpoint of the slew to bring the system to the desired

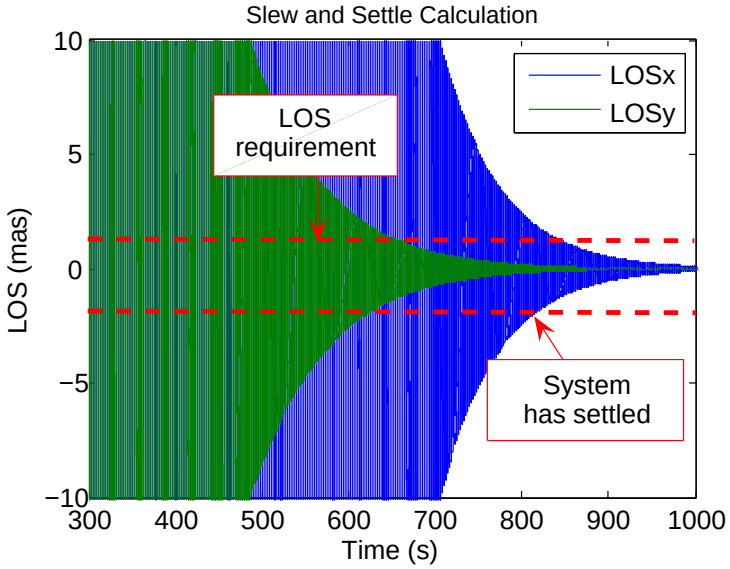

Figure 4-3: LOS Time Domain Slew and Settle Simulation, Slew completed at 300 seconds

rest state at the end of the maneuver. The profile can be seen in Figure 4-4(a). Although this is the the minimum time solution for a given maximum torque (or a minimum torque solution for a given slew time), there is a discontinuity in the angular position at the start, middle, and end of the slew, which causes residual vibrations.

The second slewing profile is a one-period sinusoidal input as seen in Figure 4-4(b). The sinusoid eliminates the discontinuity in angular position at the endpoints, but still contains a discontinuity in the angular velocity. Also, the maximum torque for a given slew time is greater than in the bang-bang case, resulting in slightly larger reaction wheels and disturbances.

The third slew profile is a zero initial condition profile, with both the angular position and angular velocity being continuous at the two endpoints (Figure 4-4(c)). The shape is constructed by dividing the slew time into thirds. The first third of the profile is a cosine curve with an amplitude of $\frac{T_{max}}{2}$, a period of $\frac{4}{3} \cdot t_{slew}$, shifted up by $\frac{T_{max}}{2}$, and shifted right from the $t = 0$ point by π radians. Here, T_{max} is the maximum torque in the profile, determined using the slew time, and t_{slew} is the slew time. The middle third of the profile is a cosine curve with an amplitude of T_{max},

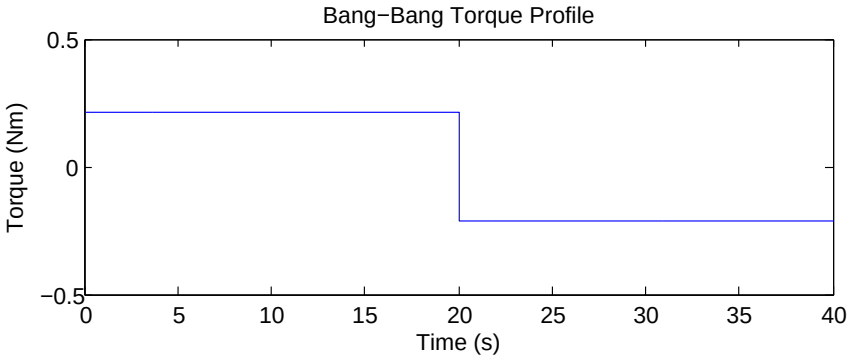

(a) Bang-Bang Torque Profile

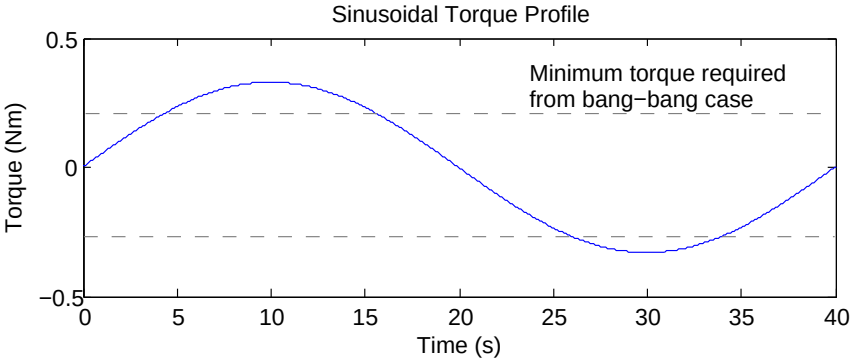

(b) Sinusoidal Torque Profile

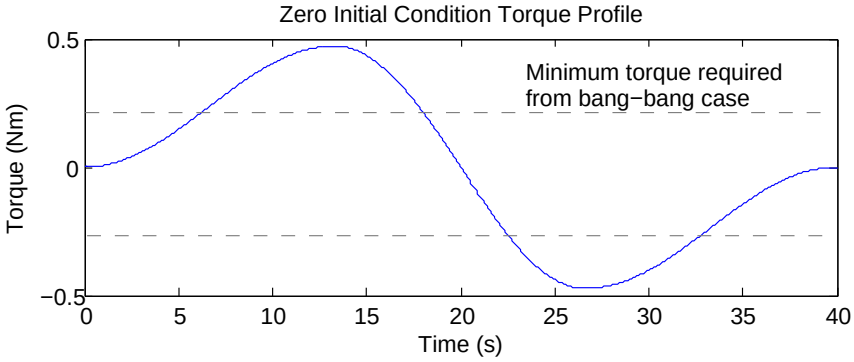

(c) Zero Initial Condition Torque Profile

Figure 4-4: Three different torque profiles as functions of time.

a period of $\frac{2}{3} \cdot t_{slew}$, and shifted right from the $t = 0$ point by π radians. The final third of the profile is a cosine curve with the same amplitude and period as the first third, but shifted down by $\frac{T_{max}}{2}$. The three sections combine to give a smooth profile that has continuous angular position and velocity at the start and end of the profile, eliminating the jump discontinuities. However, it still contains an impulse in the jerk (the third derivative of θ). This profile results in a larger torque for a given slew time than either of the previous two profiles. However, as will be shown in Section 4.4, the elimination of impulses in angular position and velocity mitigates more jitter than the extra disturbances create, making it a viable option.

4.3 Feed Forward Techniques

A final technique considered for creating torque profiles is a feed-forward technique known as time optimal command input shaping. This technique combines Pontryagin's Minimum Principle with input shaping commands [46] in a generalized way to be applied to linear systems. The goal is to move a linear system from a rest state to a desired state in the minimum amount of time while minimizing residual vibrations. The technique involves a nonlinear constrained optimization to develop an optimal series of commands. The technique is fully described in Tuttle [50], but the key steps, as they relate to the MOST system, will be repeated here.

The fundamental idea in time-optimal input shaping is to use a series of "bangs" at specified times to implement a fast motion while also reducing vibrations. A sample of a typical profile can be seen in Figure 4-5. The time optimal profile can be written as follows:

$$u(t) = \sum_{j=0}^{n} a_j \cdot 1(t - t_j) + \sum_{j=1}^{r} c_j \cdot e^{z_j(t-t_n)} \cdot 1(t - t_n) \tag{4.6}$$

where a_j are the amplitudes of the pulses, c_j are the coefficients of the exponents, z_j are the system zeros, n is the number of switches, r is the number of zeros, t_j are the switch times, and $1()$ is the unit step function. The amplitudes of the pulses are

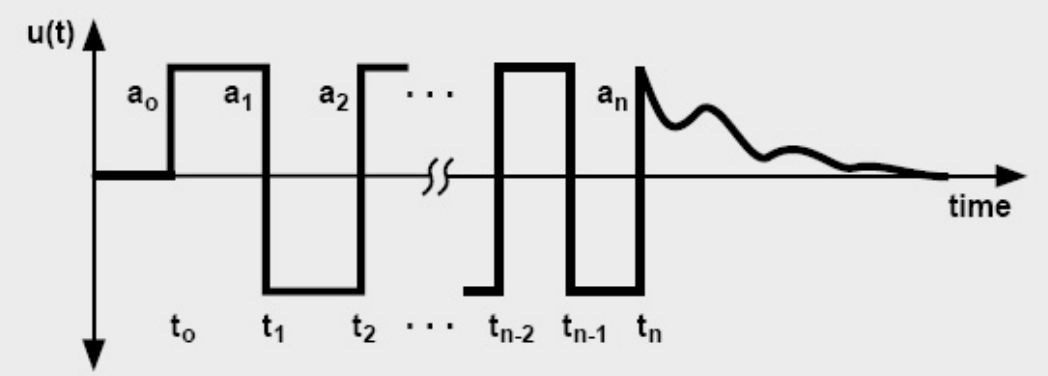

Figure 4-5: Typical Time Optimal Command Input Shaping Profile

known from the maximum value of the actuators (for minimum time). In MOST, the time is specified and the minimum torque is desired. Therefore, relations are derived to obtain the maximum torque (the amplitudes or the pulses) required to achieve a given slew time in order to fit within this framework.

The switch times are calculated using a minimization of the total slew time in the presence of three constraints: a dynamic cancellation constraint, a boundary condition constraint, and an actuator limit constraint. The essence of the dynamic cancellation constraint is that the control input must have zero net excitation at the system poles of interest [7]. The boundary condition constraint involves the two boundary conditions: first that the system starts from rest at $t = 0$, and second, that the system must move by the specified amount ($d\theta$) and end with a specified angular velocity (0). The actuator limit constraint puts a limit on the amount of control input the actuator may use. In time optimal problems, the actuators are always saturated to achieve the minimum time. Thus, without a limit on actuator authority, the optimization will use infinite control input.

In implementing the optimization on the MOST system, a simplification is made to consider only the system poles. The zeros significantly complicate the constraints, and add the tail to the command input profile, thus making the optimization more computationally expensive. The denominator dynamics give enough information to make effective use of this technique without the added complications involved with using the system zeros. With this assumption, the constraints and optimization are

implemented in the following way [50]. First, the command is restated as:

$$u(t) = \sum_{j=0}^{n} a_j \cdot 1(t - t_j) \tag{4.7}$$

The Laplace transform can be taken to obtain:

$$U(s) = \frac{1}{s} \sum_{j=0}^{n} a_j e^{-stj} \tag{4.8}$$

where $u(t)$ and $U(s)$ are the time domain and Laplace domain input respectively, t is time, and s is the Laplace variable. The dynamics cancellation constraint can be written as:

$$\left[\sum_{j=0}^{n} a_j e^{-stj} \right]_{s=p_i} = 0 \tag{4.9}$$

where p_i is the i^{th} pole. This can be expressed in matrix notation for easy MATLAB implementation as:

$$exp(-s\mathbf{t}) \cdot \mathbf{a} = \mathbf{0} \tag{4.10}$$

where $\mathbf{t}$ and $\mathbf{a}$ are the matrices containing the switch times and the amplitudes, respectively, *exp* is the element by element exponential, and s are the relevant complex poles. In this implementation, it is important to set both the real and imaginary parts of Equation 4.10 equal to zero.

The boundary constraint can be implemented as follows:

$$\begin{aligned} t_0 &= 0 \\ \theta(0) &= 0 \\ \dot{\theta}(0) &= 0 \\ \theta(t_n) &= \theta_f \\ \dot{\theta}(t_n) &= 0 \end{aligned} \tag{4.11}$$

where t_0 is the start time, $\theta(t_n)$ is the angle at the final time, θ_f is the desired final angle, and $\dot{\theta}(t_n)$ is the angular velocity at the final time. The angle and angular velocity at t_n can be found by integrating:

$$T = I \cdot \ddot{\theta} \tag{4.12}$$

where T is the torque, I is the inertia, and θ is the angular distance. This is valid if the slewing maneuver is considered to be a rigid body rotation.

The final condition is the actuator limit constraint. Since the goal is to size the actuators, and not necessarily limit the maximum torque to a specific value, this condition must be modified. A slew maneuver of a certain profile completed in a given amount of time requires a certain value of maximum torque. It is necessary to determine this maximum torque for the input shaping case. Therefore, a number of designs are used to determine a relation between the amount of maximum torque in the bang-bang case compared to the input shaping case. This relation is used to determine the maximum torque to use for the input shaping optimization to achieve a slew of a desired length of time. (The maximum torque increases $\sim 25\%$ from the bang-bang case.) With this relation, the slew time is near the desired value, but depends on the optimization. Therefore, unlike in the previous profiles, the exact length of time cannot be explicitly chosen, but can be very close to the desired time. Then, this maximum torque (T_{max}) can be used to constrain the applied input through the $\mathbf{a}$ matrix in Equation 4.10. For the case of slewing to a desired angle with a specified final angular position and zero final angular velocity, the matrix is:

$$\mathbf{a} = T_{max} \cdot [\ 1 \quad -2 \quad 2 \quad -2 \quad 2 \quad -2 \quad 1\ ]^T \tag{4.13}$$

The values in the matrix correspond to the change in torque at that switch. Therefore, the first switch causes the command to increase to T_{max}, the second causes it to decrease to $-T_{max}$ and so on. This also specifies that there will be at most seven switches, including the initial and final switch. The optimization then calculates the seven times where these switches occur to minimize the total time, while still satisfying

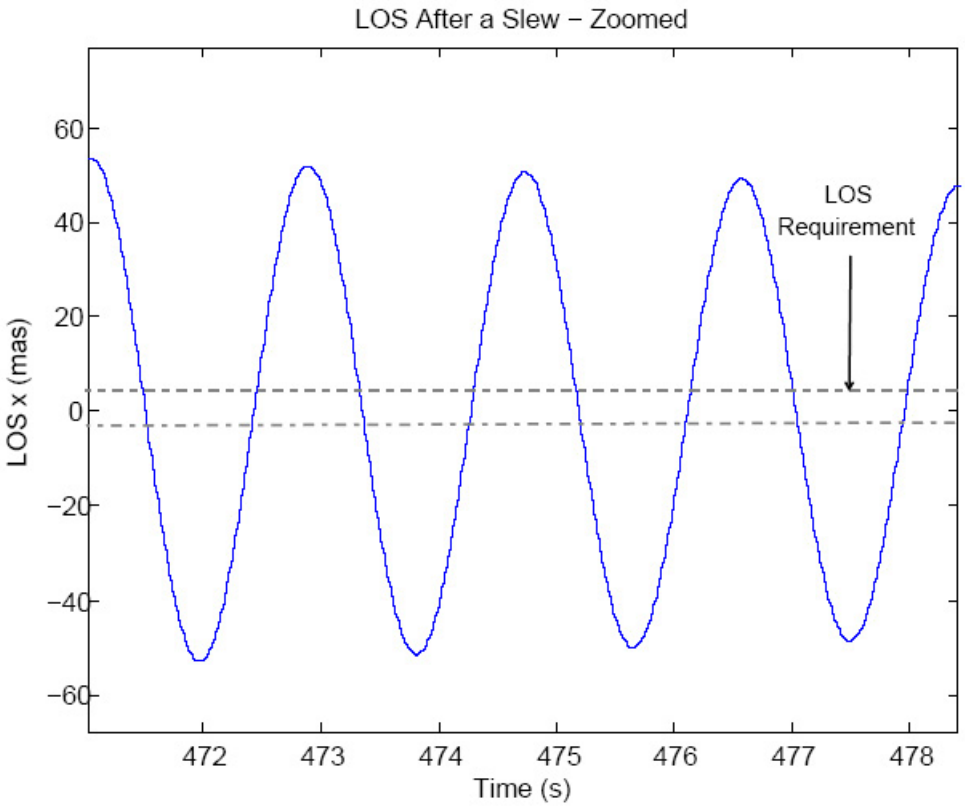

Figure 4-6: LOS Jitter after a Slew with 0.5 Hz Mode Visible

all of constraints. Although seven switch times are specified, the optimization can utilize fewer switches by setting two adjacent switch times equal to each other, thus effectively eliminating that switch.

The implementation of this method on MOST also requires a selection of poles to be included in the formulation. The 400 poles in the system would require far too many switches and computation time. Instead, only the first solar panel mode is considered and minimized. Figure 4-6 shows a close-up of the LOS jitter following the slew (Figure 4-3) for a bang-bang torque profile. The prominent vibration is the solar panel mode that is visible at about 0.5 hertz, indicating that it is the most important vibration to suppress after the slew.

Using the simplified method of only penalizing the first solar panel mode, considering the denominator dynamics, and allowing seven switches results in a simpler optimization that is implemented in MATLAB and can be automated to fit inside of

the MOST framework. A sample of a typical torque profile generated by this method can be seen in Figure 4-7.

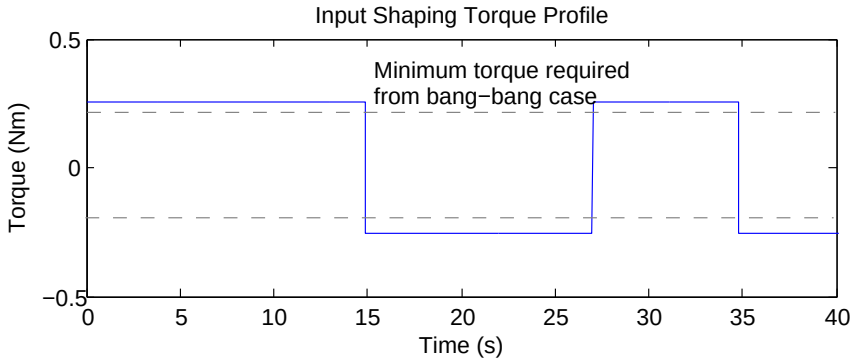

Figure 4-7: Command Input Shaping Torque Profile

4.4 Results

The framework for the slew and settle time analysis has been laid in the previous sections. The analysis ultimately consists of the following steps:

1. Determine the desired slewing maneuver
2. Determine and generate the desired torque profile
3. Divide the system torque between the reaction wheels
4. Determine the reaction wheel size and disturbance harmonics
5. Perform a time-domain simulation of the slewing maneuver, including disturbances
6. Compare resulting slew and settle times

These steps provide the basis for all of the analyses, which will be broken into three sections: analysis of different torque profiles, balance of slew and settle time, and influence of other parameters such as ACS control bandwidth and system damping.

4.4.1 Torque Profile Analysis

Four different torque profiles were discussed in Sections 4.2 and 4.3. Each of these torque profiles has advantages and disadvantages. For the first three profiles (bang-bang, sinusoidal, and zero initial conditions), as discontinuities are eliminated, the profile becomes smoother, but the maximum torque is higher. The input shaping profile is much more complex than the other three. The best way to analyze the difference is to examine the residual vibrations, shown with the LOS jitter, after the slew (Figure 4-8). Figure 4-8(a) shows the four torque profiles, and Figure 4-8(b) shows the vibrations resulting from each slew. Each profile in Figure 4-8(a) has the resulting vibration seen immediately to its right in Figure 4-8(b). This particular set of slews are all twenty seconds long, and are arbitrarily performed between time $t = 220$ s and $t = 240$ s.

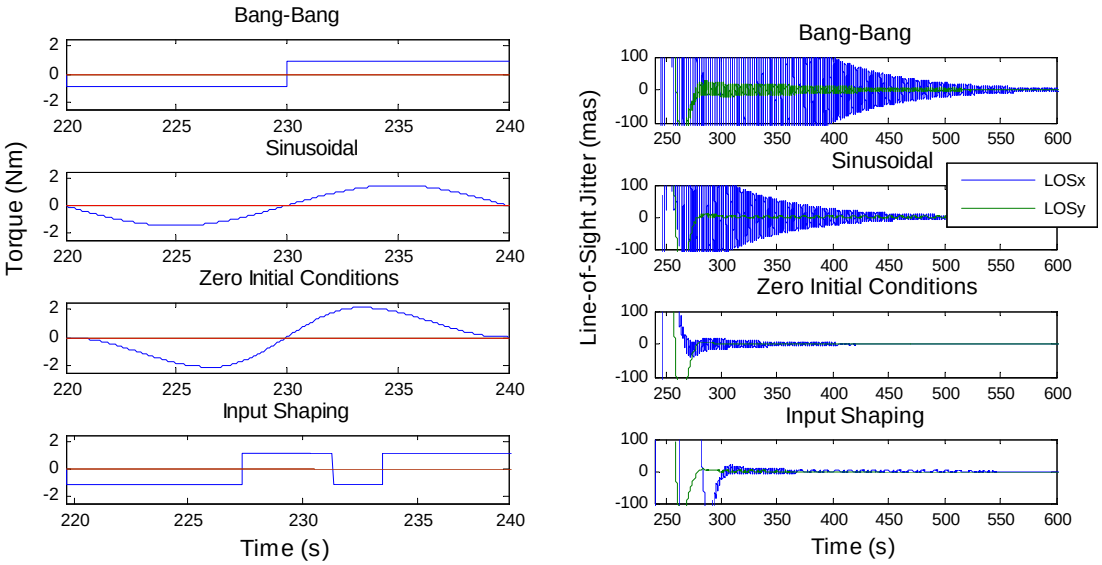

(a) Torque Profiles

(b) Resulting LOS Vibration

Figure 4-8: Torque Profiles and Corresponding LOS Jitter after the Slew

It is apparent that, although there are fewer disturbances due to the smaller reaction wheels in the bang-bang case, the discontinuities of the slew profile causes far more vibration. The bang-bang slewing profile has the worst residual vibration of any of the cases. The sinusoidal profile has significantly less vibration than the bang-

bang case, but improvements can still be made. The zero initial condition case and the input shaping case have very similar settle times. The input shaping case has some very large vibrations immediately following the slew, but they quickly settle. The zero initial condition case has smaller vibrations just after the slew, but they do not die down as quickly. This profile also requires larger reaction wheels than the input shaping case. Therefore, either of these two techniques provide favorable slew and settle performance and could be utilized for the MOST project. The MOST model allows the user a choice between any of these options, but in most cases, the zero initial condition case is used. This profile is used most often because the performance is similar to that of the input shaping case, but it does not involve optimizations, which can get stuck in local minima and not actually converge to the optimal solution. This allows the automated tradespace exploration be more computationally robust.

4.4.2 Balance of Slew Time and Settle Time

In addition to changing the torque profile, the slew time may be changed to minimize the settle time. Generally, longer slews have shorter settle times, so they may be better than fast slews. In all cases, the angular change of the telescope is five degrees. A plot of the total slew and settle time as a function of the slew time, for each of the four different torque profiles, can be seen in Figure 4-9.

The goal is to minimize the total slew and settle time, which represents the entire time the system is out of operation due to the slewing maneuver. The zero initial condition and input shaping torque profiles both give good results, with the input shaping providing the minimum "out-of-operations" time of 63 seconds at a slew time of 27 seconds for this particular system. The bang-bang case oscillates as a function of slew time, and is not a smooth curve like the others. Lengthening the slew time increases the time-lag between the three impulses in the bang-bang case. For some time-lags, the impulses constructively excite certain modes, while other time lags may cause later impulses to cancel vibrations that were excited by earlier impulses. The other three curves are relatively smooth, with the exception of a few bumps resulting from excited modes. An important thing to note is that in all of the smooth curves,

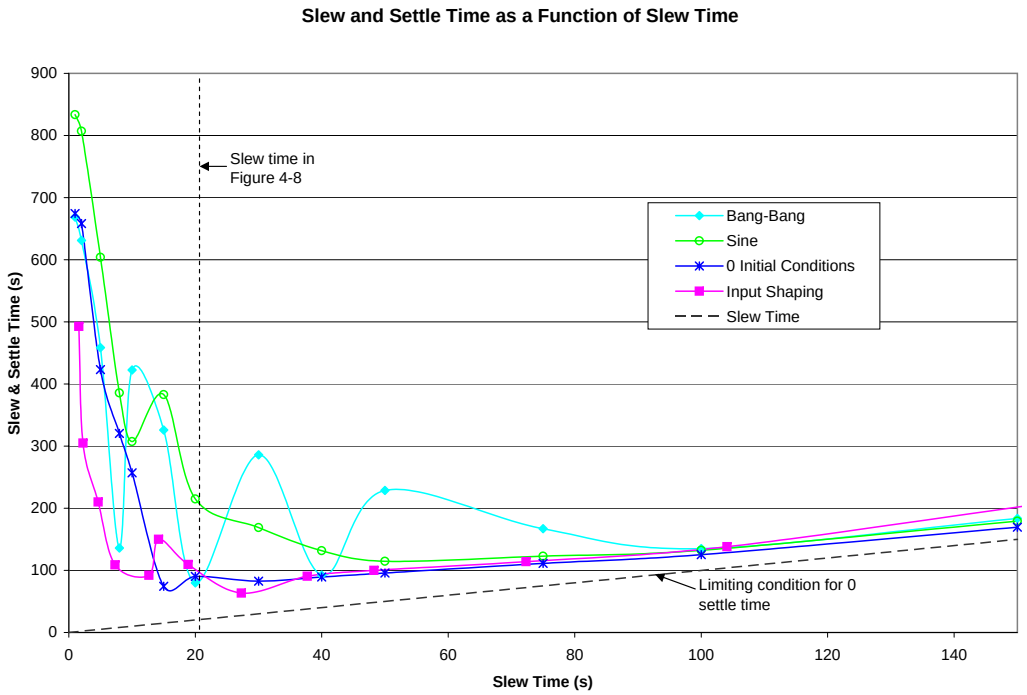

Figure 4-9: Slew and Settle Time as a function of Slew Time

it is clear that there is an optimal slew time that gives the minimum total slew and settle time. The fast slews have settle times that are much too long. But, as the slew time increases, it tends to dominate the total time, as seen in Figure 4-9. Therefore, for a given system, and a given torque profile, this method allows determination of the optimal slewing time.

4.4.3 Effect of Other Parameters

Thus far, only the effects of the slew time and the torque profile, on the slew and settle time, have been examined. There are a number of additional parameters that can greatly affect the settle time, specifically, the attitude control system (ACS) bandwidth and the prescribed system damping. The ACS system actually performs the slew. When given a commanded torque profile to follow, the ACS system controls the reaction wheels to perform the slew and settle the system. A higher ACS bandwidth generally gives more control authority, and can therefore better control the system and provide a lower settle time. However, if the ACS bandwidth is too high,

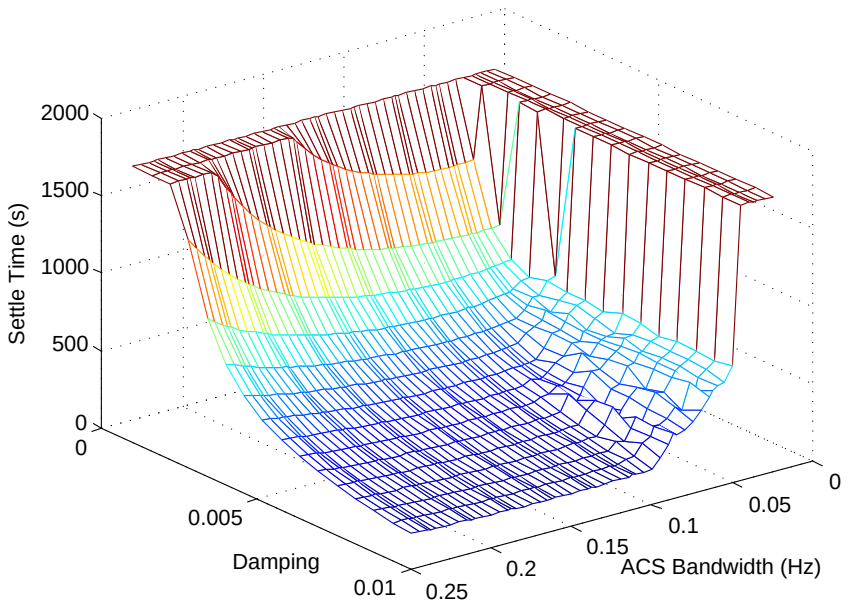

Figure 4-10: Settle Time as a function of Damping and ACS Bandwidth

it approaches the frequency of the first solar panel mode and causes long settling times.

The system damping is a prescribed modal damping of the entire system. The system will naturally dissipate some energy, and the damping describes the amount of dissipation. Therefore, a system with higher damping will dissipate more energy and thus settle quicker. To examine these effects, a system with a 20 second slew and a zero initial condition torque profile is utilized.

Figure 4-10 shows the effects of both ACS bandwidth and damping. The plateau at large values of settle time represents the systems that did not settle in the time allotted. As expected, as the damping increases, the settle time drastically decreases. The ACS bandwidth has a slightly more complex relationship. In general, increasing the ACS bandwidth, to a certain extent, decreases the settle time. However, as the bandwidth continues to increase, it gets closer to the frequency of the first solar panel mode and the settle time starts to increase with increasing bandwidth. Also, at low levels of ACS bandwidth, there is a crinkling effect visible in the graph. The crinkling is a result of the disturbance present during and after the slew. When the ACS bandwidth is very low, the disturbances can cause enough additional vibration

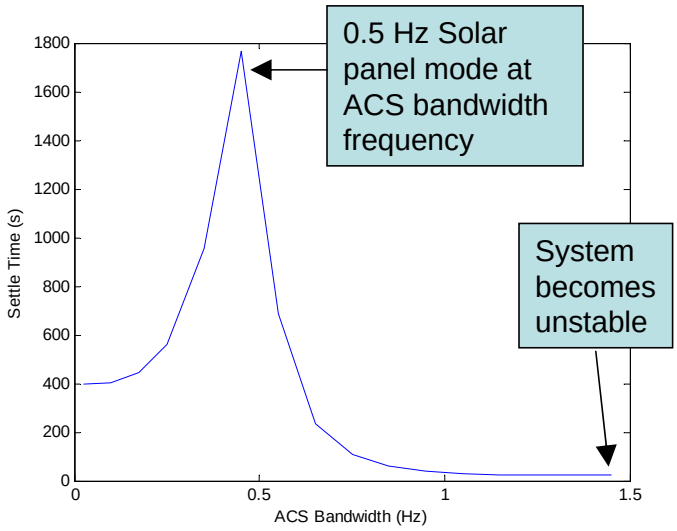

Figure 4-11: Settle Time as a Function of ACS Bandwidth

to excite the jitter above the settling threshold, even after the slewing vibrations have mostly settled. Since there is a randomized component of the disturbance, the settle time sometimes increases and sometimes does not, causing the crinkling seen in the figure. This effect is not present at higher values of ACS bandwidth because the ACS system has more control authority and keeps the vibration due to the RWA disturbance below the threshold.

In most cases, the ACS bandwidth is generally very low. However, if it is pushed up higher than the first solar panel mode, then very fast settle times can be achieved. There is a large peak in the settle time when it lies on top of or near the first solar panel mode at 0.5 Hz. However, when the bandwidth is significantly above 0.5 Hz, the settle time decreases to almost nothing. The sum of the slew and settle times essentially equals the slew time, as seen in Figure 4-11. This performance comes at the cost of stability margin, and many designers might be wary of such a high ACS bandwidth. However, if lower stability margin is acceptable, then better performance can be achieved.

4.5 Slew and Settle Analysis Conclusions

The slew and settle analysis is a way to characterize a mission operations metric, as it represents the amount of time the system is out of operations every time it points to a new location. There are many factors to take into account in optimizing the slew and settle time including:

- Reaction wheel torque distribution
- Torque profile selection
- Slew time
- ACS bandwidth
- System damping

Each of these areas involves many different options and trade studies. The optimal answers depend on the specific telescope realization, but some general conclusions can be drawn. First, a reaction wheel torque distribution that minimizes wheel speed and torque provides the minimum wheel size necessary to complete the slew. This is desirable because smaller wheels have less mass and less disturbance. The torque profile analysis shows that the zero initial condition profile and the time optimal command input shaping profile both gave better performance than the other two profiles. The zero initial condition profile was chosen because it does not require an optimization that can potentially encounter convergence problems. Also, the input shaping profile is contingent upon knowing the frequency of the solar panel mode, which could be difficult to assess accurately before the system is operational, though robustness techniques have been developed to help mitigate this concern [50]. Since the torque profile is purely software code, the profile could be changed from a zero initial condition profile to a time optimal command once a system is chosen.

The slew time was found to have a strong effect on the settle time; settle time decreases as slew time increases. This means that there is an optimum slew time that resides at a midrange slew value: between 20 and 60 seconds, depending on the

system. The ACS bandwidth should be at one of two values of settle time minimums, either below or above the solar panel mode. The conservative designer would use a low ACS bandwidth, on the order of 0.1 Hz. Finally, the system damping should be as high as possible. Unfortunately, this is not something that most designers have control over, but instead, the effects of a range of possible damping values on the settle time should be examined to ensure a robust system at all possible damping levels. Also, since the solar panel mode tends to be the problem, damping augmentation of the solar panels could be used to improve performance. Overall, this analysis can provide a system with superior slew and settle characteristics to improve overall mission operations.

Chapter 5

Control Architecture Analysis of a Single Telescope Realization

The MOST model contains multiple different controllers that were introduced in Chapter 3. These controllers all work well individually, but it is also important to consider them together as a system. When the controllers combine, they interact. This can lead to beneficial effects such as combinatory performance improvement, but can also cause adverse results such as loss of stability margin, or even an unstable system. Therefore, it is important to examine the effects of combining multiple control systems.

Additionally, each control system is generally designed to influence a particular performance metric. However, the control systems often influence metrics other than the one that was originally intended. They can affect other optical or mission performance metrics in positive ways, and affect the control metrics in negative ways. Table 5.1 identifies the interactions between the different control systems and performance metrics.

The mass and OTA cost are not included in this table, since the control systems do not directly affect either metric. However, it is possible to get indirect improvement in OTA cost and mass by utilizing control. The improvement in optical performance due to the addition of controls can permit low-mass and low-cost designs that would not have otherwise met the requirements to become viable design options, which

Table 5.1: Control System Interactions

	Performance Metric				
Control System	LOS Jitter	WFE	Settle Time	Sensitivity	Control Effort
ACS	x	x	x	x	x
FSM	x			x	x
Wavefront	x	x		x	x
Petal	x	x		x	x
Isolation	x	x	x		

essentially improves the OTA cost and mass.

In addition to understanding the effects of each control system on all performance metrics, it is also important to determine the amount of control that should be applied through each control system. Therefore, this chapter examines the control system combinations for two telescope systems: a monolithic aperture system, and a segmented aperture system. Some key parameters of the two systems can be seen in Table 5.2. One key parameter to note is the areal density is set at five kg/m^2, which is the lowest areal density considered. Therefore, these are extremely lightweight systems with a large amount of flexibility. The structural FEM and disturbance model are identical for all designs within each type of system (monolithic system 1, or segmented system 2). Therefore, within each type of system, all changes in performance are due to the changes in the control systems. The remainder of this chapter will examine the control interactions for each of these two systems. For each system, this chapter will first consider combinations of two controllers, then continue with a tradespace analysis of all controllers combined together.

5.1 Monolithic Aperture System

The key features of the monolithic aperture system examined in this tradespace are described in Table 5.2. A sample of the general design can be seen in the left side of Figure 2-3. This design is a compact, low areal density design. The system is light-weight, and has the baseline performance shown in Table 5.3.

Since there must be some ACS control at all times, the baseline performance is

Table 5.2: Key Parameters for Telescope Systems Analyzed in Chapter 5

Parameter	**System 1**	**System 2**
Mirror Type	Monolithic	Segmented
F#	1.0	1.0
Mirror Diameter (m)	3.0	3.0
Areal Density (kg/m^2)	5.0	5.0
Slew Time (s)	40	40
Damping Ratio	0.5%	0.5%
Bus Isolator Frequency (Hz)	2	2
RWA Isolator Frequency (Hz)	10	10

Table 5.3: Baseline Performance of Monolithic Aperture System

Parameter	**Result**
LOS Jitter	0.29 mas
WFE	1.26 nm
Slew and Settle Time	400 s
Sensitivity	1.02

obtained using an ACS bandwidth of 0.025 Hz. The FSM and wavefront controllers are inactive. The control effort is not included in Table 5.3 since it is a normalized quantity and thus is meaningless unless it is compared to other designs, or used with a constant relating it to power. It will, however, be included in the tradespace analysis. Also, although the isolator frequencies have a direct effect upon many of the performance metrics, they are not considered because they have been previously studied in References [52, 55]. The utilized combination of two hertz for the bus isolator and ten hertz for the reaction wheel isolator has been shown to have beneficial performance characteristics while staying within the realm of physically possible isolators.

In order to study the control interaction characteristics, a full-factorial trade study of the control parameters was run. The controller bandwidths (or penalty in the case of the wavefront controller) are varied incrementally throughout the ranges in Table 5.4. In order to examine the effects of the controls, the performance metrics will be presented as functions of two of the control variables for easy visualization. Then, a tradespace of many designs varying all three control system parameters will

be presented.

Table 5.4: Monolithic System Control System Parameters

Parameter	**Bandwidth/Control Cost**
ACS Bandwidth (Hz)	0.0025 - 1.5
FSM Bandwidth (Hz)	0 - 400
Wavefront Control Penalty	∞ (no control), 1×10^{-7} - 1×10^{-12}

5.1.1 Two-Dimensional Control System Interactions for a Monolithic Aperture System

It is possible to show a single performance metric as a function of two different control system parameters. These three-dimensional plots of the interactions can provide powerful insights into how the control systems combine with the rest of the model. Select combinations of controller and performance metrics that have interesting interactions will be presented in this section.

All three control systems affect the sensitivity, and thus the stability margin of the system; the first set of graphs in Figure 5-1 shows the sensitivity interactions. The three plots show the sensitivity as a function of two out of three of the control parameters. The third control system parameter (that is not in the plot) is held constant. When the FSM or wavefront control is not being considered, it is absent from the system. When the ACS is not being examined, it is set at a constant, relatively low bandwidth of 0.025 Hz, and cannot be turned off, since the ACS must be present to control the rigid body modes of the system. Therefore, any interactions visible in the plots are due to the two control parameters being examined.

Figure 5-1(a) shows the sensitivity as a function of the ACS and FSM bandwidths without any wavefront control. As the ACS bandwidth increases, the sensitivity increases. The sensitivity is rather low until it approaches the solar panel mode at 0.5 Hz. It then remains constant at a higher value until it approaches another mode (near a bandwidth of 1.5 Hz), where it increases again. Also, as the FSM bandwidth increases, the sensitivity increases. These two trends are not surprising; the combined

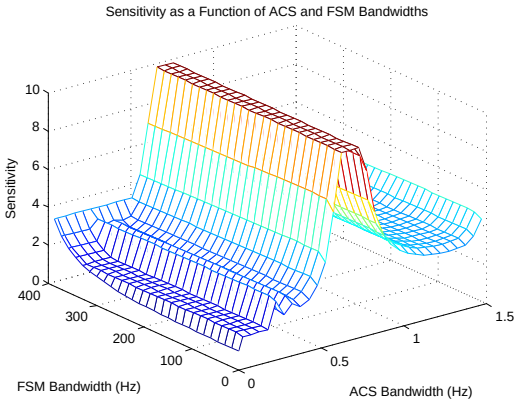

(a) Sensitivity as a Function of ACS and FSM Bandwidths with no wavefront control

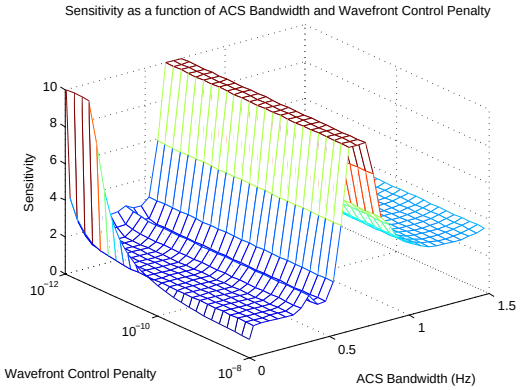

(b) Sensitivity as a Function of ACS Bandwidth and Wavefront Control Penalty with no FSM control

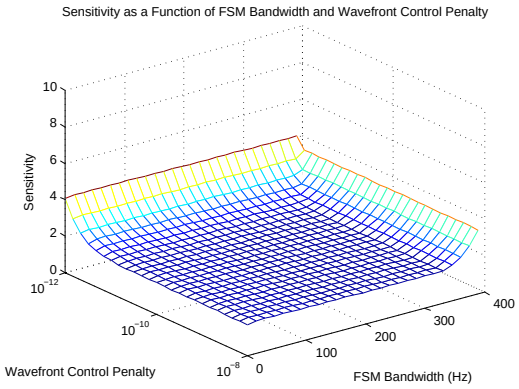

(c) Sensitivity as a Function of FSM Bandwidth and Wavefront Control Penalty with ACS Bandwidth of 0.025 Hz

Figure 5-1: Sensitivity as a Function of Controller Parameters for a Monolithic Aperture System

sensitivity tends to be near the worst case of the two individual sensitivities (Figures 3-3 and 3-5) at the respective bandwidths. The only exception is that the sensitivity at very high ACS bandwidths is larger here than it was without the FSM control. But, the overall trend is still similar.

Figure 5-1(b) shows the sensitivity as a function of the ACS bandwidth and the wavefront control penalty. Unlike the previous case, this plot does not follow the same trends as the individual cases from Chapter 3 of the sensitivity versus control. In general, as ACS bandwidth increases, the sensitivity still increases. Low wavefront control penalty implies high wavefront control bandwidth, so, as expected, when the wavefront control penalty decreases, the sensitivity also rises. At higher wavefront control penalties (lower wavefront control bandwidths), the sensitivity increases due to the ACS control tends to dominate; the wavefront controller contributes to the high sensitivity only when a large amount of wavefront control is applied.

Another interesting feature in Figure 5-1(b) is that the sensitivity is quite high at very low ACS bandwidths. This is due to the interactions between the piezo-electric actuators and the tip and tilt motion of the mirror. As mentioned previously, the piezos can induce tip and tilt in combination with other Zernikes. However, these Zernikes are not included as a part of the wavefront control sensor, or in the performance metric used for the controller design, since they cannot be directly controlled. Also, since the center of gravity of the system is slightly offset from the geometric center of the system, when the mirror changes shape and the center of gravity of the mirror moves, it creates a small torque on the system. When the ACS bandwidth is extremely low and the wavefront control bandwidth is very high, the ACS controller has difficulties overcoming these torques. This combination results in the visibly high sensitivity.

Figure 5-1(c) shows the sensitivity as a function of the FSM bandwidth and the wavefront control penalty. As the wavefront control penalty decreases and the amount of wavefront control increases, the sensitivity rises. Also, as the FSM bandwidth increases, the sensitivity rises as well. However, there is a large, flat region of the sensitivity surface where relatively large amounts of control can be applied with only

a minimal rise in sensitivity. These designs which utilize a lot of control and have very little sensitivity penalty are most desirable.

The optical performance can also be analyzed in terms of multiple controllers. The LOS jitter and WFE as functions of the applicable control parameters can be seen in Figure 5-2. These particular graphs are included because they represent the most interesting performance metrics that are affected by multiple controllers, as shown in Table 5.1.

Figure 5-2(a) shows the LOS jitter as a function of ACS and FSM bandwidths. As intended, increasing the FSM bandwidth substantially improves the LOS jitter performance. Also, the LOS jitter varies with different ACS bandwidths. There are a few "bumps" in the surface near key system modes where the interactions with the ACS system deteriorates performance. However, overall, ACS bandwidth improves optical performance by stabilizing the rigid body motions of the mirror that contribute to the LOS jitter. If the ACS bandwidth were reduced to zero, then the LOS jitter would become infinite because the system would become unstable. This improvement is difficult to see in this particular graph due to the discrepancy in the amount of improvement due to the FSM and ACS systems; in these ranges of bandwidths considered, the FSM can improve the LOS jitter by over 0.2 mas, while the ACS only improves the jitter by about 0.02 mas, a full order of magnitude less.

Figure 5-2(b) shows the LOS jitter as a function of FSM bandwidth and wavefront control penalty. Here, both controllers have a significant effect. The FSM directly corrects for LOS jitter in the optical path, while the wavefront control helps minimize the LOS jitter contribution due to the vibration of the primary mirror. With the addition of wavefront control, the LOS jitter remains constant for a long range of control penalties, before quickly dropping off to improved LOS jitter values. This nonlinear relationship suggests that there is a minimum amount of wavefront control effort that must be applied to have any significant effect on the LOS jitter performance. Overall, the surface is smoothly decreasing in both directions, so increasing the amount of either FSM or wavefront control can significantly improve the LOS jitter performance.

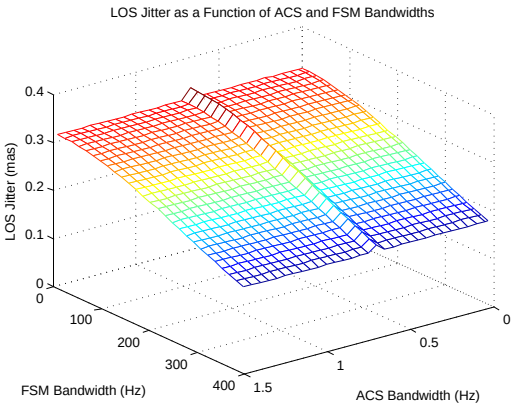

(a) LOS Jitter as a Function of ACS and FSM Bandwidths, no wavefront control

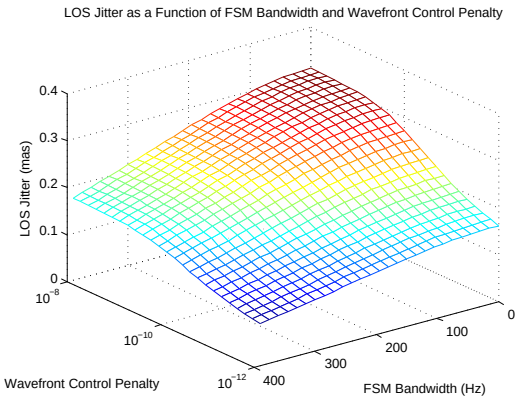

(b) LOS Jitter as a Function of FSM Bandwidth and Wavefront Control Penalty, ACS bandwidth of 0.025 Hz

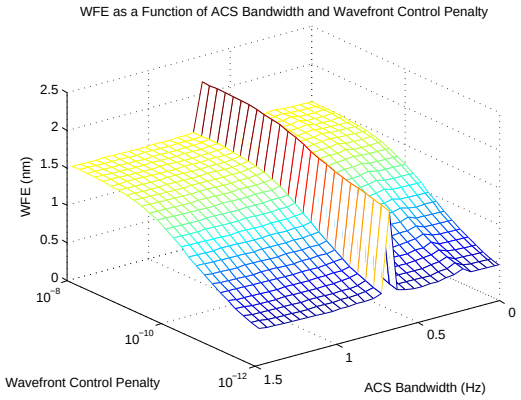

(c) WFE as a Function of ACS Bandwidth and Wavefront Control Penalty, no FSM control

Figure 5-2: Performance as a Function of Controller Parameters for a Monolithic Aperture System

Finally, Figure 5-2(c) shows the wavefront error as a function of the ACS bandwidth and wavefront control penalty. As expected, increasing the amount of wavefront control improves the WFE performance. The effects of the ACS bandwidth on the optical performance are still small, but are more pronounced than in Figure 5-2(a). There are multiple "humps" along the lines of increasing ACS bandwidth. Also, these humps are larger when there is a large amount of wavefront control applied. Therefore, it is desirable to choose a bandwidth that resides within one of the valleys to optimize the performance.

The monolithic aperture system clearly has trade-offs to consider. The control system interactions combine to produce both good optical performance effects and undesirable stability margin effects. The FSM control and wavefront control both contribute to good LOS jitter performance, and the wavefront control significantly lowers the WFE. However, all three controllers contribute the the sensitivity increases. Although it appears that the ACS system only provides marginal performance benefits, it is important to remember the strong effect of the ACS bandwidth on the settle time. The larger ACS bandwidths may be necessary to meet settle time requirements. These figures illustrate some of the trade-offs, but they are limited in that they can only consider two control systems at a time. Therefore, the following section will present a tradespace of results when all control systems are implemented together.

5.1.2 Monolithic Aperture Control Tradespace

The previous section examined the interactions of two control systems, with the third kept constant and inactive when possible. However, the actual system will most likely utilize all three control systems. Therefore, the following plots show the entire tradespace of designs. Each point represents a separate design. The designs are plotted versus two performance metrics and colored by the control system input parameters.

The first set of plots (Figure 5-3) shows the LOS jitter versus the WFE. Each of the three plots shows the same points; the only difference is in the coloring. The most desirable points on the graphs are in the bottom left corner with low LOS jitter and

WFE values.

Figure 5-3(a) shows the LOS jitter and WFE colored by the ACS bandwidth. This plot is not incredibly interesting due to the small effect of ACS bandwidth in this range on the optical performance. It is difficult to see all of the colors in the the figure, since the spacing is very close on this scale, but a zoomed-in version reveals the same trends seen in section 5.1.1. Figure 5-3(b) shows the same plot, colored by FSM bandwidth. The stratification here is very clear. As the FSM bandwidth increases, the LOS jitter decreases. Furthermore, the LOS jitter decreases more at higher bandwidths than at lower bandwidths, so more performance improvement is gained as the bandwidth continues to increase. Finally, Figure 5-3(c) shows the same plot, but colored by the wavefront control penalty. Here, the blocks of designs are shown to be distinguished by the amount of wavefront control. As the control penalty decreases, the LOS jitter and wavefront error also dramatically decrease, creating the blocks seen in the figure. The wavefront control clearly improves both LOS jitter and WFE by reducing the vibrations in the primary mirror.

Similar plots could also be made of any two performance metrics and colored by any of the variable parameters. For example, the settle time and sensitivity are plotted in Figure 5-4, colored by the ACS bandwidth. Here, the designs with ACS bandwidths of 0.0025 and 0.5 Hz are not visible; no designs with these bandwidths settled in the allotted amount of time. In general, increasing bandwidth decreases the settle time. However, there are a few outliers (0.5 Hz and 0.25 Hz) where the ACS bandwidth is near the frequency of the first solar panel mode. This interaction causes very large settle times. The sensitivity does not appear to be highly dependent on the ACS bandwidth; there are large sensitivity ranges for each ACS bandwidth, indicating that there is another parameter responsible for the spread. However, the designs with very high ACS bandwidths that have very low settle times all have sensitivities that are above the acceptable values. Also, the very low bandwidth designs which are not shown have very low sensitivities, so there is a correlation between the sensitivity and ACS bandwidth.

The LOS jitter versus control effort is shown in Figure 5-5. Figure 5-5(a) shows

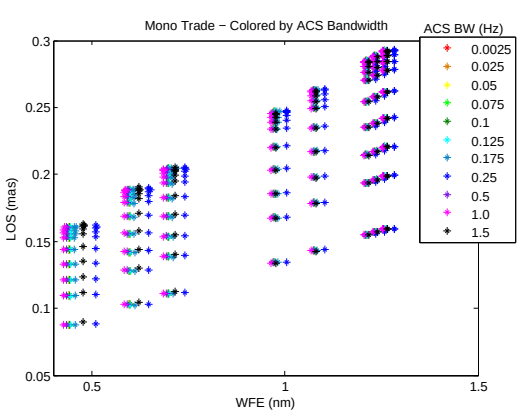

(a) Colored By ACS Bandwidth

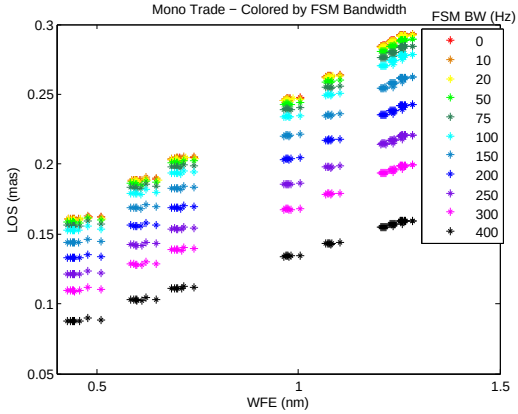

(b) Colored by FSM Bandwidth

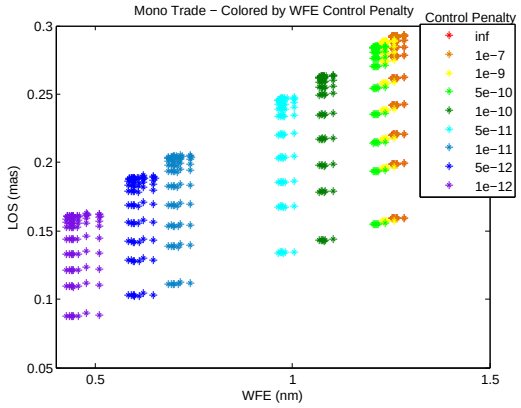

(c) Colored by Wavefront Control Penalty

Figure 5-3: LOS Jitter Versus WFE for a Monolithic System

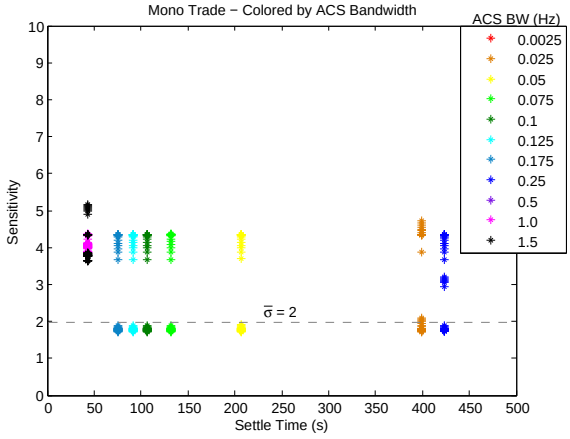

Figure 5-4: Sensitivity Versus Settle Time Colored by ACS Bandwidth

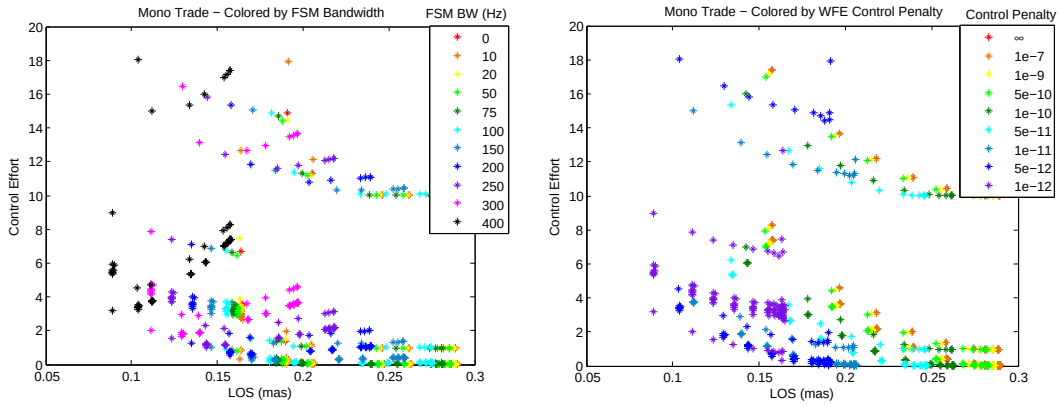

(a) Colored By FSM Bandwidth

(b) Colored by Wavefront Control Penalty

Figure 5-5: Control Effort Versus LOS Jitter

the designs colored by FSM bandwidth, and Figure 5-5(b) shows the designs colored by the wavefront control penalty. As expected, both figures indicate that as more control is applied, the control effort increases and the LOS jitter decreases. There is a Pareto front visible, where any increase in the performance of one variable corresponds to the necessary decrease in the performance of the other. The designs with the lowest LOS jitter all have high control effort, and the designs with the lowest control efforts have higher LOS jitter. There are also dominated designs with poor LOS jitter performance and with high control effort; these designs could have high ACS bandwidths, which would account for the increased control effort without significant LOS jitter improvement.

Two other plots that include stability margin are shown in Figure 5-6. Figure 5-6(a) shows the LOS jitter versus sensitivity colored by FSM bandwidth. It is clear the the FSM bandwidth has a large effect on the LOS jitter. Also, designs with higher FSM bandwidth generally have slightly larger sensitivities. However, the FSM bandwidth is not the predominant contributor to the sensitivity until the FSM bandwidth becomes larger than about 300 Hz; there are many designs with FSM bandwidths at 300 Hz that do not have noticeably higher sensitivities than the low FSM bandwidth designs. Figure 5-6(b) shows the WFE versus sensitivity, colored by wavefront control penalty. Here, again, the WFE gets noticeably better with more wavefront control.

However, unlike Figure 5-6(a), as the control increases, the sensitivity noticeably increases.

Also, there are Pareto fronts visible in both Figures 5-6(a) and 5-6(b). This confirms the trade-off between sensitivity and optical performance. In Figure 5-6(a), the Pareto front contains relatively high FSM bandwidth designs (>100 Hz). Therefore, high FSM bandwidth is a valuable trait. Another input parameter could be used to move along the Pareto front, trading-off cost for performance. The Pareto front in Figure 5-6(b) contains many different wavefront control penalties. Therefore, varying the wavefront control penalty is a way to move across the Pareto front and choose a design.

There are four designs identified on the Pareto front of each plot. The characteristics of each of these designs can be seen in Table 5.5. Points 1a-1d appear on the LOS jitter-sensitivity Pareto front of Figure 5-6(a), while points 2a-2d appear on the WFE-sensitivity Pareto front of Figure 5-6(b). Each design point is marked on both Figures 5-6(a) and 5-6(b) so that the performance can be visualized across both sets of performance metrics. Ideally, the Pareto fronts in the two figures would contain the same types of designs, clearly making those designs the most desirable and allowing for identification of control parameters that give good results across multiple performance metrics. Some of the chosen designs do appear on both Pareto fronts, but others do not.

The control effort and settle time do not appear on either plot, though they must be considered in the overall design selection. The settle time is included in Table 5.5 for reference. As seen previously, the settle time can be changed by varying the ACS bandwidth. As long as there is enough stability margin, the ACS bandwidth can be increased to a level that results in an adequate settle time.

The LOS-sensitivity Pareto front (designs 1a-1d) contains a variety of FSM Bandwidths. There are also various levels of wavefront control; the designs with lowest LOS jitter contain wavefront control, while the low sensitivity designs do not. The WFE-sensitivity Pareto front (designs 2a-2d) contains various levels of wavefront control, but no FSM control. The FSM control does not improve WFE, and since it increases

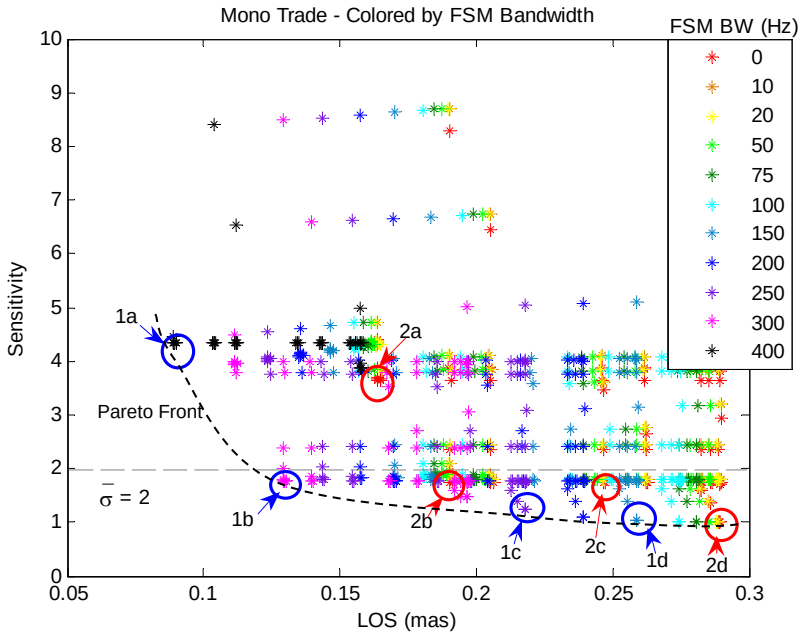

(a) Colored By FSM Bandwidth

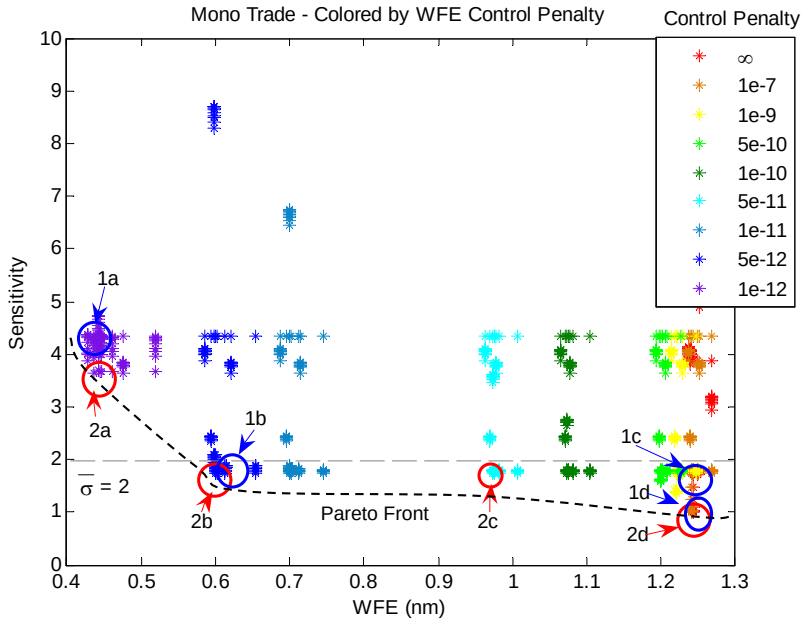

(b) Colored by Wavefront Control Penalty

Figure 5-6: Optical Performance versus Sensitivity

Table 5.5: Select Pareto Designs for the Monolithic System

	ACS BW (Hz)	**FSM BW (Hz)**	**Wavefront Control Penalty**	**LOS (mas)**	**WFE (nm)**	**Sensitivity**	**Settle Time (s)**
1a	0.075	400	$1{\cdot}10^{-12}$	0.089	0.444	4.355	132
1b	0.025	300	$5{\cdot}10^{-12}$	0.130	0.654	1.78	423
1c	0.0025	250	∞	0.218	1.242	1.22	>2000
1d	0.001	150	∞	0.256	1	1.04	75
2a	0.1	0	$1{\cdot}10^{-12}$	0.164	0.445	3.674	107
2b	0.075	0	$5{\cdot}10^{-12}$	0.1902	0.599	1.75	132
2c	0.175	0	$5{\cdot}10^{-11}$	0.2469	0.9821	1.72	75
2d	0.0025	0	∞	0.289	1.242	1.001	>2000

sensitivity, it never appears on the WFE-sensitivity Pareto front.

When considering both Pareto fronts in Figure 5-6, the most promising designs are 1*b* and 2*b*. These designs have some features in common: the ACS bandwidth is in a low range (from 0.025 - 0.075), which allows the system to settle without incurring a large penalty in sensitivity. The FSM bandwidth is quite different; 300 Hz in design 1b and 0 Hz in design 2b. The increased FSM bandwidth results in a decrease in LOS jitter, and only a small increase in sensitivity (0.03). Therefore, it seems worth the sensitivity penalty to use the higher FSM bandwidth. Both designs have equal wavefront control penalties, utilizing the most wavefront control possible without violating the sensitivity constraints ($5{\cdot}10^{-12}$). These specific parameters can be adjusted to obtain a design that meets the needs of the mission, but this provides a preliminary range of control parameters that results in good performance.

When considered together, the plots in this section provide a quantitative means to analyze the effects of utilizing multiple control systems. In some cases, the additive effects are as expected, as in the ACS and FSM case where the controllers do not significantly interfere. This implies that these two control systems could be designed independently, as long as proper stability margin is maintained. However, the wavefront controller tends to interact with the other control systems, resulting in behavior that is difficult to predict.

The tradespace plots also show the direct trade-offs between performance metrics,

and how the performance is affected by the controller parameters. Designs that appear favorable when considering multiple performance metrics appear on the Pareto front, and can be considered "good" designs. However, the two-dimensional Pareto fronts only take two performance metrics into account, so the designs should also be examined in terms of the other metrics.

5.1.3 Favorable Families of Control Architectures for the Monolithic Systems

The previous two sections revealed numerous insights into the effects of the control systems for a given, monolithic aperture configuration. Consequently, observations can be made about the families of control architectures to pursue in greater detail for this particular structural configuration. First, the wavefront control bandwidth should be relatively high, with the wavefront control penalty around $5{\cdot}10^{-12}$. Control penalties near this value provide ample optical performance improvement without severe sensitivity penalties. Also, the addition of the wavefront control provides improvement in both LOS jitter and WFE by attenuating the vibrations in the primary mirror.

The FSM bandwidth can also be relatively high; bandwidths up to 250-300 Hz cause significant LOS jitter improvement with only minimal increases in the sensitivity. However, if the LOS jitter improvement is unnecessary (since the designs all meet the 1.6 mas requirement), then the FSM control may be excluded to avoid unnecessary control effort and complexity.

The ACS bandwidth has been shown to have a significant effect on the sensitivity, but only a small effect on the optical performance metrics. However, the slew and settle time must be maintained. The designs with mid-range ACS bandwidths (0.025-0.125) allow the system to settle in a reasonable amount of time (100-400 s). These bandwidths have low enough sensitivities to be implemented in combination with the other controllers, but still allow the system to settle after the slew.

The specific goals of the mission would help to better define the actual control

architecture. However, these results provide guidelines for promising combinations of control systems to pursue in later design phases. The uncertainty in the system during this phase of conceptual design makes it impossible to choose a specific control architecture, but the trends revealed in this section should remain valid and provide a basis for further analysis. Overall, the monolithic system can achieve very good performance when the control systems are carefully implemented, but caution should be taken to avoid any adverse effects.

5.2 Segmented Aperture System

The segmented aperture system examined in this section has similar parameters to the monolithic system, with the exception of the aperture type. Some key features are described in Table 5.2. The baseline performance of this system can be seen in Table 5.6. As with the monolithic aperture system, the baseline performance is obtained without the use of the FSM, wavefront, and petal controllers, and the ACS system has a bandwidth of 0.025 Hz.

Table 5.6: Baseline Performance of Segmented Aperture System

Parameter	**Result**
LOS Jitter	0.28 mas
WFE	2.26 nm
Slew and Settle Time	420 s
Sensitivity	1.72

Again, a full-factorial design trade of the control parameters is run. The range of values for the parameter inputs used for the segmented system analysis can be seen in Table 5.7. The tradespace will first be examined using three-dimensional surface plots. This shows the variability in a single performance metric due to the interactions of two control systems. Then, the tradespace results will be shown on two-dimensional tradespace plots to visualize the trade-offs between performance metrics.

Table 5.7: Segmented System Control System Parameters

Parameter	Bandwidth/Control Cost
ACS Bandwidth (Hz)	0.0025 - 1.5
FSM Bandwidth (Hz)	0 - 400
Wavefront Control Cost	∞ (no control), 1×10^{-9} - 1×10^{-12}
Petal Bandwidth (Hz)	0 - 50

5.2.1 Two-Dimensional Control System Interactions for a Segmented Aperture System

In the segmented aperture system, there are four possible control systems: ACS control, FSM control, wavefront control, and petal control. Each of these control systems affects the stability margin, thus the sensitivity of the system. Since the sensitivity is common to all control systems, and is the limitation on the amount of control, it will be examined first.

Figure 5-7 shows the sensitivity plotted as a function of every set of two control systems. Figure 5-7(a) shows the sensitivity as a function of the ACS and FSM bandwidths. The sensitivity rises with increasing ACS bandwidth, and is quite high near the solar panel mode at 0.5 Hz. It decreases slightly at higher ACS bandwidths, but it does not return to an acceptable level. This prohibits the very fast settle times that are possible with high ACS bandwidths. It is also possible to see that the FSM bandwidth contribution to the sensitivity is small in comparison with the ACS bandwidth, except at the highest FSM bandwidths.

Figure 5-7(b) shows the sensitivity as a function of the ACS bandwidth and wavefront control penalty. At very low levels of ACS bandwidth, when the wavefront control is included, the sensitivity is extremely high. This is the same phenomenon that was seen in the monolithic case where the piezo-electric actuators can unintentionally induce some components of the tip and tilt Zernikes, and the ACS controller must have a high enough bandwidth to counteract this effect. Once the ACS bandwidth reaches an acceptable level, the sensitivity drops rapidly, and then increases with increasing bandwidth. Also, as the wavefront control penalty decreases, and

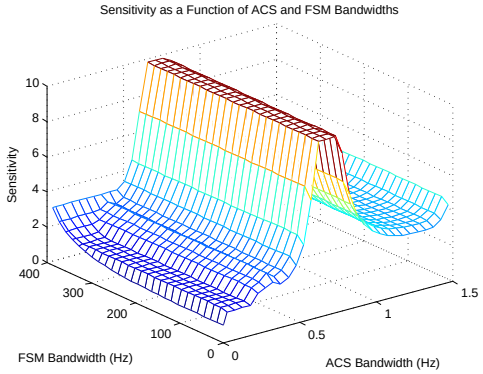

(a) Sensitivity as a Function of ACS and FSM Bandwidths

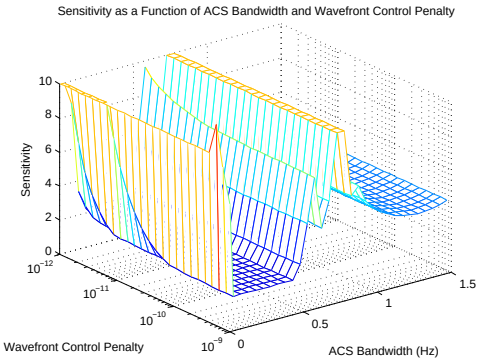

(b) Sensitivity as a Function of ACS Bandwidth and Wavefront Control Penalty

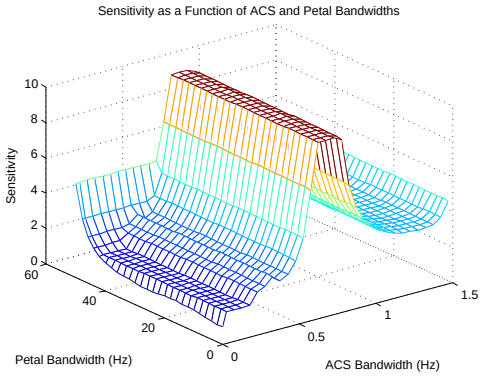

(c) Sensitivity as a Function of ACS and Petal Bandwidths

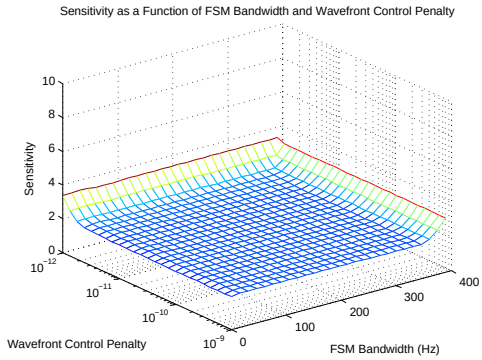

(d) Sensitivity as a Function of FSM Bandwidth and Wavefront Control Penalty

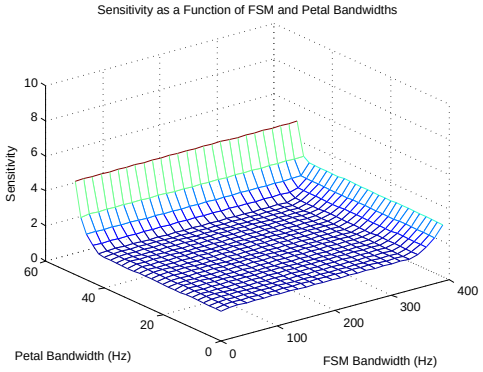

(e) Sensitivity as a Function of FSM and Petal Bandwidths

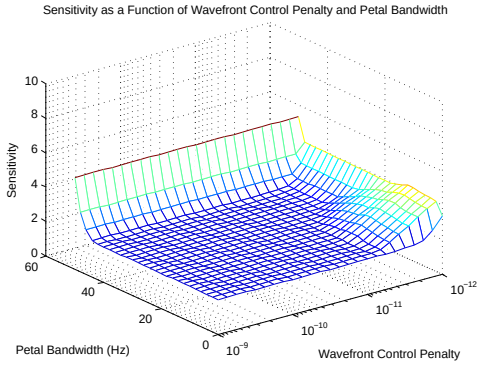

(f) Sensitivity as a Function of Petal Bandwidth and Wavefront Control Penalty

Figure 5-7: Sensitivity as a Function of Controller Parameters for a Segmented Aperture System

more control is applied, the sensitivity increases as expected.

Figure 5-7(c) shows the sensitivity as a function of ACS and petal bandwidths. This plot appears similar to Figure 5-7(a) with ACS bandwidth increasing at the solar panel mode, then remaining unacceptably high at all bandwidths above 0.5 Hz. At low levels of ACS bandwidth, the heightening of the sensitivity due to high petal bandwidths is visible. However, at higher levels of ACS bandwidth, this effect disappears as the ACS controller dominates the sensitivity transfer function.

Figures 5-7(d), 5-7(e), and 5-7(f) all show similar effects. As either FSM, petal, or wavefront control bandwidths increase, the sensitivity increases. In all cases, the sensitivity is low and the sensitivity surface is rather flat at low bandwidth levels. When any of the bandwidths increase, the sensitivity increases. Therefore, the optimal amounts of control would be the combinations of bandwidths where the most control is applied, but the sensitivity surface is surface is still relatively flat and the sensitivity is below two.

It is also important to examine the aggregate performance while utilizing multiple controllers. First, since all controllers have some influence over the LOS jitter, the LOS jitter, as a combination of all controller parameters, is plotted in Figure 5-8. As visible from the plots, the ACS bandwidth in this range has a minimal effect on the LOS jitter. Again, if the ACS bandwidth was reduced to zero, the system would become unstable and the LOS jitter would become very large. However, in the range of ACS bandwidths examined, these effects are small, especially in comparison with the effects of the other control systems.

Increasing the FSM control bandwidth decreases the LOS jitter as desired. Also, the FSM effect on LOS jitter is nonlinear; higher FSM bandwidths contribute to exceedingly better performance. The wavefront control also significantly improves the LOS jitter. There is, again, a nonlinear relationship where increasing wavefront control at a higher bandwidth implies greater performance improvements. Additionally, the petal control contributes to the LOS jitter reduction by stabilizing the primary mirror segments. However, in this case, the LOS jitter quickly decreases with even a small petal bandwidth. The LOS jitter then asymptotes to a constant value at larger

bandwidths, indicating that, unlike the previous two cases, significant performance benefit is gained by adding only a small amount of control, and there is a limit to the performance improvement to be gained by utilizing petal control.

In most cases, the effects of each controller are pronounced in each plot, regardless of which two controllers are being considered. Therefore, the performance is largely combinatory, without adverse effects from including multiple controllers. One interesting interaction can be seen in Figure 5-8(f), which shows the LOS jitter as a function of the petal bandwidth and wavefront control cost. As expected, as either control system applies more effort, the LOS jitter performance improves. However, adding petal control bandwidth has a significantly greater impact when the wavefront control penalty is high (there is not much wavefront control). As the amount of wavefront control increases, the visible improvement due to the petal control disappears. This indicates that there is a limit to the amount of LOS jitter improvement that can be obtained by simply stabilizing the mirror segments. When the wavefront control bandwidth is extremely high, the piezo-electrics actually stabilize the rigid body mirror modes, but at the expense of sensitivity.

The WFE will be examined only in terms of the ACS, petal and wavefront control systems, since the FSM controller has no effect on the wavefront error. The WFE, plotted as a function of each combination of two control parameters, can be seen in Figure 5-9.

The WFE performance appears similar to the LOS jitter performance in Figure 5-8. The effect of the ACS bandwidth on the performance is again visible, indicating that the desirable ACS bandwidths are in the valleys of the WFE surface. The wavefront control contributes to a significant decrease in the WFE; up to a 50% improvement. Also, the petal control significantly reduces the WFE. However, there is again a limit to the amount of improvement due to increasing the petal bandwidth. The petal control can only control the tip and tilt Zernikes of each petal; once these are stable, the control cannot provide additional benefits. As desired, the best performance is obtained by using both wavefront control and petal control. The two systems control complimentary Zernikes, so the combination of the two controllers performs

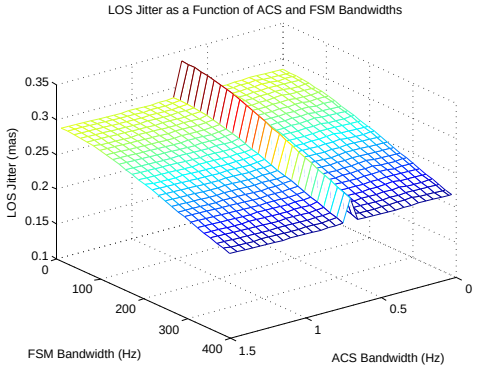

(a) LOS Jitter as a Function of ACS and FSM Bandwidths

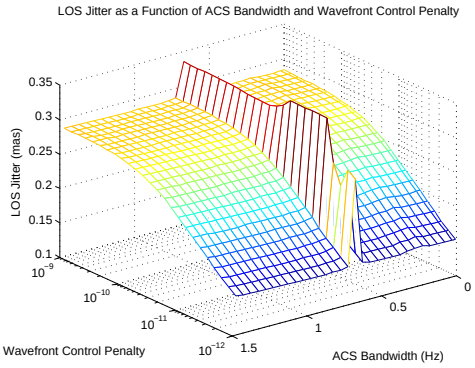

(b) LOS Jitter as a Function of ACS Bandwidth and Wavefront Control Penalty

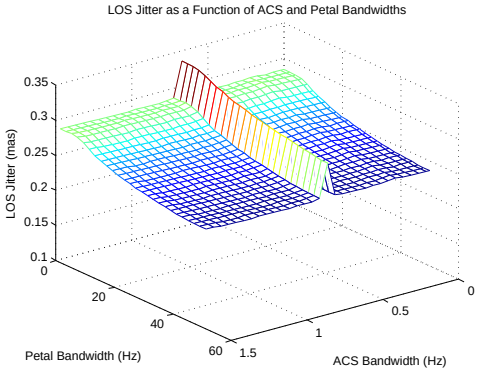

(c) LOS Jitter as a Function of ACS and Petal Bandwidths

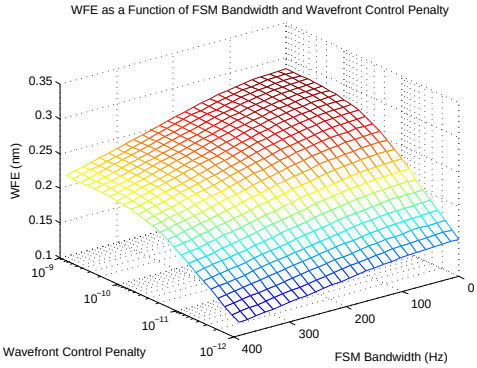

(d) LOS Jitter as a Function of FSM Bandwidth and Wavefront Control Penalty

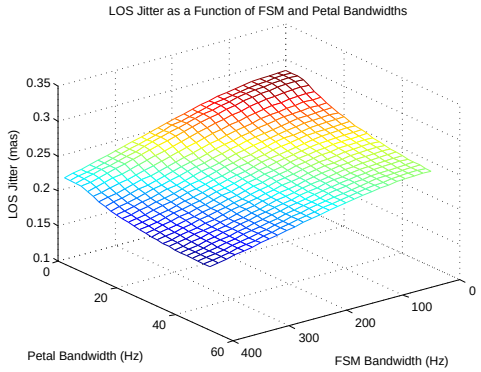

(e) LOS Jitter as a Function of FSM and Petal Bandwidths

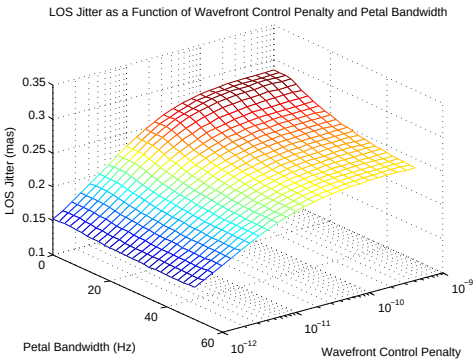

(f) LOS Jitter as a Function of Petal Bandwidth and Wavefront Control Penalty

Figure 5-8: LOS Jitter as a Function of Controller Parameters for a Segmented Aperture System

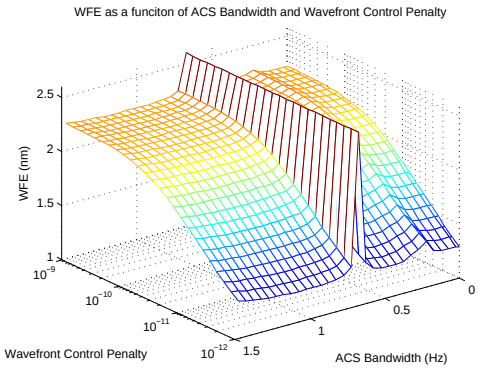

(a) WFE as a Function of ACS Bandwidth and Wavefront Control Penalty

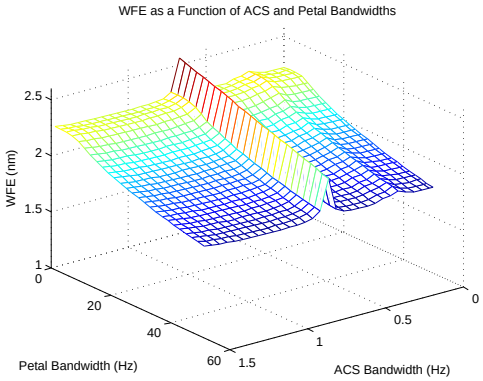

(b) WFE as a Function of ACS and Petal Bandwidths

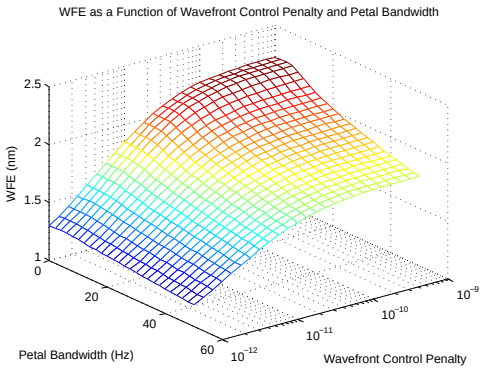

(c) WFE as a Function of Petal Bandwidth and Wavefront Control Penalty

Figure 5-9: WFE as a Function of Controller Parameters for a Segmented Aperture System

best. This is especially true when the sensitivity is limited; the lowest wavefront control penalty (highest wavefront control bandwidth) in Figure 5-9(c) has a sensitivity that is much too high (Figure 5-7(f)), and thus cannot be utilized. The designs with slightly less wavefront control and some petal control have lower sensitivites and good WFE performance, indicating the imporatance of both control systems.

The segmented systems display slightly more complex optical performance and stability control interactions than the monolithic systems. The addition of the petal controller, along with the alternative implementation of the wavefront control, changes the system. Most complications arise in the sensitivity metrics, where the control

systems interact. Particularly, the ACS system in combination with other control systems creates complex interactions that result in potentially high sensitivities. The control system interactions do not affect the optical performance metrics as much. For the most part, these interactions are similar to the combination of the resulting performance of the individual control systems. The magnitudes and amount of improvement due to a given control system change when there are other systems present, but the overall trends remain relatively constant. Overall, these plots provide valuable insight into the system performance when control systems are combined in various ways.

5.2.2 Segmented Aperture Control Tradespace

Since it is also important to examine all four controllers together, the entire tradespace of segmented aperture designs is examined. Two performance metrics are plotted against one another, and the designs are colored by the different control variable inputs. This allows the relative effects of each of the controllers on the performance metrics to be seen. This technique also shows Pareto fronts and indicates which of the control inputs can be used to move along the Pareto front and trade off different performance metrics.

The first set of plots (Figure 5-10) shows the two optical performance metrics: LOS jitter and wavefront error. It is difficult to discern a definite pattern in Figure 5-10(a), which is colored by ACS bandwidth. As seen previously, the ACS bandwidth does have an effect on the optical performance, but it is small compared to the other control influences. Figure 5-10(b) shows the same points colored by FSM Bandwidth. Here, the points are clearly delineated in the LOS direction by the FSM bandwidth, indicating that the FSM controller has a strong influence on reducing the LOS jitter, but does not affect the WFE. Figure 5-10(c) shows the points differentiated by the wavefront control penalty. Here, there are clear blocks of points, indicating that the wavefront control significantly contributes to reducing the both WFE and LOS jitter. The final plot, Figure 5-10(d) shows the points colored by the petal bandwidth. This shows that the petal control also reduces the WFE, and creates the spread within the

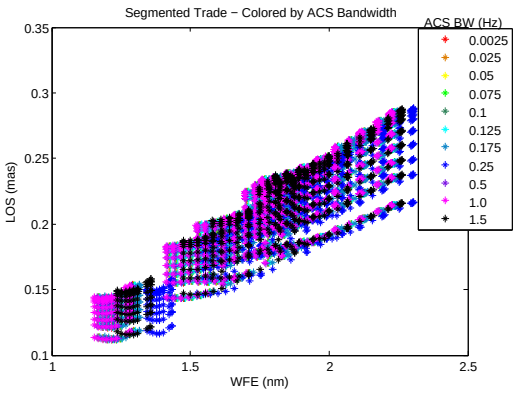

(a) Colored By ACS Bandwidth

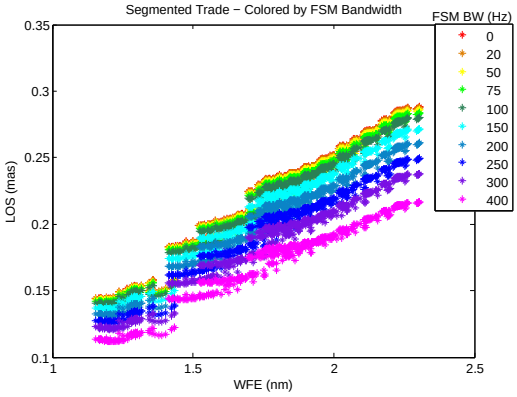

(b) Colored by FSM Bandwidth

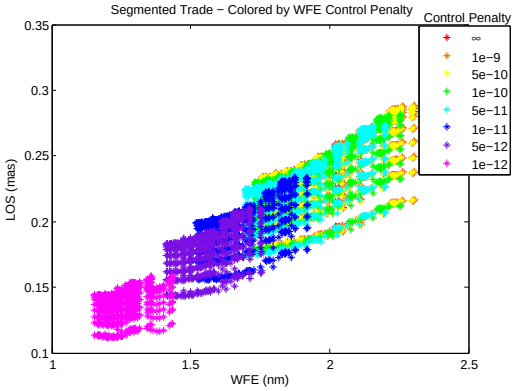

(c) Colored by Wavefront Control Penalty

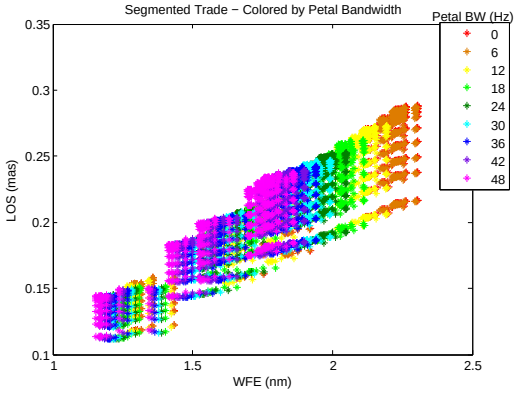

(d) Colored by Petal Bandwidth

Figure 5-10: LOS Jitter Versus Wavefront Error for a Segmented System

"boxes" that are characterized by the wavefront control penalty and can be seen in Figure 5-10(c).

Also, as the wavefront control penalty becomes smaller (the points of low WFE and LOS), the size of the "boxes" shrinks. This indicates that the petal controller causes less WFE reduction when the wavefront control penalty is low. However, utilizing a lot of wavefront control and petal control together clearly gives the best overall WFE performance.

The settle time versus sensitivity can be seen in Figure 5-11. As with the monolithic system (Figure 5-4), there are a number of ACS bandwidths (0.0025, 0,25 and 0.5 Hz) not visible on the plot because those systems did not settle in the time allot-

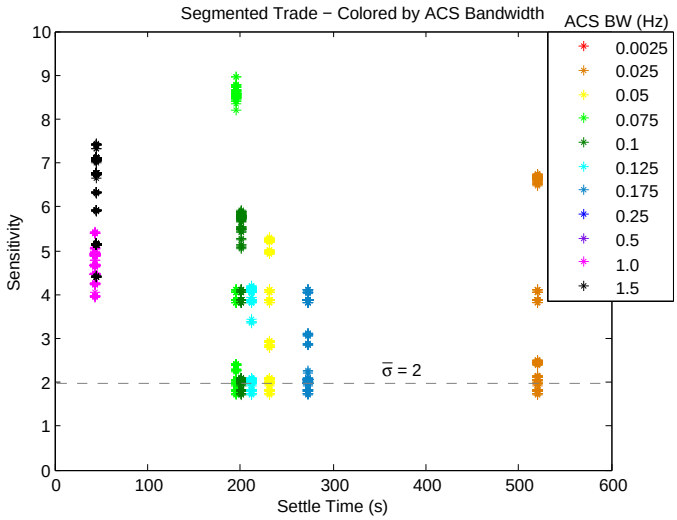

Figure 5-11: Sensitivity Versus Settle Time Colored by ACS Bandwidth

ted. This is because the ACS bandwidth is either too low, or near the frequency of the solar panel mode. None of the systems with high ACS bandwidth and extremely low settle time meet the sensitivity requirement. The designs with bandwidths in the range of 0.05 to 0.175 Hz all result in reasonable settle times and can have sensitivities below the threshold of two.

The sensitivity versus optical performance is also important. Figure 5-12 shows the sensitivity versus LOS jitter, colored by the ACS and FSM Bandwidths. Figure 5-12(a) shows the designs colored by the ACS bandwidth. There is a strong horizontal stratification, indicating that changing ACS bandwidth has a small effect on the LOS jitter, but greatly affects the sensitivity. Figure 5-12(b) again shows the sensitivity versus jitter, but colored by FSM bandwidth. There is not a strong stratification in either direction, but there is more delineation in the horizontal direction, indicating that the FSM bandwidth affects the LOS jitter more than the sensitivity. However, there is also a trend of increasing sensitivity with increasing FSM bandwidth.

There is also a Pareto front drawn on each of the plots in Figure 5-12. The Pareto front is not entirely smooth, and the sensitivity jumps to just above two when the LOS jitter values are reduced below 0.2 mas. Also, most of the designs along the Pareto front have a relatively high FSM bandwidth (300 Hz). The extremely high FSM bandwidth designs (400 Hz) all have sensitivities larger than the requirement

value of two. However, FSM bandwidths between 200 and 300 give good performance with only a small increase in sensitivity.

Figure 5-13 shows the sensitivity versus the wavefront error. Figure 5-13(a) is colored by the wavefront control penalty. Here, as expected, as the amount of wavefront control increases (wavefront control penalty decreases), the WFE decreases, and the sensitivity increases, signifying that improved performance can only be gained at the expense of stability margin. Figure 5-13(b) shows the sensitivity versus WFE colored by the petal bandwidth. Again, within each block of designs of constant wavefront control, increasing the petal bandwidth improves performance but decreases stability margin. Therefore, once a level of wavefront control has been chosen, the petal bandwidth can be used to move across the Pareto front, trading off performance and sensitivity.

A Pareto front is again drawn on each of the plots in Figure 5-13. This Pareto front contains designs of many wavefront control penalties and petal bandwidths. This indicates that both the wavefront and the petal control can be used to move along the Pareto front, trading off wavefront error for sensitivity.

There are a series of design points labeled on Figures 5-12 and 5-13. Design points 1a-1d are on the LOS-sensitivity Pareto front of Figure 5-12, and points 2a-2d are on the WFE-sensitivity Pareto front in Figure 5-13. Both sets of points are labeled on both sets of plots (Figures 5-12 and 5-13) to see how the designs perform in terms of the other performance metrics. Ideally, the designs would be on both Pareto fronts, indicating that there is good performance in terms of all three metrics. The control parameters and performance outputs of each labeled design are listed in Table 5.8.

The settle time and control effort are absent from this table, and should also be considered in the final design decisions. In general, the settle time can be altered by changing the ACS bandwidth, as long as enough stability margin remains. The control effort simply scales up with increasing control bandwidth.

Of the labeled points, designs 1b and 2b have the best aggregate performance. However, while the sensitivities are not outrageously high, they are above two. If this slightly lower stability margin were acceptable and the sensitivities were permitted

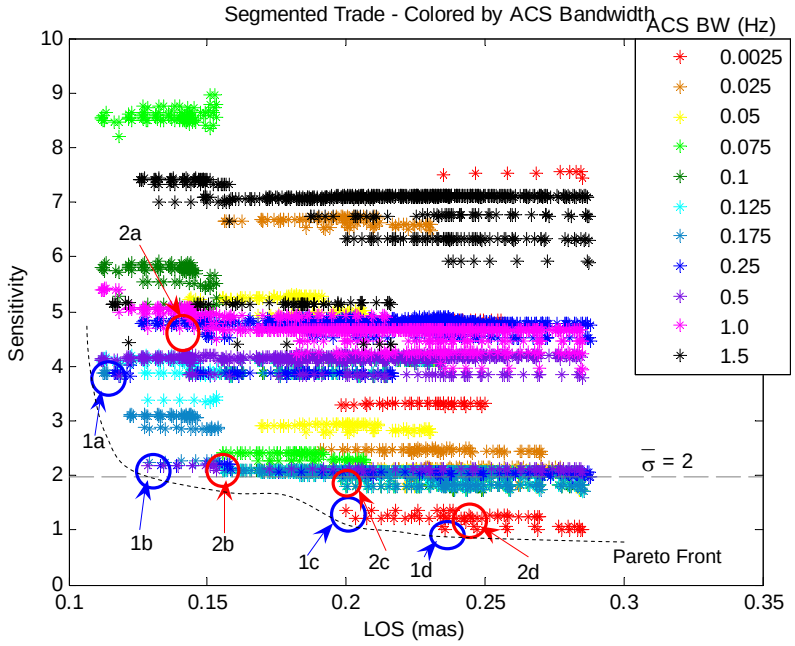

(a) Colored By ACS Bandwidth

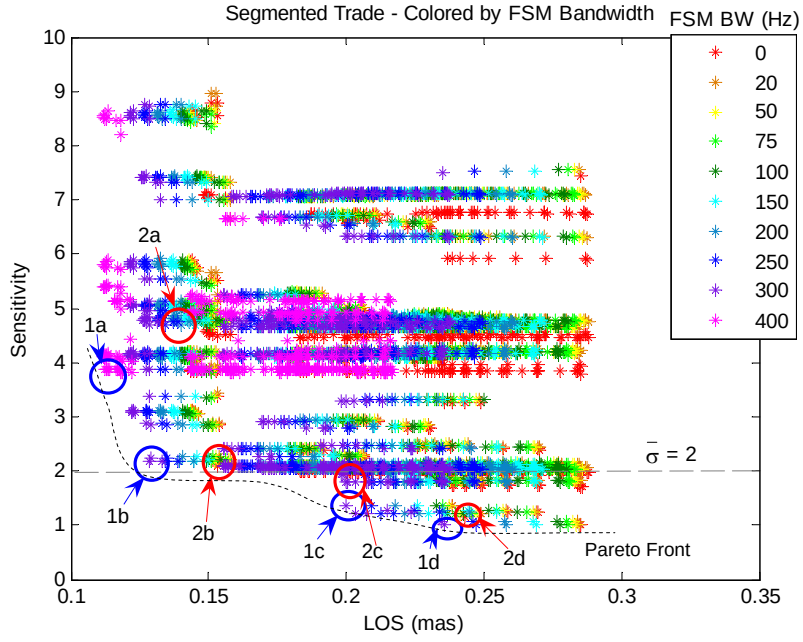

(b) Colored by FSM Bandwidth

Figure 5-12: LOS Jitter versus Sensitivity for a Segmented System

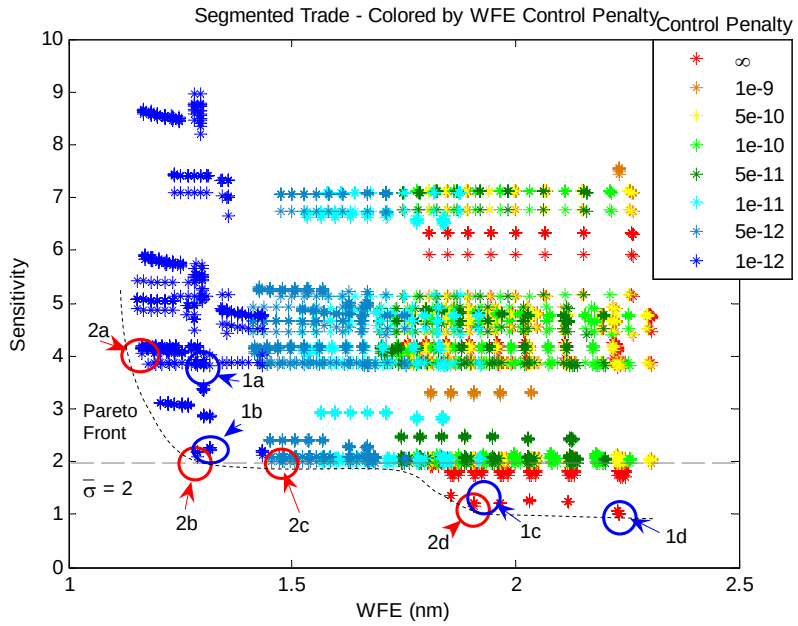

(a) Colored by Wavefront Control Penalty

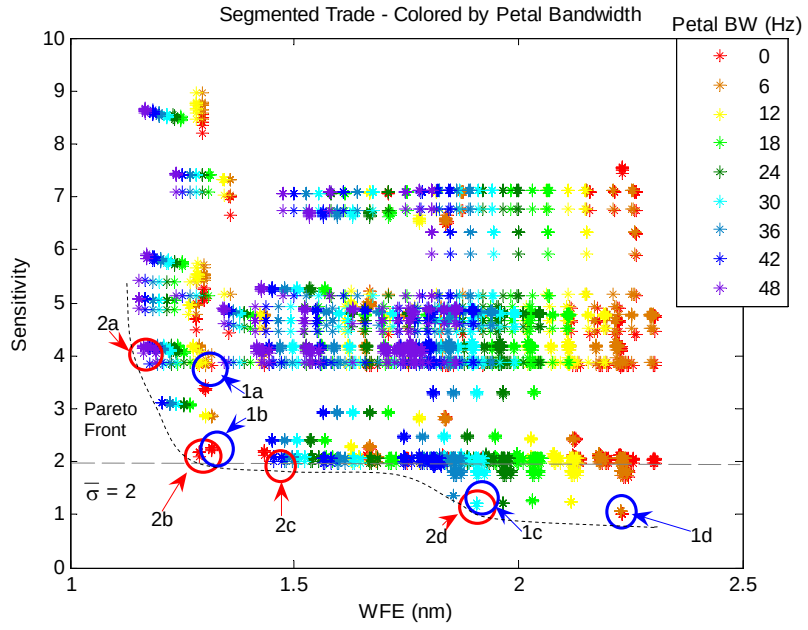

(b) Colored by Petal Bandwidth

Figure 5-13: WFE versus Sensitivity for a Segmented System

Table 5.8: Select Pareto Designs for the Segmented System

	ACS BW (Hz)	**FSM BW (Hz)**	**Wavefront Control Penalty**	**Petal BW** (Hz)	**LOS (mas)**	**WFE (nm)**	**Sensitivity**
1a	0.125	400	$1{\cdot}10^{-12}$	0	0.118	1.302	3.813
1b	0.175	300	$1{\cdot}10^{-12}$	0	0.129	1.317	2.244
1c	0.0025	300	∞	30	0.218	1.908	1.213
1d	0.0025	300	∞	0	0.256	2.234	1.002
2a	0.175	250	$1{\cdot}10^{-12}$	48	0.145	1.191	4.045
2b	0.175	0	$1{\cdot}10^{-12}$	0	0.154	1.316	2.206
2c	0.075	0	$1{\cdot}10^{-11}$	42	0.200	1.565	1.985
2d	0.0025	0	∞	30	0.243	1.908	1.149

to be above two, these designs would prove to be good. They have a lot of wavefront control, but no petal control to reduce the WFE. The FSM bandwidth is variable within the range of bandwidths that does not greatly affect the sensitivity, and the ACS bandwidth is at a mid-range value.

If the sensitivity requirement of two is a strict requirement, then designs 1c and 2c would be the most promising. Both of these designs use some petal control; enough to provide significant optical performance improvement without a large increase in sensitivity. These designs differ in the amounts of wavefront and FSM control applied; design 1c includes no wavefront control and high FSM bandwidth, while design 2c includes moderate wavefront control, but no FSM control. The difference is derived from the particular performance metric being minimized: 1c is on the LOS Pareto front, and 2c is on the WFE Pareto front. Therefore, either of these design could be considered good, depending on the desired outcome. Design 2c would most likely be more desirable, as it has a lower WFE. All designs meet the 1.6 mas LOS jitter requirement, but none of the designs meet the 1 nm WFE goal. Given that the WFE goal cannot be met with this particular structural configuration, WFE should be minimized as much as possible.

5.2.3 Favorable Families of Control Architectures for the Segmented Aperture Systems

Though no definite control architecture can be selected for this system at this stage of design, favorable traits of a potential control architecture can be identified. These traits provide a starting point for further analysis in the subsequent design phases. First, the wavefront controller can provide the most optical performance improvement. However, it does so at the expense of sensitivity, actuator channels, and control effort. The designs with the highest levels of wavefront control (wavefront control penalty of $1{\cdot}10^{-12}$) all have sensitivities above the requirement value. Instead, slightly less wavefront control should be utilized to gain performance benefit without large sensitivity and control effort penalties.

The petal control can also stabilize the mirror segments, decreasing both LOS jitter and wavefront error. A mid-range petal controller bandwidth (25-40 Hz) should be used to gain such improvement. Also, a small amount of petal control can result in a significant performance improvement. Overall, the systems that use some wavefront control (mid-range control penalty) and some petal control (mid-range petal bandwidth) seem to have the most promise; there is considerable optical performance improvement without dramatic sensitivity increases. However, this involves the utilization of two separate control systems, which introduces additional avionics complexity.

The FSM control could also provide improvement in the LOS jitter. All Pareto-optimal points on the sensitivity-LOS Pareto front have relatively high FSM bandwidth ($\sim$300 Hz). However, all designs meet the LOS jitter requirement, so this performance improvement may prove to be unnecessary, and the FSM control may result in needless complexity. Therefore, systems with relatively high FSM control and systems with no FSM control should both be examined further, since they provide very different benefits.

The ACS bandwidth had little effect on the optical performance. However, the slewing and settling are necessary, and the ACS bandwidth must be large enough to

permit the system to settle after a slew. Therefore, the bandwidth must be at least 0.05 Hz for settling, but should remain below about 0.175 Hz to meet the sensitivity constraints.

These ranges of bandwidths and control system options provide a starting point for further exploration. The subsequent design phases will further examine these possibilities to determine a control architecture for the system when the uncertainty in the overall design is substantially reduced.

Overall, The segmented aperture system has been shown to have more complex control interactions than the monolithic system due to the addition of controllers. However, it is still possible to examine the specific controller interactions as well as the performance metric trade-offs resulting from the control architecture selection. Also, potentially favorable control architectures are identified.

5.3 Summary

This chapter examined two systems, one with a monolithic aperture and one with a segmented aperture, in the presence of multiple control systems. For both systems, the control interactions were first examined two at a time to determine the resulting cost and performance. In many cases, the interactions were as expected, with combined performance being similar to the sum of the trends of the two individual controllers. However, certain cases revealed more complex relationships where the control systems interacted and produced unanticipated results. Then, the control systems were all examined together and presented as a part of a tradespace. These plots show the trade-offs between different performance metrics and the relative contributions of each controller to those metrics. The various types of performance metrics often conflict, and the control architecture must be chosen to balance the differing types of requirements. Then, the tradespace is used to determine Pareto optimal design points and find traits of favorable architectures to provide a basis for further examination in subsequent design phases. Finally, this analysis only accounts for variations in the control systems, and not in any of the structural parameters. Chapter 6 will examine

the controller effects combined with structural parameters to help to determine the best overall architectures.

Chapter 6

Control-Structure Interactions and Architecture Selection

Chapter 5 discussed the effects of the control architecture on the performance metrics for a system with a given structural configuration. However, during the conceptual and preliminary design phases, many of those structural parameters may be negotiable and could be changed to provide better performance. Therefore, this chapter will examine key structural parameters and their effects on the performance and the control system design.

6.1 Tradespace Analysis

A tradespace is run to examine the effects of both the controls and the structure to determine a favorable overall design. The parameters varied in this tradespace are summarized in Table 6.1. Using a full factorial combination of these parameters results in nearly 3000 designs.

Each design in the tradespace has an associated overall performance, which is a combination of the optical performance, control, and programmatic metrics discussed in Section 2.6. A tradespace analysis is used to determine trends in the data. This analysis involves plotting two performance metrics against one another, and coloring the design points by an input parameter. These plots can show Pareto fronts, where

Table 6.1: Parameters Varied for the Tradespace Analysis

Parameter	**Type**	**Values**	**Units**
Mirror Type	Structural	Monolithic, Segmented	-
F#	Structural	1.0, 1.5, 2.0	-
Mirror Areal Density	Structural	5, 10, 15,	kg/m^2
Mirror Rib Aspect Ratio	Structural	2, 4, 6	-
ACS Bandwidth	Control	0.0125, 0.025, 0.125, 1.0	Hz
FSM Control	Control	Off, Low, High	-
WFE Piezo Control	Control	Off, Low, High	-
Petal Control	Control	Off, On	-

any increase in performance of one variable corresponds to an automatic decrease in the performance of the other, clearly indicating the design trade-offs. The colorings indicate the input parameters responsible for the associated performance, and show how to vary the input parameters to obtain the desired performance.

The first set of plots (Figure 6-1) shows the two optical performance metrics, line-of-sight jitter and wavefront error, colored by the four structural parameters. The best performing designs are closest the the lower, left corner. The data points in each plot are identical, only the color varies between plots. Figure 6-1(a) shows the designs colored by mirror type: monolithic or segmented. The monolithic performance is generally better for both optical performance metrics. This is due to the increased circumferential stiffness in the monolithic system because the mirror is one piece, whereas the segmented aperture connections allow much more flexibility. Figure 6-1(b) shows the designs differentiated by the areal density. As expected, the designs with higher areal density tend to perform slightly better because they are generally stiffer. However, there are extremely good performing low areal density systems as well. Not shown in this plot is the fact that some of these low areal density systems utilize a lot of control, causing them to perform on par with the higher areal density systems. Figure 6-1(c) shows the designs colored by $F\#$. The low $F\#$, highly compact, designs clearly dominate in both LOS jitter and WFE. Low $F\#$ implies a highly curved mirror; this causes the light to focus closer to the primary mirror, bringing the secondary mirror closer to the primary mirror, creating a shorter,

compact design. Also, the curved shape provides more stiffness and resistance to drum-like modes, which results in less vibration in the mirror and better performance. Finally, Figure 6-1(d) shows the designs colored by the aspect ratio of the ribs. A higher aspect ratio results in a thinner, deeper rib. This case does not have as strong of a separation of designs. However, for a given design, higher aspect ratio ribs improve performance. The explanation is two-fold. First, higher aspect ratio ribs increase the stiffness of the mirror. Second, the tall, thin ribs provide a larger moment arm for the piezo-electric actuator, giving the wavefront controller more authority.

It is also important to consider the controls in this analysis as well. The set of plots in Figure 6-2 shows the same LOS jitter versus WFE plots colored by each of the four control parameters. Figure 6-2(a) shows the designs colored by ACS bandwidth. There is really no visible gain in performance on this scale due to the ACS bandwidth. The ACS control only results in small changes in the optical performance which are not visible on this large scale. Figure 6-2(b) shows the designs colored by FSM bandwidth. The addition of FSM bandwidth significantly decreases the LOS jitter, as designed. When the FSM control bandwidth increases, each point moves directly down, improving LOS jitter. Figure 6-2(c) shows the designs colored by wavefront control effort. Here, the addition of wavefront control effort moves the designs down and left, indicating improved performance in both WFE and LOS jitter. However, the improvement in WFE is far more dramatic than the improvement in LOS jitter. Another interesting note is that the designs with higher initial WFE undergo significantly more improvement; the designs that have low initial WFE improve very little with the addition of the control. This is because the designs with the large initial WFE tend to be designs with low areal density. The low areal density designs give the piezo-electric actuators more control authority, and thus show the most improvement with the addition of control. Also, the LQG control design attempts to balance the control effort and performance, so designs that initially perform well do not warrant the additional control effort for small performance improvements. Finally, Figure 6-2(d) shows the designs colored by petal control, for only the segmented aperture systems. Again the petal control improves both LOS jitter and WFE, and the designs

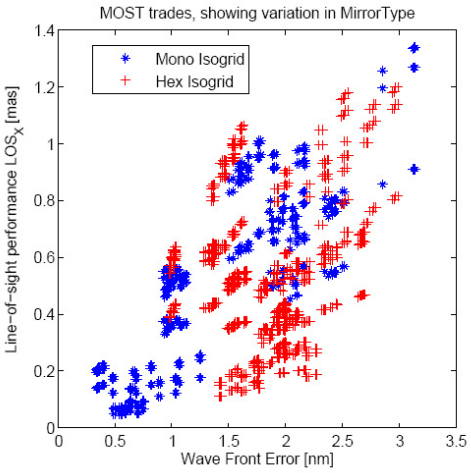

(a) Colored By Mirror Type

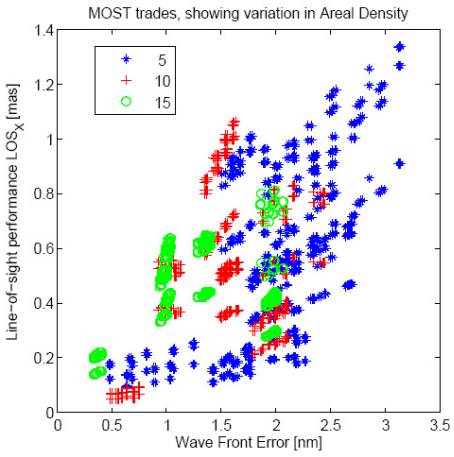

(b) Colored by Areal Density (kg/m^2)

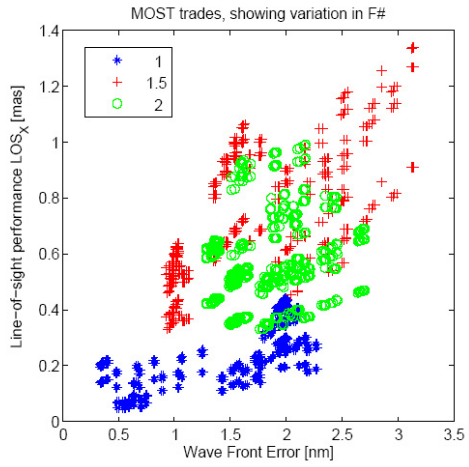

(c) Colored by $F\#$

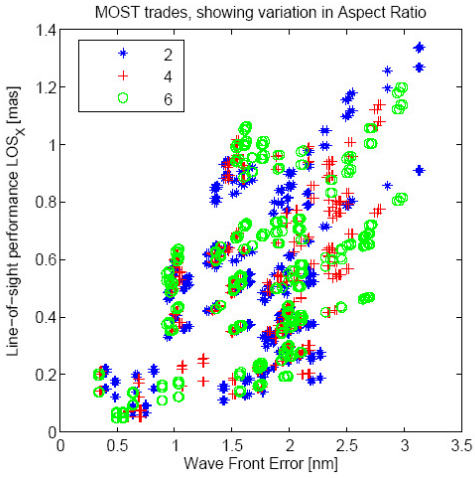

(d) Colored by Rib Aspect Ratio

Figure 6-1: Line-of-sight Jitter versus Wavefront Error Varying Structural Parameters

with the worst initial performance improve the most, again due to the lower areal density. The higher areal density designs have more massive petals, which are less susceptible to dynamic disturbances. Also, the higher areal density petals have higher inertias, and the cantilevered boundary control works best when the inertia of the petal is low.

The design traits that give the best optical performance are summarized in Table 6.2. The clearly dominating designs are all monolithic, $F\#$=1 systems. The other traits listed in the table provide improvement in WFE, but are not absolutely necessary for the best optically performing systems.

Table 6.2: Traits of systems with the best LOS jitter and WFE

Mirror Type:	Monolithic
$F\#$:	1.0
Aspect Ratio:	High
FSM Bandwidth:	High
Wavefront Control:	High
Petal Control:	On

These plots and analyses can provide powerful insights into the effect of the input parameters on the optical performance. However, an obvious disadvantage it that it is only possible to view two performance metrics at a time; the designs that seem best in terms of the two optical performance metrics may prove to have high sensitivities, costs, control efforts, settle times, or masses. It is possible to create plots of any combination of performance metrics colored by any input parameter. A series of plots will be shown to illustrate the effects of the the input parameters on the other performance metrics.

The WFE versus sensitivity is plotted in Figure 6-3. Figure 6-3(a) shows the sensitivity versus wavefront error colored by the amount of wavefront control. In general, the designs with high wavefront control have lower WFE, but higher sensitivity. This is consistent with the findings of Section 3.3.2. Figure 6-3(b) shows the sensitivity versus WFE colored by petal control for only the segmented aperture systems. The petal control brings down the WFE, but at the expense of sensitivity. Therefore, even

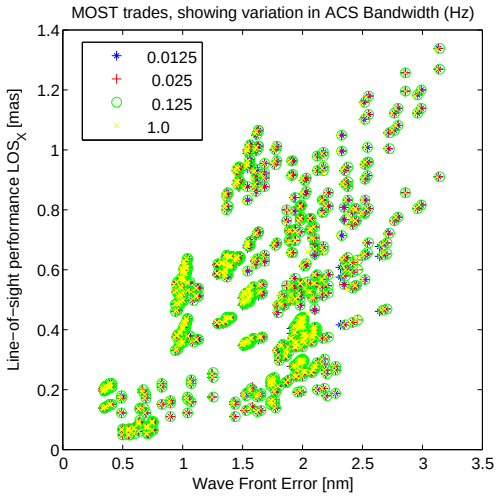

(a) Colored By ACS Bandwidth (Hz)

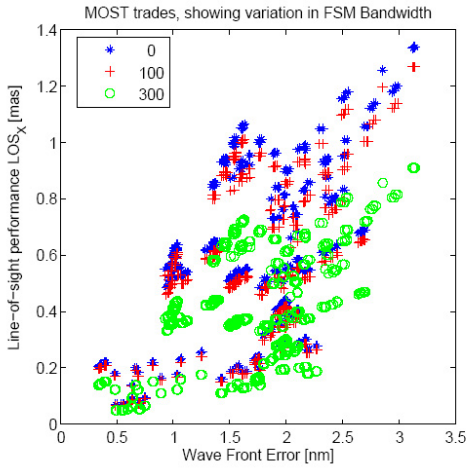

(b) Colored by FSM Bandwidth (Hz)

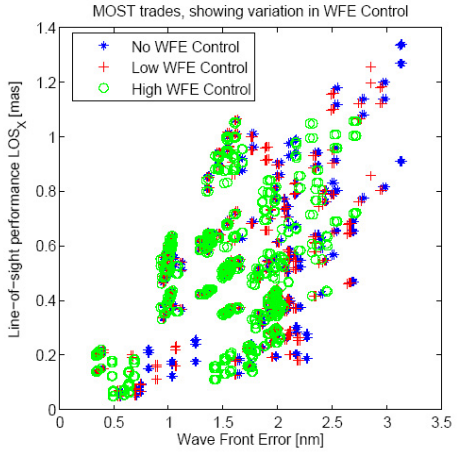

(c) Colored by Wavefront Control Penalty

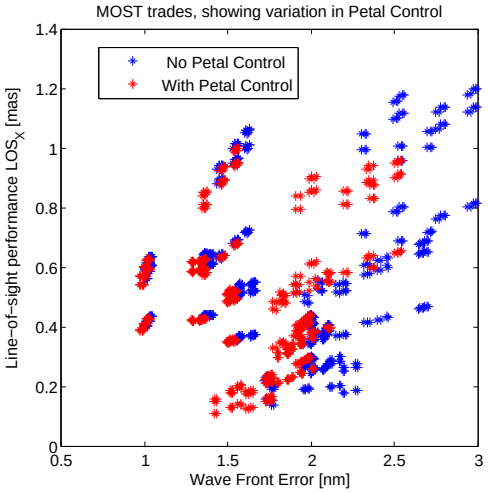

(d) Colored by Petal Control Bandwidth

Figure 6-2: Line-of-sight Jitter versus Wavefront Error

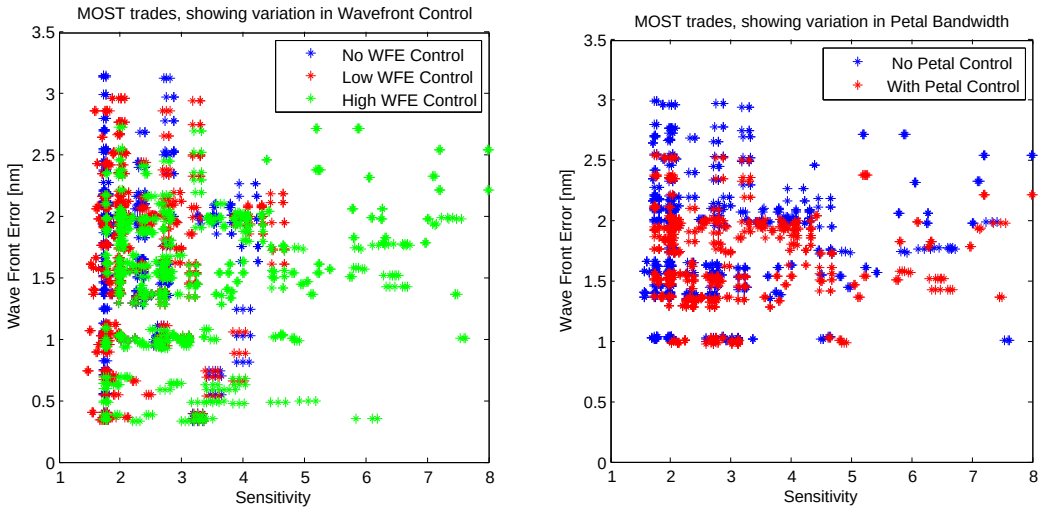

(a) Colored by Wavefront Control Penalty (b) Colored by Petal Control Bandwidth

Figure 6-3: Sensitivity Versus Wavefront Error

though both controllers tend to improve performance, high sensitivities may exclude those designs.

The design characteristics yielding Pareto performance in Figure 6-3 have the traits shown in Table 6.3. The best performing designs tend to be monolithic, low $F\#$, high rib aspect ratio systems. These systems have the best performance without any control, so the WFE and the sensitivities are both low. All values of wavefront and petal controls are found on the Pareto front since both controllers improve WFE but degrade sensitivity. Thus, the design decision would be made to meet the needs of the particular mission.

Table 6.3: Traits of systems with the best sensitivity and WFE

Mirror Type:	Monolithic
Areal Density:	High
$F\#$:	1.0
Aspect Ratio:	High

The LOS jitter versus sensitivity is shown in Figure 6-4. Figure 6-4(a) shows the designs colored by mirror type. Here, the moderately better LOS performance of

monolithic designs is again visible. Also, the designs with the highest sensitivities tend to be segmented aperture systems. However, there are both monolithic and segmented systems with low sensitivities; neither type of system always has lower sensitivity. But, with the application of large amounts of control, the monolithic systems tend to respond better, with smaller sensitivity increases. Figure 6-4(b) shows the same designs colored by areal density. Although higher areal densities are expected to have better optical performance, in this case, there is no obvious trend. The designs with the worst LOS jitter tend to have low areal densities, but the designs with good LOS jitter have a mixture of areal densities. This is because there is no indication of the control applied in each design, so some of the low areal density designs with a lot of control have similar LOS performance to the high areal density designs. There is a weak trend in the sensitivity; the lower areal density designs tend to have slightly higher sensitivities. However, the trend is not overwhelming, and many low areal density designs do have low sensitivities. Finally, Figure 6-4(c) shows the designs colored by FSM bandwidth. This plot explains many of the effects from Figures 6-4(a) and 6-4(b). The designs with lowest LOS jitter have high FSM bandwidth. Also, the FSM bandwidth increases the sensitivity, though only marginally, since the FSM bandwidths are all within the range of low sensitivities identified in Section 3.2.

The types of systems providing the best LOS jitter and sensitivity are summarized in Table 6.4. Again, low $F\#$, monolithic systems are best for these two metrics. However, there are multiple areal densities on the Pareto front. This is because the control can decrease the LOS jitter of the low areal density designs enough to make the performance comparable to that of the high areal density designs. Also, the Pareto systems have no petal control; the petal control contributes to a larger increase in sensitivity than improvement in LOS jitter.

Table 6.4: Traits of systems with the best LOS jitter and sensitivity

Mirror Type:	Monolithic
$F\#$:	1.0
FSM Bandwidth:	High
Petal Control:	Off

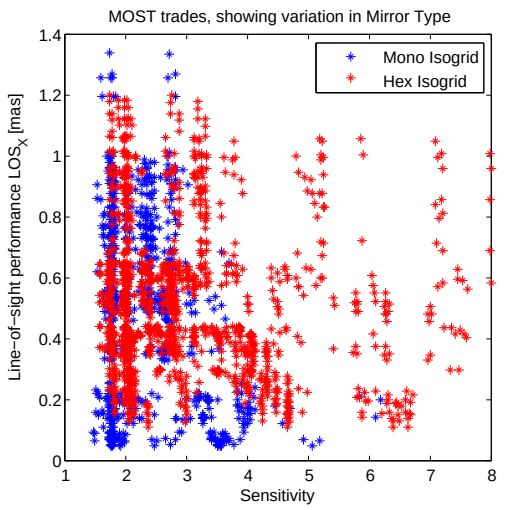

(a) Colored by Mirror Type

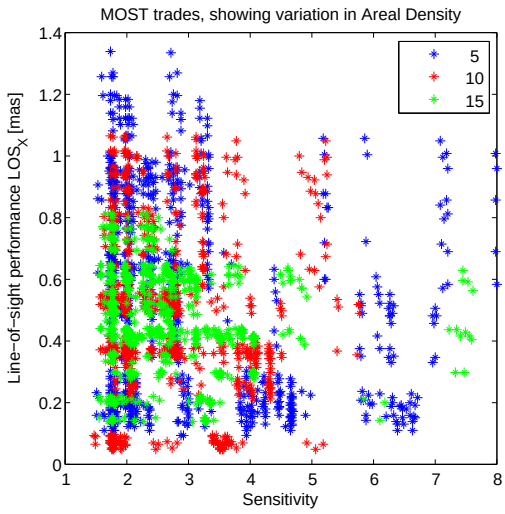

(b) Colored by Areal Density

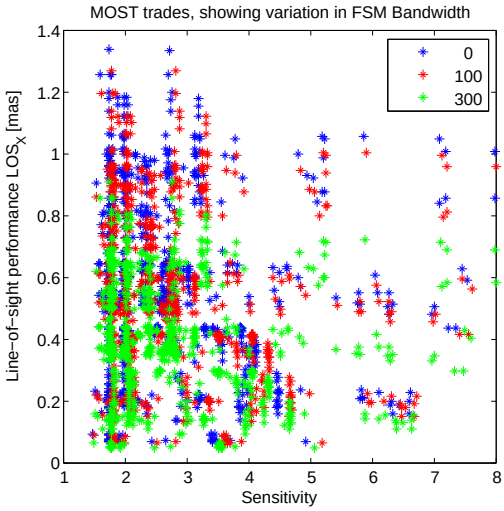

(c) Colored by FSM Bandwidth

Figure 6-4: Sensitivity Versus LOS Jitter

The settle time versus sensitivity is shown in Figure 6-5. The sensitivity and settle time do not appear to have a strong correlation; there are many sensitivities for a given settle time and vice versa. However, there is a small Pareto front in the lower left corner; the fastest settle times come with an increase in sensitivity. Figure 6-5(a) shows the designs colored by mirror type. In general, the mirror type is not a strong differentiator between designs. The monolithic designs tend to have slightly longer settle times, but the difference is minor. Figure 6-5(b) shows the designs colored by areal density. Again, the trends are subtle, but the low areal density designs tend to have slightly larger sensitivities and slightly longer settle times. Finally, Figure 6-5(c) shows the designs colored by ACS bandwidth. The ACS controller performs the slew, so the strong correlation between settle time and ACS bandwidth is expected. Larger ACS bandwidths involve shorter settle times. However, the highest ACS bandwidth (1 Hz) has sensitivities above the requirement. The three lower bandwidth values all contain a considerable spread in sensitivity, indicating that there is another control parameter that is primarily responsible for the high sensitivities in certain designs.

The traits of the sensitivity and settle time Pareto designs are summarized in Table 6.5. The designs all have ACS bandwidths of either 0.125 Hz or 1.0 Hz. The 0.125 Hz designs have longer settle times, but lower sensitivities, and the 1.0 Hz designs have shorter settle times, but higher sensitivities. There are designs of all other input parameter traits along this front.

Table 6.5: Traits of systems with the best sensitivity and settle time

Areal Density:	High
ACS Bandwidth:	Mid-High

The control effort and performance can also show interesting trade-offs. Figure 6-6 shows the control effort versus the WFE. There is no real Pareto front, so the characteristics of the low WFE and low control effort designs are sought. Figure 6-6(a) shows the designs colored by mirror type. As shown previously, the low WFE designs are all monolithic. Also, the correlation between mirror type and control effort is low. Some segmented systems do have higher control costs, but this is mainly due

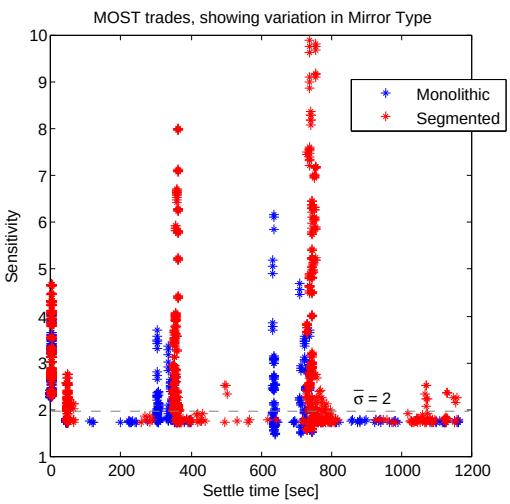

(a) Colored by Mirror Type

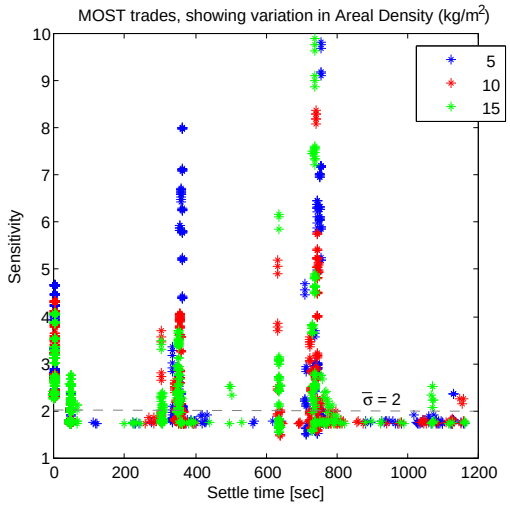

(b) Colored by Areal Density

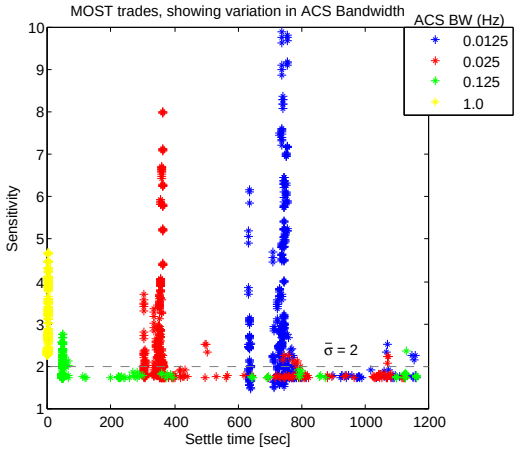

(c) Colored by FSM Bandwidth

Figure 6-5: Sensitivity Versus LOS Jitter

to the addition of the petal control, rather than more effort being applied by one of the control systems that exists in both the segmented and monolithic systems. Figure 6-6(b) shows the designs colored by areal density. As expected, the higher areal density designs generally have better wavefront error and lower control effort. Both outcomes are due to there being fewer vibrations that must be controlled. Figure 6-6(c) shows the designs colored by $F\#$. As seen previously, the low $F\#$ designs have significantly lower WFE. Also, the control effort is also lower for the more compact, low $F\#$ designs. Adding control always increases the control effort, so those plots are omitted.

The designs optimizing WFE and control effort are shown in Table 6.6. The best designs in terms of these two variables are clearly monolithic, high areal density, and low $F\#$. The controllers improve WFE performance, but cause proportional rises in control effort.

Table 6.6: Traits of systems with the best control effort and WFE

Mirror Type:	Monolithic
Areal Density:	High
$F\#$:	1.0

Another interesting interaction is between the effectiveness of the control systems and the structural parameters. Designs that have high initial WFE end up with more improvement due to the wavefront control. Figures 6-7 and 6-8 show the change in WFE with the addition of wavefront control for different structural configurations. Figure 6-7 shows the monolithic case. There are three points for each design number: one with no wavefront control, one with low wavefront control, and one with high wavefront control. All other input parameters for a given design number are the same. The three large groups are defined by the three areal density values, and the smaller ellipses enclose the different $F\#$ designs. The low areal density (left) designs have significantly more improvement in WFE than the high areal density points, due to the addition of wavefront control. This occurs because there is more control authority in the lower areal density designs since there is less mass and stiffness

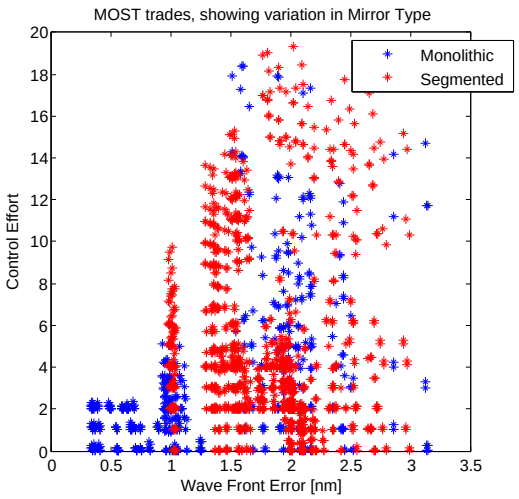

(a) Colored by Mirror Type

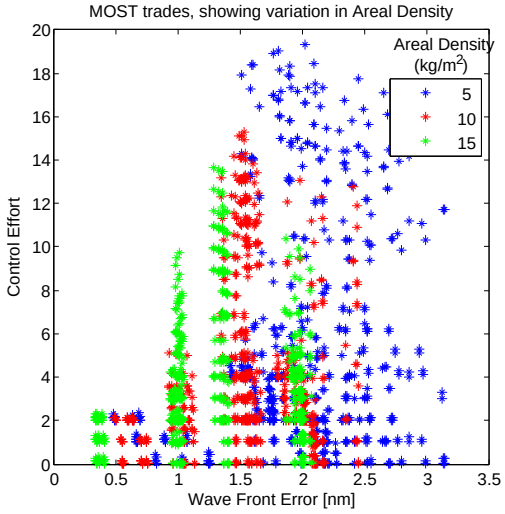

(b) Colored by Areal Density

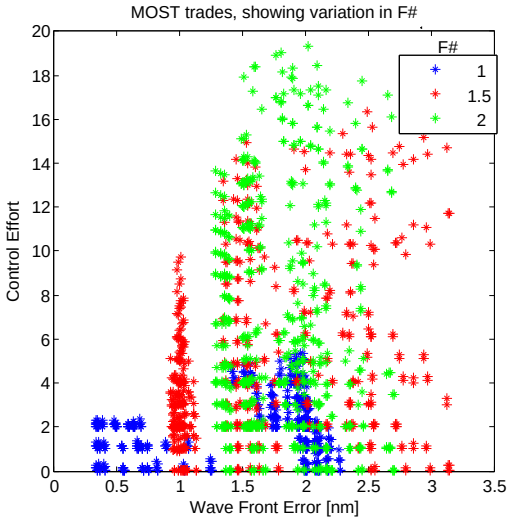

(c) Colored by $F\#$

Figure 6-6: Control Effort Versus WFE

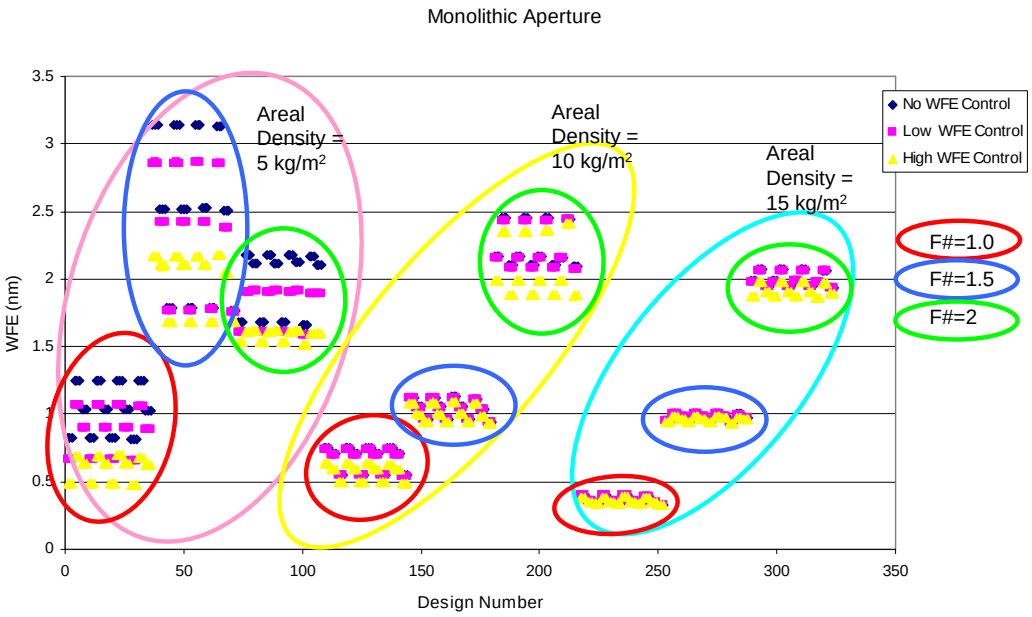

Figure 6-7: Wavefront Error Performance for a Monolithic Aperture System

that must be controlled. Also, the wavefront errors tend to be initially lower (with no wavefront control) in the higher areal density designs. The LQG controller is designed to balance the state error and the amount of control applied; the higher areal density designs have both a lower initial state error and necessitate more control to decrease that error. Therefore, since the controller attempts to balance the control effort and the state error, the lower areal density designs (that have more initial error and that take less effort to fix that error) tend to undergo a greater performance change.

The lower $F\#$ designs tend to have better performance, but $F\#$ does not influence the amount of improvement due to the addition of wavefront control. The variation seems to be more due to the initial wavefront error, rather than the $F\#$. The other variations are due to the rib aspect ratio and ACS bandwidth, but these effects are much less significant than the effects due to either areal density or $F\#$.

Figure 6-8 shows a similar plot for the segmented aperture system. However, there are twice as many designs due to the presence of the petal control. The left half of the plot shows the designs without petal control, and the right side shows the same designs with petal control. This plot does not have distinctions as clear as the monolithic case. However, some similar trends are still visible. The low areal density

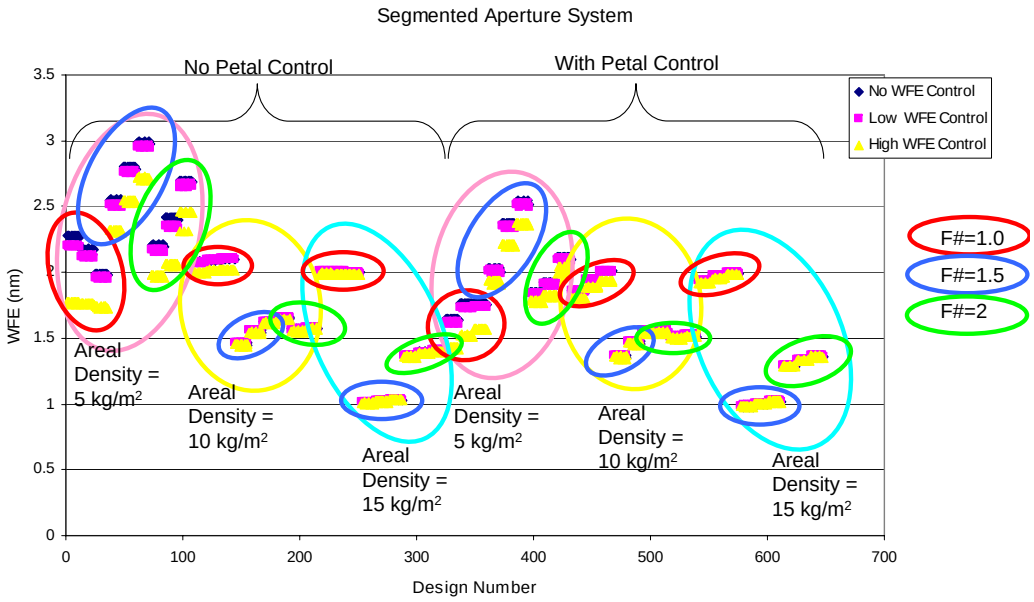

Figure 6-8: Wavefront Error Performance for a Segmented Aperture System

designs still undergo the most WFE improvement. However, the trend in WFE due to the $F\#$ of the system is no longer present. The designs on the right half of the plot have lower WFE than those on the left, indicating that the petal control is also improving performance, as desired.

In addition to examining the optical performance and control metrics, the OTA cost and mass are no longer constant because the structural parameters are changing. Figure 6-9 shows the mass versus the wavefront error. Figure 6-9(a), which is colored by areal density, shows that, as expected, the mass varies significantly with the areal density. Also, there is a trade-off between mass and wavefront error since lowest mass designs tend to have higher WFE. Figure 6-9(b) shows the same designs colored by wavefront control effort. The wavefront control does not affect the mass of the system, but it does account for the vertical spread in the designs. The various points appear in vertical lines. Each of these lines has a design with no wavefront control on the top (high WFE), and high wavefront control on the bottom (low WFE). This is similar to the vertical design lines in Figures 6-7 and 6-8.

Table 6.7 summarizes the traits of the mass versus WFE Pareto designs in Figure 6-9. The best optical performance is obtained with monolithic, low $F\#$ systems.

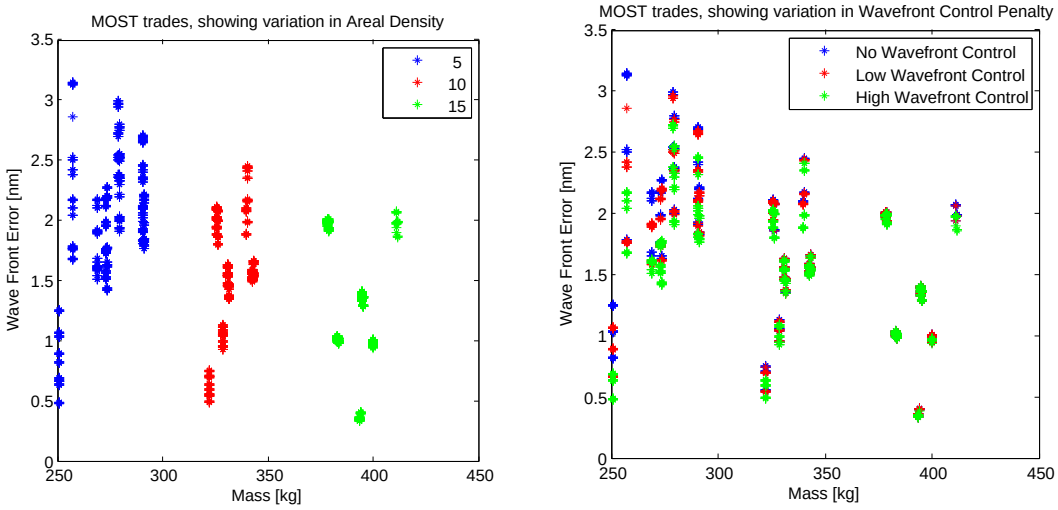

(a) Colored by Areal Density

(b) Colored by Wavefront Control

Figure 6-9: Mass Versus Wavefront Error

The low $F\#$ designs have lower mass because of the compactness of the design. As mentioned previously, the areal density can be used to move along the Pareto front, as lower mass designs tend to have higher WFE and vice versa. The wavefront control and petal control both improve the WFE without a direct mass penalty (not considering control support avionics).

Table 6.7: Traits of systems with the best mass and WFE

Mirror Type:	Monolithic
$F\#$:	1.0
Wavefront Control:	High
Petal Control:	On

Figure 6-10 shows the relative OTA cost versus the WFE differentiated by $F\#$ and mirror type. Here, high $F\#$, segmented aperture designs have the lowest cost. This is because it is cheaper to manufacture multiple, smaller mirrors than one very large mirror. Also, the mirrors with higher $F\#$s have higher sagitta (curvature), which is also more expensive.

The design traits of the best performing systems in Figure 6-10 are summarized

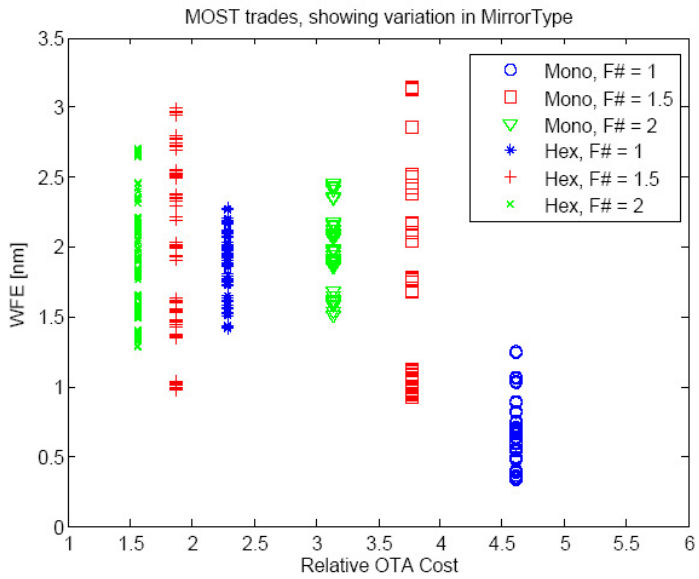

Figure 6-10: Cost Versus WFE Distinguished by Mirror Type and $F\#$

in Table 6.8. As mentioned above, the segmented, low $F\#$ systems have significantly lower OTA cost, and the high areal density designs have low WFE. Also, the petal control and wavefront control are desirable since they reduce the WFE.

Table 6.8: Traits of systems with the best OTA cost and WFE

Mirror Type:	Segmented
$F\#$:	Low
Areal Density:	High
Wavefront Control:	High
Petal Control:	On

The traits of the lowest OTA cost designs conflict with results of Figure 6-1. Here, high $F\#$, segmented systems are best, while Figure 6-1 showed that monolithic, low $F\#$ designs give superior optical performance. These types of conflicting conclusions suggest that the performance metrics must be examined in an integrated fashion to obtain an accurate depiction of that design.

6.2 Multi-Dimensional Performance Analysis

It is important to look at all metrics before any design decisions are made. Ideally, the designs would be plotted on a n-dimensional surface, where n is the number of performance metrics. In this case, there are seven metrics; making this visualization impossible. The Pareto surface designs can be computed, but they cannot be displayed.

One strategy for determining favorable families of designs is to first apply the requirements from Section 2.6. Those requirements are summarized in Table 6.9. The LOS jitter, WFE, and sensitivity requirements were all calculated in Chapter 2. The settle time requirement is added to eliminate designs that do not settle after a slew. Any designs that do not meet these four requirements are removed from the set of valid designs.

Table 6.9: Summary of Requirements

LOS Jitter	< 1.6 mas
WFE	< 1.0 nm
Sensitivity	< 2.0
Settle Time	< 400 s

Then Pareto designs can be computed by finding all of the designs where an improvement in one performance metric necessitates a degradation in the performance of another metric. If it is assumed that any design that meets the four requirements is acceptable. Therefore, those metrics are excluded, and this reduces to a three dimensional Pareto surface. This surface is still difficult to visualize, so the traits of the designs on the surface will be presented as an alternative.

For this tradespace, 235 of the original 2916 designs meet all four requirements. Of the 235 valid designs, 157 designs are non-dominated and approximate the Pareto surface. The traits of the Pareto surface designs are summarized in Table 6.10.

A number of observations can be made from this list of designs. First, as expected, the number of monolithic systems on the Pareto surface far exceeds the number of segmented systems. This is partially due to the fact that far few segmented systems

Table 6.10: Traits of Designs on the Pareto Surface

Parameter	**Units**	**Design Traits-# of Designs**
Mirror Type	-	Monolithic: 110, Segmented: 47
Areal Density	kg/m^2	5: 36, 10: 72, 15: 49
$F\#$	-	1: 77, 1.5: 80, 2: 0
Rib Aspect Ratio	-	2: 43, 4: 56, 6: 58
ACS Bandwidth	Hz	0.0125: 0, 0.025: 55, 0.125: 102, 1: 0
FSM Control	-	Off: 59, Low: 49, High: 49
Wavefront Control	-	Off: 43, Low: 70, High: 44
Petal Control	-	Off: 149, On: 8

meet the WFE requirement. There are designs at every areal density, but the majority of Pareto designs have an areal density of ten kg/m^2. This mid-range areal density requires less control effort than the low areal density cases. Also, these designs have lower mass than the high areal density systems. All systems have $F\#$s equal to either 1.0 or 1.5. The systems with $F\#$=1.0 have lower control costs and lower masses, while the systems with $F\# = 1.5$ have lower OTA costs. The rib aspect ratios are about equally divided between the three options.

The ACS bandwidths are all equal to either 0.025 Hz or 0.125 Hz. The lower ACS bandwidth designs did not meet the settle time requirements, and the higher bandwidth designs did not meet the sensitivity requirements. The FSM control is about equally split between the three values, indicating that it does not have a strong effect on the Pareto surface. Most designs have a low level of wavefront control. The low wavefront control allows low areal density (low mass) designs to meet the requirements, but does not have exceedingly high control effort. Finally, very few of the designs incorporate petal control. However, since the monolithic systems do not have an option for petal control, close to 20% of the designs with the option for petal control utilize it. The petal control can decrease the WFE, but for any design that can meet the WFE requirement without the petal control, it purely adds additional control effort.

The Pareto surface gives a preliminary idea of which types of designs may prove favorable. However, if the requirements were relaxed, or if performance margin were

desired, these designs could change quite dramatically. Relaxation of the requirements, particularly the wavefront error requirement, would allow many more segmented, low-cost, low-mass designs to become viable options. In many cases, these designs would lie on the Pareto front. Also, if all seven metrics were included in the Pareto front, then designs with more control would appear on the Pareto front more often. The control tends to improve optical performance, but degrade sensitivity and control effort, so if the goal is to simply meet, and not exceed, optical performance requirements, any control over what is necessary to meet the requirements degrades the set of performance metrics under consideration.

6.3 Summary

When designing the control architecture, it is important to remember that the control systems do not act independently; the performance of the control systems change with different structural configurations. Therefore, an ideal design decision would be made by considering both the structural and control parameters together to determine the best overall design. As expected, high areal density designs give good initial performance. However, the wavefront and petal control are more effective on low areal density designs. For the wavefront control, the low areal density gives the actuators more control authority for less control effort, while in the petal control, the lower mass and inertias of the petals makes it easier for the actuator to control. In the monolithic systems, low $F\#$ designs were clearly superior in terms of optical performance, but this trend disappeared in the segmented case. Also, low $F\#$ designs have higher mirror manufacturing costs. The rib aspect ratio affects the moment-arm of the piezo-electrics, introducing the trade between structural integrity of the ribs versus more control authority. Each of these interactions are important and should be taken into account together to obtain the best design.

Also, each of the performance metrics are optimized by utilizing a certain set of input design parameters. The traits that best optimize each performance metric are summarized below.

- Line-of-Sight Jitter:
  - Monolithic aperture
  - Low $F\#$
  - High FSM bandwidth
- Wavefront Error
  - Monolithic aperture
  - Low $F\#$
  - High aspect ratio ribs
  - High wavefront control
  - High petal control
- Settle Time
  - High ACS bandwidth
- OTA Cost
  - Segmented aperture
  - High $F\#$
- Mass
  - Low areal density
  - Low $F\#$
- Sensitivity
  - Low control bandwidths
- Control Effort
  - Low control bandwidths

Many of the desired traits for one performance metric conflict with the traits of another metric. Therefore, the needs of the particular mission need to be known to make any definite conclusions on favorable architectures. However, some families of favorable designs can be identified to meet the needs of some theoretical missions.

- Low cost, deployable system
  - A low cost, deployable system would necessarily use a segmented aperture. An extremely low-cost design would also use a high F# and low areal density (to minimize OTA and launch costs). Since these types of systems tend to have relatively poor optical performance, a lot of control would be utilized. To keep the sensitivity under two, there would be a combination of mid-range FSM, petal, and wavefront control.
- High optical performance
  - An extremely high performing system would likely use a monolithic aperture with low $F\#$. The areal density would be high to minimize vibrations, and controls would be utilized to the furthest extent possible while maintaining stability margin.
- Low Complexity
  - A system with very little complexity would use as little control as possible to still meet the requirements, as the controls naturally introduce complexity into the system. Also, a monolithic aperture is likely, as deployability and alignment can be complicated.

Using the various design traits, the performance can largely be tailored to the needs of a particular mission. However, those needs must be known before the design can be chosen and refined. Also, there is clearly no "utopia" design that optimizes all performance metrics; there are always trade-offs to be made. The addition of control improves performance, but introduces complexity and decreases stability. Deployable, segmented mirrors allow for larger aperture systems, but the optical performance is

slightly degraded and control needs to be introduced to compensate for this loss. Low areal density can minimize launch costs, but again, more control needs to be introduced to meet the optical performance requirements. Therefore, there are many families of potentially favorable architectures, depending on specific mission goals.

Chapter 7

Conclusions

This Chapter contains a thesis summary with overall conclusions and contributions. It also includes recommendations for future work in this area.

7.1 Thesis Summary

Future space telescopes require new technologies and innovativeness to meet both the tight performance as well as the programmatic requirements. One way to effectively utilize lightweight systems is by including control. However, in future systems, the effects of the controls, as well as the interactions between layered control systems, may become non-intuitive, as the new architectures become less based on heritage designs. Therefore, it is necessary to examine those effects in order to create a predictable, high-performing system. Also, control should not be applied indiscriminately, and the cost to include control must be considered. As the areal density decreases, the cost due to mass decreases, but the cost due to control increases. Therefore, the optimal point, where the sum of these two costs is minimized, is the ideal amount of control for a given system.

The MOST project is a parametric, integrated model that includes finite element modeling, normal modes analysis, integrated state-space modeling, and a variety of analyses techniques such as a dynamic disturbance analysis. This process provides quantitative analysis of conflicting types of performance requirements. The

performance metrics include optical performance, quantified by line-of-sight jitter and wavefront error, control performance, determined by the stability margin and control effort, and programmatic metrics, including mass, OTA cost, and out-of-operations time due to slewing the system. The entire process is completely automated, and almost any parameter in the system can be easily changed to create a completely different architecture. This allows examination of large tradespaces to quantitatively determine the trade-offs between performance metrics, and determine which types of architectures offer the most promise.

The MOST framework can be used to determine the effects of multiple control systems in order to create an architecture that performs well over all performance metrics. Specifically, the control can be designed to balance the control metrics and the optical performance metrics to identify designs that efficiently balance both types of metrics. It is desired that the sensitivity remain below two, the LOS jitter remain less than 1.6 mas, and the WFE remain less than 1.0 nm, while minimizing the other four performance metrics (settle time, control effort, mass and OTA cost). These conflicting desires require careful consideration and balance.

The MOST system contains four control systems: attitude control system, fast steering mirror control, wavefront control, and petal control. Each of these controllers is designed to improve the performance of a specific metric. The ACS system improves settle time, the FSM control improves LOS jitter, and the wavefront control and petal control both improve WFE. While, each controller improves the performance of the target metric, they also increase the sensitivity and control effort. Additionally, when implemented together, they will each affect other un-targeted performance metrics, thus motivating the need to examine all control systems together and across all performance metrics.

In addition to the typical optical performance metrics, a slew and settle analysis is also included to quantify the amount of time the system is non-operational due to the slew maneuver. There are many factors to help minimize the non-operational amount of time, including slew speed, torque profiles, and controller bandwidths. For a given system, there is an optimal slewing speed to minimize the slew and settle

time, and this can be determined to provide the system with efficient mission operation characteristics. Also, higher ACS bandwidth produces the best settle times, as long as the controller frequency is not near the frequency of a structural mode. Unfortunately, this performance comes at the expense of stability margin. There are also feed-forward techniques that minimize vibrations with a smaller maximum torque, which involves smaller reaction wheels, and thus smaller disturbances. However, this technique involves an optimization, which outweighs is benefits during the tradespace analysis. This technique could be implemented to improve settle time performance once an architecture is selected.

The four control systems were also examined in conjunction with one another for a monolithic and segmented aperture system. In many cases, such as the ACS and FSM controllers, the performance of two control systems together acted as expected, with trends similar to those found when the control systems were analyzed separately. However, in other cases, such as the interactions between the wavefront controller and the ACS controller, more complex relations were discovered resulting from the interactions of the control systems.

Next, all control systems were combined into a tradespace to show the relative contributions of control parameters on the performance metrics. This analysis also revealed trade-offs between different performance metrics. The Pareto fronts, where the performance of one metric must be sacrificed to gain any performance in the other metric, were identified and used to show the trade-offs between cost and performance. This tradespace analysis was used to determine traits of potentially favorable control architectures for a given structural configuration, depending on requirement values and performance priorities.

The monolithic system has very good performance when considering the optical and control performance metrics. Many designs met all requirements, and, depending on precise goals of the mission, there are many extremely low areal density, monolithic systems that could be suitable. The optical performance for the segmented systems is not as good as the monolithic systems. In the extremely low areal density cases, the 1.0 nm WFE requirement proved difficult to achieve. However, segmented systems

are easier to deploy and manufacture, making them viable options.

Finally, the control system and structural parameters were varied together. This large tradespace analysis revealed key interactions between the control and the structure, including the dependency of the effectiveness of the wavefront controller on the primary mirror areal density. Low areal density mirrors undergo far more improvement in WFE due to the wavefront control than higher areal density mirrors. This improvement can allow lower areal density designs to have better closed loop performance than the higher areal density designs.

The metrics were plotted two at a time to reveal the various Pareto fronts in the data. This analysis clearly showed trade-offs between performance metrics, and also revealed which input parameters are responsible for those trade-offs. It is also used to identify design traits that give good performance. However, conflicting results can be obtained when looking at different sets of performance metrics. Ideally, all performance metrics would be examined together, but the seven-dimensional space cannot be visualized. Therefore, requirement values were used to eliminate designs from the tradespace, and a Pareto surface of the remaining metrics (without hard requirements) was determined. Finally, the characteristic traits that optimize the performance of each individual performance metric were determined, along with a few families of potentially favorable architectures.

It is not possible to determine a single "best" architecture for future systems. The ideal architecture depends on the specific goals of that mission. However, the research in this thesis outlines a framework for determining a favorable set of designs, given requirements and priorities. Additionally, for a given structural configuration, it is still possible to optimize the control systems to obtain the best combination of controllers that balances performance improvement and control cost. This framework could also be easily adapted to include additional controllers, analysis routines, or performance metrics if those became available or necessary, making it a powerful methodology for the conceptual design phase.

7.2 Contributions

The major contributions of this thesis are summarized below.

- Incorporated the design and analyses of multiple control systems into an integrated model to facilitate large tradespace analyses.
- Quantitatively determined the benefits and costs of utilizing highly controlled, lightweight telescope systems.
- Incorporated and analyzed various slewing strategies to minimize the amount of time a system is out of operations due to a slew.
- Analyzed the effects of layered control systems to determine potential adverse interactions, including loss of stability margin.
- Developed a framework for choosing a control architecture for a given structural configuration.
- Examined the interactions between structural and control parameters to determine families of favorable architectures based on the needs of the mission.

7.3 Future Work

This thesis has provided a basis for control architecture selection for space telescopes during the conceptual design phase. However, there are a number or areas where more work could be done.

First, additional control algorithms could be implemented. Each sensor/actuator pair has been implemented with a single control algorithm. Other control algorithms, particularly robust controls, could be examined to reduce sensitivity for a given level of performance. Other techniques may provide more performance improvement than has already been realized. Additionally, the petal and wavefront controllers could be combined into a single controller that accounts for the tip, tilt, and higher order Zernikes of each petal of the segmented aperture system. Combining these two types

of controllers may prove effective for reducing the overall wavefront error by having the controllers work together, instead of separately.

Also, additional performance metrics could be added, and the current performance metrics could be updated. Particularly, the control effort metric could be turned into a power consumption with appropriate weightings between the mean squared control channel output and power consumption. Then, the solar panels could be sized based on the amount of power required, capturing that additional cost. Another extension would be to determine an overall "cost" for the control. This cost would be a function of the control effort, sensitivity, bandwidth, and number of channels. Also, the optical performance metrics are currently based on dynamics, and could be extended to include additional optical and ray-tracing techniques using Zemax of Code-V.

Optimization routines could also be included to search over large tradespaces. By utilizing an optimization algorithm instead of a full-factorial search, more input parameters could be varied in finding the best architectures. This would allow for more variation in the architectures, and an actual optimization of the control system for that architecture.

These are just a few of the ways in which the research in this thesis could be extended. There are many possibilities for the design of future telescope systems. The framework presented provides a way to analyze the interactions between the structure and multiple control systems, while considering different types of performance metrics. It also sheds light onto some of the more complex interactions, and specific trade-offs involved in the telescope control architecture selection.

Bibliography

[1] Ball Aerospace. Fast steering mirrors. Technical report, 2006. URL: <http://www.ballaerospace.com/fsm.html>.

[2] N. M. Alexandrov, R. M. Lewis, C. R. Gumbert, L. L. Green, and P. A. Newman. Optimization with variable-fidelity models applied to wing design. In 38^{th} *Aerospace Sciences Meeting & Exhibit*, Reno, NV, January 10-13, 2000. AIAA 2000-0841.

[3] George Angeli and Brooke Gregory. Linear optical model for large ground based telescope. In *Proceedings of the SPIE, Volume 5178*, pages 64–73. SPIE, 2004.

[4] George Angeli, Anna Segurson, Robert Upton, Brooke Gregory, and Myung Cho. Integrated modeling tools for large ground based optical telescopes. In *Proceedings of the SPIE, Volume 5178*, pages 49–63. SPIE, 2004.

[5] George Z. Angeli, Myung K. Cho, and Mark S. Whorton. Active optics and control architecture for a giant segmented mirror telescope. In *Proceedings of the SPIE, Volume 4840*, pages 129–139. SPIE, 2003.

[6] Ruth Azor. Momentum management and torque distribution in a satellite with reaction wheels. In *The 33rd Israel Annual Conference on Aviation and Astronautics*, pages 339–347, Israel, 1993. Israel Society of Aeronautics and Astronautics.

[7] S. P. Bhat and D. K. Miu. Precise point-to-point positioning control of flexible structures. *ASME Journal of Dynamic Systems, Measurement, and Control*, 112(4):667–674, 1990.

[8] Carl Blaurock. Disturbance-optics-controls-structures (docs). Technical report, Nightsky Systems, Inc., 2006. URL: <http://www.nightsky-systems.com/pdf/DOCS_Intro.pdf>.

[9] Mark E. Botkin. Structural optimization of automotive body components based upon parametric solid modeling. In 8^{th} *AIAA/USAF/NASA/ISSMO Symposium on Multidisciplinary Analysis and Optimization*, Long Beach, CA, Sept. 6-8, 2000. AIAA-2000-4707.

[10] R.G. Brown and P.Y.C. Hwang. *Introduction to Random Signals and Applied Kalman Filtering*. John Wiley & Sons, New York, 3^{rd} edition, 1997.

[11] Mark Campbell. *Uncertainty Modeling for Structural Control Analysis and Synthesis*. PhD thesis, Massachusetts Institute of Technology, Cambridge, MA, 1996.

[12] Soon-Jo Chung, David W. Miller, and Olivier L. deWeck. Argos testbed: study of multidisciplinary challenges of future spaceborne interferometric arrays. *Opt. Eng.*, 43(9):2156–2167, September 2004.

[13] Ed Crawley, Mark Campbell, and Steve Hall. *High Performance Structures: Dynamics and Control*. Cambridge University Press - Draft, Cambridge, MA, 1998.

[14] John Van de Vegte. *Feedback Control Systems*. Prentice Hall, Englewood Cliffs, NJ, 3^{rd} edition, 1994.

[15] Olivier L. de Weck and David W. Miller. Integrated modeling and dynamics simulation for the next generation space telescope. Master's thesis, Massachusetts Institute of Technology, Cambridge, MA, June 1999.

[16] George Z. Angeli et. all. Modeling tools to estimate the performance of the thirty meter telescope: an integrated approach. In *Proceedings of the SPIE, Volume 5497*, pages 237–250. SPIE, 2004.

[17] J. Johnston et. all. Integrated modeling activities for the james webb space telescope: Structural-thermal-optical analysis. In *Proceedings of the SPIE, Volume 5487*, pages 600–610. SPIE, 2004.

[18] J. L. Fanson and T. K. Caughey. Positive position feedback control for large space structures. *AIAA Journal*, 28(4):717–724, 1990.

[19] P. A. Fenyes. Multidisciplinary design and optimization of automotive structures - a parametric approach. In 8^{th} *AIAA/USAF/NASA/ISSMO Symposium on Multidisciplinary Analysis and Optimization*, Long Beach, CA, Sept. 6-8, 2000. AIAA-2000-4706.

[20] R. H. Freemand and J. E. Pearson. Deformable mirrors for all seasons and reasons. *Applied Optics*, 21:580–588, 1982.

[21] Simon O. Grocott. Comparison of control techniques for robust performance on uncertain structural systems. Master's thesis, Massachusetts Institute of Technology, Cambridge, MA, February 1994.

[22] Robert L. Grogan and Robert A. Laskin. On multidisciplinary modeling of the space interferometry mission. In *Proceedings of the Amerian Controls Conference*, pages 1558–1562. AACC, 1998.

[23] Homero L. Gutierrez and David W. Miller. *Performance Assessment and Enhancement of Precision Controlled Structures During Conceptual Design*. PhD thesis, Massachusetts Institute of Technology, Cambridge, MA, February 1999.

[24] T. Hyde, K. Ha, J. Johnston, J. Howard, and G. Mosier. Integrated modeling activities of the james webb space telescope: Optical jitter analysis. In *Proceedings of the SPIE, Volume 5487*, pages 588–599. SPIE, 2004.

[25] Physik Instruments. Active optics and piezo-driven high-dynamics steering mirrors. Technical report, 2007. URL: <http://www.physikinstrumente.com/en/products/steering_mirror/index.php>.

[26] H. Irschik. A review of static and dynamic shape control of structures by piezoelectric actuation. *Engineering Structures*, 24:5–11, 2005.

[27] Robert N. Jacques and David W. Miller. An apporach to the preliminary design of controlled structures. Master's thesis, Massachusetts Institute of Technology, Cambridge, MA, February 1991.

[28] Cyrus D. Jilla and David W. Miller. *A Multiobjective, Multidisciplinary Design Optimization Methodology for the Conceptual Design of Distributed Satellite Systems*. PhD thesis, Massachusetts Institute of Technology, Cambridge, MA, May 2002.

[29] E. O. Jordan, A. Stewart, S. A. Uebelhart, D. Howell, and D. W. Miller. Parametric modeling of space telescope architectures. In *2006 SPIE Astronomical Telescopes and Instrumentation Conference*, Orlando, FL, May 24-31, 2006.

[30] Arthur E. Bryson Jr. and Yu Chi Ho. *Applied Optimal Control*. Hemisphere Publishing, USA, 1975.

[31] Huibert Kwakernaak and Raphael Sivan. *Linear Optimal Control Systems*. John Wiley & Sons, New York, 1972.

[32] Wiley J. Larson and James R. Wertz. *Space Mission Analysis and Design*. Microcosm, Inc, Torrance, CA, Kluwer Academic Publishers, Boston, 3^{rd} edition, 1992.

[33] F. F. Lillie and A. J. Bronowicki. Adaptation in space telescopes. In 45^{th} *AIAA/ASME/ASCE/AHS/ASC Structures, Structural Dynamics & Materials Conference*, Palm Springs, CA, April 19-22, 2004. AIAA 2004-2064.

[34] Kuo-Chia (Alice) Liu and David W. Miller. *Stochastic Performance Analysis and Staged Control System Designs for Space Based Interferometers*. PhD thesis, Massachusetts Institute of Technology, Cambridge, MA, May 2003.

[35] D. M. LoBoscoa, C. Blaurock, S.Chung, and D. W. Miller. Integrated modeling of optical performance for the terrestrial planet finder structurally connected interferometer. In *Proceedings of the SPIE*. SPIE, 2004.

[36] Douglas G. MacMynowski, George Z. Angeli, Konstantinos Vogiatzis, Joeleff Fitzsimmons, and Steve Padin. Parametric modeling and control of telescope wind-induced vibration. In *Proceedings of the SPIE, Volume 5497*, pages 266–277. SPIE, 2004.

[37] Gregory J. W. Mallory and David W. Miller. *Developement and Experimental Validation of Direct Controller Tuning for Spaceborne Telescopes*. PhD thesis, Massachusetts Institute of Technology, Cambridge, MA, 2000.

[38] Terry S. Mast and Jerry E. Nelson. Segmented mirror control system harware for celt. In *Proceedings of the SPIE - Active Hardware*. SPIE, 2000.

[39] Brett P. Masters and Edward F. Crawley. *Evolutionary Design of Controlled Structures*. PhD thesis, Massachusetts Institute of Technology, Cambridge, MA, June 1997.

[40] Rebecca A. Masterson. Development and validation of empirical and analytical reaction wheel disturbance models. Master's thesis, Massachusetts Institute of Technology, Cambridge, MA, June 1999.

[41] Stephen M. Merkowitz. The lisa integrated model. *Classical and Quantum Gravity*, 20:255–260, 2003.

[42] D. W. Miller, E. F. Crawley, J. P. How, K. Liu, M. E. Campbell, S. C. O. Grocott, R. M. Glaese, and T. D. Tuttle. The middeck active control experiment (mace): Summary report. Report 7-96, MIT Space Engineering Research Center, 1996.

[43] David W. Miller, Olivier L. deWeck, Scott A. Uebelhart, Robert Grogan, and Ipek Basdogan. Integrated dynamics and controls modeling for the space interferometry mission (sim). In *2001 IEEE Aerospace Conference*, Big Sky, Montana, March 10-17, 2001. IEEE.

[44] C. Perrygo and R. Burg. Hand calculation of line-of-sight sensitivity to optics displacements. Technical report, Northrop Grumman Space Technology, 1999.

[45] M. D. Sensmeier, B. T. Stewart, and J. A. Samareh. Rapid generation of aircraft structural topologies for multidisciplinary optimization and weight estimation. In 47^{th} *AIAA/ASME/ASCE/AHS/ASC Structures, Structural Dynamics & Materials Conference*, Newport, RI, May 1-4, 2006. AIAA 2006-1981.

[46] N. C. Singer and W. P. Seering. Preshaping command inputs to reduce system vibration. *ASME Journal of Dynamic Systems, Measurement, and Control*, 112:76–82, 1990.

[47] Sigurd Skogestad and Ian Postlethwaite. *Multivariable Feedback Control*. John Wiley & Sons, West Sussex, England, 2^{nd} edition, 2005.

[48] R. E. Smith, M. I. G. Bloor, M. J. Wilson, and A. M. Thomas. Rapid airplane parametric input design (RAPID). In 12^{th} *AIAA Computational Fluid Dynamics Conference*, San Diego, CA, June 19-22, 1995. AIAA-95-1687.

[49] H. P. Stahl, G. H. Rowell, G. Reese, and A. Byberg. Multivariable parametric cost model for ground-based telescopes. In *Proceedings of the SPIE, Volume 5497*, pages 173–180. SPIE, 2004.

[50] Timothy D. Tuttle. *Creating Time-Optimal Commands for Linear Systems*. PhD thesis, Massachusetts Institute of Technology, Cambridge, MA, May 1997.

[51] Robert K. Tyson. *Principles of Adaptive Optics*. Academic Press, Inc., San Diego, CA, 1991.

[52] S. A. Uebelhart, L. E. Cohan, and D. W. Miller. Design exploration for a modular optical space telescope architecture using parameterized integrated models. In 47^{th} *AIAA/ASME/ASCE/AHS/ASC Structures, Structural Dynamics & Materials Conference*, Newport, RI, May 1-4, 2006. AIAA 2006-2083.

[53] S. A. Uebelhart, D. Howell, and D. W. Miller. Evaluating alternative architectures for lightweight space telescopes using parameterized models. In *2006 IEEE Aerospace Conference*, Big Sky, Montana, March 4-11, 2006.

[54] Scott A. Uebelhart. Conditioning, reduction and disturbance analysis of large order integrated models for space telescope. Master's thesis, Massachusetts Institute of Technology, Cambridge, Massachusetts, February 2001.

[55] Scott A. Uebelhart. *Non-Deterministic Design and Analysis of Parameterized Optical Structures during Conceptual Design*. PhD thesis, Massachusetts Institute of Technology, June, 2006.

[56] K. Wilcox and J. Peraire. Balanced model reduction via the proper orthogonal decomposition. *AIAA Journal*, 40(11):2323–2330, 2002.

[57] J. C. Wyant. Zernike polynomials. Technical report. URL: <http://www.optics.arizona.edu/jcwyant/Zernikes/ZernikePolynomials.htm>.

[58] Kemin Zhou and John C. Doyle. *Essentials of Robust Control*. Prentice Hall, New Jersey, 1998.